NOVEL Ni/Ce-Al_2O_3 CATALYSTS FOR BIOMASS GASIFICATION: KINETICS AND THERMODYNAMICS STUDIES

BY

SAGIR ADAMU

A Dissertation Presented to the

DEANSHIP OF GRADUATE STUDIES

KING FAHD UNIVERSITY OF PETROLEUM & MINERALS

DHAHRAN, SAUDI ARABIA

In Partial Fulfillment of the
Requirements for the Degree of

DOCTOR OF PHILOSOPHY

In

CHEMICAL ENGINEERING

DECEMBER 2017

KING FAHD UNIVERSITY OF PETROLEUM & MINERALS

DHAHRAN- 31261, SAUDI ARABIA

DEANSHIP OF GRADUATE STUDIES

This thesis, written by **Sagir Adamu** under the direction his thesis advisor and approved by his thesis committee, has been presented and accepted by the Dean of Graduate Studies, in partial fulfillment of the requirements for the degree of **DOCTOR OF PHILOSOPHY IN CHEMICAL ENGINEERING**.

Mozahar Hossain

Dr. Mohammad Mozahar Hossain
(Advisor)

Dr. Mohammad Bashammakh
Department Chairman

Shaikh Abdur Razzak

Dr. Shaikh Abdurrazzak
(Co-Advisor)

Dr. Salam A. Zummo
Dean of Graduate Studies

Dr. Mohammad Bashammakh
(Member)

13/2/18

Date

Dr. Mamdouh Al-Harthi
(Member)

Oki Muraza

Dr. Oki Muraza
(Member)

This PhD Thesis is dedicated to my parents Adamu & Rabi'atu, and my wife Hafiza

ACKNOWLEDGMENTS

I thank King Fahd University of Petroleum and Minerals, Saudi Arabia for giving me the golden opportunity to pursue this terminal degree. I would like to express my sincere gratitude to my Ph.D. Thesis Advisor, Dr. Mohammad Mozahar Hossain for his guidance during this work. He instilled confidence in me and upgraded my level of passion and commitment to research. He was both an Advisor and an elder brother. Thank you very much, Sir.

I am grateful to each of my committee members, in the persons of, Dr. Shaikh Abdurrazzak, Dr. Mohammad Bashammakh, Dr. Mamdouh Al-Harthi and Dr. Oki Muraza for facilitating this work. I am very grateful to Dr. Housam Binous who got me started on the thermodynamic equilibrium studies. I am also thankful to the staff of Chemical Engineering Department for their technical support at one point or the other. I thank Ahmad Rasheedy and Yasir Khan for their help in learning the operation of autoclave engineers' batch reactor, and CREC Riser Simulator respectively. I appreciate the help of Mr. Idris Bakare on the use of XRD equipment and his help in conducting pyridine FTIR of some samples. I thank Mr. Amanullah for some experimental set-up and Mr. Elgazoly for SEM analyses. I am also grateful to Dr. Tawfik and Mr. Zaki of Chemistry Department for their help with BET and elemental analyses respectively.

TABLE OF CONTENTS

LIST OF TABLES

LIST OF FIGURES

LIST OF SCHEMES

LIST OF ABBREVIATIONS

Variables

T	Temperature (Kelvin)
T_0	Reference temperature (K), equal to 298.15 K
P	Pressure (MPa)
P_1	Reference pressure (MPa)
P_i	Partial pressure of the i^{th} component (bar)
t	Time (s)
k_j^0	Pre-exponential factor for the j^{th} reaction
E_{WGS}	Activation energy for water gas shift reaction
E_{SRM}	Activation energy for steam reforming of methane
E_{RDRM}	Activation energy for reverse dry reforming of methane
K_i^{ads}	Pre-exponential factor for i^{th} species on the catalyst surface
ΔH_j^{ads}	Heat of adsorption for j^{th} species on the catalyst surface
R	Ideal gas constant (kJ/mol)
G	Gibbs' free energy (kJ/mol)
n_i	Number of moles of the i^{th} component
N	Number of gaseous species
S_i	Entropy of component i
y_i	Mole fraction of i^{th} component in gas phase
H_2	Hydrogen
H_2O	Water
CH_4	Methane
CO	Carbon monoxide
CO	Carbon dioxide

C	Carbon
C_{P_i}	Specific heat capacity
A_H	Total amount of hydrogen in the feed
A_C	Total amount of carbon in the feed
A_O	Total amount of oxygen in the feed
$a_1 \dots a_{10}$	Parameters for Duan equation
σ_m, ε_m	Lennard−Jones mixing parameters
a, b	Parameters for the Peng-Robinson equation of state

Superscripts

tot	Total
Res	Residual
$ideal$	Ideal gas

Subscripts

r	Reduced
c	Critical
mix	Mixture
m	Methane
ω	Acentric factor

Abbreviations

SCW	Supercritical water
SCWG	Supercritical water gasification
GEM	Gibbs' energy minimization
WGS	Water gas shift reaction
$RDRM$	Reverse dry reforming of methane
SRM	steam reforming of methane

ABSTRACT

Full Name : Sagir Adamu

Thesis Title : Novel Ni/Ce-Al_2O_3 Catalysts for Biomass Gasification: Kinetics and Thermodynamics Studies

Major Field : Chemical Engineering

Date of Degree : December, 2017

A new template-free technique was applied to synthesize a highly stable mesoporous Ce-doped-mesoporous-Al_2O_3 support. The newly prepared Ce(x)/Al_2O_3 were investigated for potential applications in a thermochemical process using appropriate characterization methods (such as TGA, SEM, TPD, TPR) and numerical analysis in the form of kinetic studies of NH_3 desorption from the surface of the support. The most promising support (i.e. 1.0 wt% Ce/Al_2O_3) was impregnated with varying amounts of nickel (5 to 20 wt%) and evaluated in a CREC riser simulator using glucose, toluene or mixed glucose/toluene as biomass surrogate species. XRD patterns showed that nickel is well dispersed on the alumina surface. Presence of ceria plus our successive nickel impregnation helped in conserving the catalysts high surface area (i.e. 102 m^2/g at 20 wt% nickel loading). Ceria dopant also suppressed coke formation during steam gasification of 15 wt% glucose in the fluidized bed reactor at 650 °C and 1 atm. Ni(20)/Ce-Al_2O_3 exhibited lowest extent of coking and produced highest amount syngas with H_2/CO ≈ 1.75:1. The acidity of the catalysts as determined via NH_3 TPD range from 0.317 to 0.202 mmol NH_3/g-sample as the nickel loading was increased from 5 to 20 wt%. The relative decrease in acidity is ascribed to coordination of Ni species with electron deficient Lewis acidic centers of the Ce-Al_2O_3. TPR profiles indicate that the catalysts are sufficiently reducible below 500 °C. Results of catalyst evaluation in CREC riser simulator show that the reduced form of the catalyst favors hydrogen production from glucose as compared to the oxidized form. Therefore, a possible mechanism is considered to describe glucose conversion to permanent gases (H_2, CO, CO_2, and CH_4) via intermediate products, using a reduced nickel catalyst. It is shown that the reduced catalysts favor bond cleavage, promotes water gas shift and steam reforming reactions to give hydrogen/syngas as more selective products. Raman spectral analysis of the regenerated catalyst showed no remnant coke after catalyst regeneration by oxidation/reduction protocol. Ni(20)/Ce-doped-Al_2O_3 with the best performance in terms of syngas production, and least tendency for coking was used for the kinetic studies (for T = 550 – 700 °C, and t = 5 – 25 sec) in the riser simulator. The detailed kinetic model comprises of reactant adsorption, surface reaction, and product desorption steps, involving water gas shift reaction (WGS), steam reforming of methane (SRM) and reverse dry reforming of methane (RDRM). The results of the model simulation show an excellent fitting in Mathematica, with a high coefficient of determination (R^2 = 0.999). The rate of water gas shift was the highest (i.e. $7.76x10^{-2}$ mmol/gcat.s.bar^2) followed by steam reforming of methane ($4.13x10^{-2}$

mmol/gcat.s.bar^2) and then reverse dry reforming of methane ($3.57x10^{-2}$ mmol/gcat.s.bar^2). The high reaction rates signify the suitability of the new Ni(x)/Ce-meso-Al_2O_3 catalytic system developed in this work, and applied for steam gasification of biomass. The modeling procedure could be applied conveniently to a different catalytic system in a similar reactor to obtain the necessary kinetic parameters.

A non-stoichiometric thermodynamic model was developed and applied to predict the equilibrium product composition of the gasification of any real biomass. The model is based on Gibbs' free energy minimization in which Peng–Robinson and Duan's equations of state (EoS) were used separately to derive the residual Gibbs free energy function. Glucose was used as a biomass surrogate to run the model, and the results were compared with experimental data. The accuracy of our calculation was verified by comparing the model's compressibility factor, Z for the gaseous mixture (i.e. CO_2, H_2O, H_2, CO and CH_4), with those obtained from Aspen-HYSYS at selected operating conditions. Temperature and water to glucose (W/G) ratio affect the syngas composition significantly.

Keywords:

Ce-doped-mesoporous Al_2O_3; Ni(x)/Ce-doped-Al_2O_3; biomass gasification; Coke resistance; thermodynamic modeling; kinetic modeling; CREC riser simulator; autoclave batch engineers' reactor.

ملخص الرسالة

الاسم الكامل: صغيرادامو

عنوان الرسالة: حفاز الالومينا (Al_2O_3) المبتكر والمطعم بمادة السيريوم والنيكل لتطبيق تغويز الكتلة الحيوية: دراسات حركية و حرارية

التخصص: هندسة كيميائية

تاريخ الدرجة العلمية: : ربيع الاول ١٤٣٩ هـ الموافق / ديسمبر ٢٠١٧ م

تم تطبيق تقنية جديدة لتحضير داعم الومينا(Al_2O_3) ذو مسامية و استقرار عالية مطعم بمادة السيريوم .تم دراسة قابلية استخدام هذه المادة المحضرة في عمليات الكيمياء الحرارية وذلك من خلال استخدام طرق التوصيف المناسبة (مثل TGA, SEM, TPD, TPR) والتحليل العددي في شكل دراسات حركية لامتصاص غاز النشادر (NH_3) على سطح الداعم.تم اختيار اكثر الدواعم الواعدة (1.0 wt% Ce/Al_2O_3) بتطعيمه بكميات متفاوتة من النيكل (5 إلى 20٪ بالوزن) ومن ثم اختبار ادائه في محاكي التفاعل (CREC riser simulator) باستخدام الجلوكوز والتولوين أو الجلوكوز المختلط / التولوين كأنواع بديلة للكتلة الحيوية. أظهرت تقنية (XRD) أن النيكل مشتت بشكل جيد على سطح الألومينا. ساعد وجود السيريا بالإضافة إلى التشريب المتعاقب للنيكل في الحفاظ على مساحة السطح العالية للحفاز (أي 102 متر مربع / جرام عند تحميل النيكل بنسبة 20٪ بالوزن) .كما قمع وجود السيريا تشكيل فحم الكوك خلال تفاعل التغويز ل15٪ بالوزن من الجلوكوز في المفاعل السرير المميع (the fluidized bed reactor) عند 650 درجة مئوية والضغط الوجوي. العينة (Ni(20)/Ce-Al_2O_3 اظهرت أدنى حد من فحم الكوك وكذلك أنتجت أعلى كمية من الغاز الصناعي (.$H_2/CO \approx 1.75:1$).

عند زيادة تحميل النيكل من 5 إلى 20٪ بالوزن, فأن الحموضة في المحفزات تتراوح من 0.317 إلى 0.202 ملي مول نشادر لكل جرام من العينة باستخدام غاز النشادر(NH_3). يعزى الانخفاض النسبي في الحموضة إلى ترابط جزيئات النيكل مع المراكز الحمضية (Lewis acidic centers). تحليل (TPR) اظهر أن المحفزات قابلة للتخفيض بطريقة فعالة عند درجة حرارة أقل من 500 درجة مئوية. أظهرت نتائج تقييم المحفز في جهازالمحاكاة (CREC riser simulator) أن الشكل المخفض (reduced) للمحفز يفضل إنتاج الهيدروجين من الجلوكوز مقارنة بالشكل المؤكسد (oxidized). وبناء على تلك النتائج السابقة, تم دراسة الاليات المحتملة لوصف تحويل الجلوكوز إلى غازات دائمة (H2) ، ثاني أكسيد الكربون، (CO_2) والميثان(CH4) عن طريق المنتجات الوسيطة وذلك باستخدام محفز النيكل المخفض. ويظهر من النتائج أن تفاعلات التحويل الغازي للماء (water gas shift) و الاصلاح البخاري(steam reforming) على المحفزات المخفضة تنتج الهيدروجين / الغاز الصناعي كمنتجات أكثر انتقائية .أظهر التحليل رامان الطيفي للحفاز المجدد عدم وجود بقايا فحم الكوك بعد تجديد حافزا بواسطة بروتوكول الأكسدة / التخفيض.تم عمل الدراسات الحركية باستخدام العينة (Ni(20)/Ce-doped-Al2O3) (عند دراجات حرارة 500-700 درجة مئوية، و از(مان 5-25 ثانية .يتكون النموذج الحركي التفصيلي من امتزاز متفاعل، تفاعل سطح، وخطوات امتصاص المنتج، والتي تنطوي على تفاعل تغيير غاز الماء (WGS)، وإصلاح البخار من الميثان (SRM) وإلاصلاح الجاف العكس للميثان (RDRM). نتائج محاكاة النموذج في ماثماتيكا تظهر

تتطابق ممتاز مع معامل فعالية عالية(R2 = 0.999). كان معدل تحول غاز الماء الاعلى ($7.76x10^{-2}$ mmol/gcat.s.bar^2) يليه إصلاح البخار للميثان ($4.13x10^{-2}$ mmol/gcat.s.bar^2) ثم الإصلاح العكسي الجاف للميثان ($3.57x10^{-2}$ mmol/gcat.s.bar^2). تدل معدلات التفاعل المرتفعة على مدى كفائة النظام الحفاز الجديد (Ni(x)/Ce-meso-Al_2O_3) الذي تم تطويره في هذا العمل وتطبيقه على تغويز البخار للكتلة الحيوية (steam gasification of biomass) .يمكن تطبيق إجراء النمذجة بصورة مماثلة على اي نظام تحفيزي مختلف في مفاعل مماثل للحصول على قيم المتغيرات الحركية اللازمة للدراسة. تم انشاء وتطبيق نموذج حراري غير متكافئ (non-stoichiometric thermodynamic) للتنبؤ بالمكونات الناتجة من تغويز أي كتلة حيوية حقيقية . يستند هذا النموذج على مبدأ جيبس الحد من الطاقة الحرة والتي تم فيها استخدام معادلة بينغ- روبنسون و معادلة دوان (EoS) بشكل منفصل. تم استخدام الجلوكوز كبديل للكتلة الحيوية لتشغيل النموذج، وتمت مقارنة النتائج المحصلة مع البيانات التجريبية. تم التحقق من دقة حسابنا بمقارنة عامل انضغاط النموذج (Z) للمزيج الغازي(CO_2, H_2O, H_2, CO and CH_4) ، مع تلك التي تم الحصول عليها من أسبن-هيسيس (Aspen-Hysys) في ظروف التشغيل المحددة . اثرت درجة الحرارة و نسبة المياه إلى الجلوكوز (W / G) على تكوين الغاز الصناعي بشكل كبير.

الكلمات الدالة

داعم الالومينا (Al_2O_3) ذو المسامية و الاستقرار عالية مطعم بمادة السيريوم, تغويز الكتلة الحيوية, مقاومة فحم الكوك, النمذجة الحرارية, النمذجة الحركية, محاكي التفاعل, مفاعل دفعة.

CHAPTER 1

INTRODUCTION

1.1 Background

Biomass is the fourth largest world's energy resource [1]. The total biomass production was estimated at 146 billion metric tons per year worldwide [2]. In Saudi Arabia alone, the municipal solid waste is about fifteen (15) million tons, 40-51% of which is constituted by food garbage [3]. Wastes from sewage plants, dairy, and date-palms factories also contribute a significant proportion of waste-biomass resources which could be harnessed for renewable chemical syntheses. Biomass conversion to gaseous or liquid fuels improves its energy density. This is achieved in different gasifier types, such as the fixed bed (e.g. updraft, downdraft, co-current, counter-current etc.), and a fluidized bed (e.g. fast fluidized and circulating fluidized bed). The common gasifying agents are air, steam, and oxygen. The use of steam in a fluidized bed reactor is a promising approach for biomass conversion to syngas. Its inherent advantages include rapid heating and fluidization of biomass/catalyst mixture, effective heat transfer between reacting species with negligible hotspots, and uniform gasifier temperature, tolerance for a wide range of particle size distributions of biomass having varying fuel quality [4,5]. Figure 1.1 depicts general gasification process, involving different reaction network.

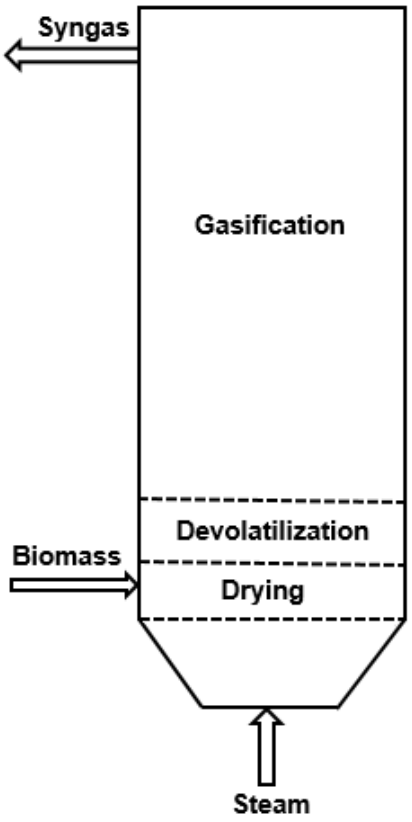

$$Tar + H_2O \rightarrow H_2 + CO$$

$$CH_4 + H_2O \rightarrow CO + 3H_2 \qquad \Delta H^0 = 205.81\ kJ/mol$$

$$CH_4 + CO_2 \rightarrow 2CO + 2H_2 \qquad \Delta H^0 = 246.98\ kJ/mol$$

$$CO + H_2O \rightarrow H_2 + CO_2 \qquad \Delta H^0 = -41.16\ kJ/mol$$

$$C + H_2O \rightarrow H_2 + CO \qquad \Delta H^0 = 131.29\ kJ/mol$$

$$C + CO_2 \rightarrow 2CO \qquad \Delta H^0 = 172.46\ kJ/mol$$

$$C + 2H_2 \rightarrow CH_4 \qquad \Delta H^0 = 131.29\ kJ/mol$$

$$C_xH_yO_z + H_2O \rightarrow H_2 + CO + CO_2 + tars$$

Figure 1.1: Schematic diagram for steam gasification of biomass.

The overall process comprises of three main steps: biomass drying, devolatilization, and gasification. Devolatilization breaks the biomass into permanent gases, tars, and carbon. The main gasification then proceeds to reform the biomass tar into syngas, and gasify coke to syngas, and the permanent gases react with one another to redistribute the product composition towards thermodynamic equilibrium.

However, each of the gasifiers listed above requires that the waste biomass feed is pretreated and dried to get rid of a large amount of its water content (up to 70%) [6]. Thus, there is the need for developing alternative conversion processes, which will skip

the economically unfavorable drying step. Supercritical water gasification (SCWG) is one of the most promising techniques for the conversion wet or moist biomass into a hydrogen- or methane-rich gas, which can be used for a wide number of applications. Supercritical water refers to the state of water beyond its critical conditions of 374 °C and 22.1 MPa. Supercritical water exhibits different physical properties than those of subcritical water or even steam. These include low dielectric constant, viscosity, thermal conductivity, a high peak in the specific heat capacity around the critical point [7,8]. The potential areas of applications of waste biomass gasification include heat and electricity generation, on-site generation of fuel within industries, buildings or vehicles. Despite its promising potential, SCWG has the following inherent limitations: (1) Formation of significant amounts of tars and chars which can cause fouling and hamper continuous operations. (2) SCWG is an energy-intensive operation. Therefore, a catalyst is required, which should reform these tars to syngas, and provide appreciably high yield at moderate temperature. Part of this work entails theoretical studies of waste carbonaceous materials (WCM) gasification, in the form of Thermodynamics Analysis. This shall guide our experimental work which will involve the design, synthesis, and characterization of a cheap, stable and high biomass conversion heterogeneous catalysts in the form of $M_1/M_2{-}Al_2O_3$ and we will conclude with kinetics studies. The synthesis and characterization of the above catalysts and the subsequent application to producing syngas, a fuel and a precursor to methanol among many other chemicals make the niche for anticipated interesting contributions by the proposed study to the literature.

The thermodynamics study shall cover mainly, the application of Gibbs free energy minimization techniques to predict the product composition of biomass gasification of

different feeds. Also, two different equations of state shall be used to predict the *Activation Energy Residual function* for different water/carbon ratio, which will be incorporated into the Gibbs' free energy minimization model and for different waste biomass species. As regards the catalysis, the major contribution will originate from the unpublished combination of proposed Metal/Support—Catalyst synthesis.

1.2 Scope of this work

This work focuses on the synthesis of ceria-doped-alumina for application in nickel-catalyzed biomass gasification. Target reaction conditions are up to 700 °C in a CREC fluidized bed reactor at atmospheric pressure; or up to 500 °C, 250 bar in an autoclave engineers' batch reactor. The study is also targeted at mitigating catalyst coking, enhancing catalyst thermal stability and fluidizability for optimal output in biomass gasification operation under turbulent fluidized bed conditions or well-mixed batch reactor conditions.

Biomass surrogates are utilized to represent the real biomass. Glucose is used as a surrogate for the cellulosic content of biomass, while toluene is used to represent the intermediate tar content of a real biomass gasification. This facilitates successful simulation of the real gasification process. Furthermore, some real biomass materials such as banana peels, apple pomace rice husk, and millet husk were obtained, characterized, and pyrolyzed to have an idea of the maximum amount of syngas and ash content that could be obtained from the gasification of such real feeds. Traces of nitrogen, sulfur, and other impurities in the biomass were neglected and are therefore outside the scope of the present work.

A highly stable ceria doped gamma alumina is developed in this work. CeO_2 is selected as a dopant to improve the thermal stability without impairing the overall catalytic performance of the final Ni/Ce-doped-Al_2O_3 catalysts. A successive incipient wetness method was used to achieve the impregnation of nickel up to 20 wt%. The mode of catalyst regeneration during repeated gasification cycles are systematically studied. Properties of the fresh and spent catalyst are obtained by appropriate characterization methods as enumerated in Chapter 4.

The motivation for this work stems from the following:

- The need for alternative renewable energy sources.
- The abundance of waste carbonaceous biomass such as municipal wastes, wastes from dairy and date palm factories of Saudi Arabia, and the need for beneficial solid waste management.
- Availability of transition metals catalysts at affordable prices.
- The need for understanding biomass gasification reaction kinetics.

The methodologies that are used to achieve the above objectives are reported in the section entitled "research methodology". The references cited in this work are listed appropriately in the bibliography.

1.3 Thesis structure

This thesis is organized as follows:

- Chapter 2 reviews biomass gasification catalysts, and state of the art in biomass gasification and the current challenges.

- Chapter 3 summarizes the objectives of the present studies.
- Chapter 4 describes the methodology of the present studies. It contains the detailed description of synthesis characterization and the relevant analyses.
- Chapter 5 details the catalyst development, results of catalysts characterization, coke studies, and desorption kinetics studies
- Chapter 6 covers the detailed thermodynamic modeling and give the results in comparison to some experimental data
- Chapter 7 illustrates the development of a detailed kinetic model and the procedure for parameter estimation
- Chapter 8 provides concluding remarks and recommendation for future studies.

CHAPTER 2

LITERATURE REVIEW

In this Chapter, we provide an overview of the milestone attained so far in the catalytic waste biomass gasification. The Chapter also reviews the literature in thermodynamics and kinetic analyses of gasification of some model biomass compounds.

2.1 Biomass gasification: thermodynamics, catalysts, and kinetics

Thermochemical transformation of waste biomass to syngas has been applied to maximize the energy potential of waste biomass materials, and at the same time serving as a way of solid waste management. This process has zero net CO_2 emission, as the CO_2 involved during gasification is recycled back to plants for photosynthesis [See Figure 1.2]. The thermochemical techniques could be the conventional air, steam or the recent supercritical water gasification (SCWG). However, SCWG proved to be much more efficient than the others, because it produces less tar and chars and most importantly could handle wet biomass directly without the expensive drying step [9,10], requiring about 2.4 MJ/kg-H_2O at atmospheric conditions. The steam reforming of biomass as an alternative route for hydrogen production was proposed since 1974 by Antal and coworkers [11]. However, it was revealed shortly that this process generates various gaseous products including tar and coke with a low hydrogen yield [12]. This finding discouraged further research into the subject. Later on, different researchers around the world recommenced the study of biomass gasification again, but now using supercritical

water (SCW) [11,13–15]. Recent investigations into this subject include the work of Letellier et al. (2008), who conducted numerical investigations of gasification of wet biomass in supercritical water. They built a thermodynamic model which accounts for the solid, liquid and gas phases involved, as well as the energy requirements in the course of SCWG. The components considered included H_2, CH_4, H_2O, CO, CO_2, NH_3, H_2S, CH_3CHO, CH_3COOH, C_6H_5OH, Char and minerals [16]. Similarly, Begum developed a model for fluidized bed gasification of waste biomass, which predicts the pressure, temperature, steam-fuel ratio and air-fuel ratio, for a pilot scale SCWG plant [17]. Earlier, some investigators in China conducted similar thermodynamics studies and reported the favorable conditions for hydrogen yield at temperatures beyond 650 K, pressure range of 20-35 MPa; and feed concentration of 0.1-1.0M [12]. They showed further that high oxygen (greater than stoichiometric quantities) decreased methane and hydrogen yield. However, increasing pressure and temperature improves hydrogen purity but decrease its recovery ratio [18]. Kaushal built 1-D model for bubbling fluidized bed gasifier containing two-phases (bubble and emulsion) and two-compartments (dense lower compartment zone and upper freeboard) considering the overall reaction kinetics, mass and energy balances, tar generation and cracking, biomass feed type and fluidizing agents such as oxygen, air, steam or their suitable combinations [19]. Xue and Fox also used computational fluid dynamics to study the physical and chemical processes during a fluidized-bed gasification of polydispersed biomass particles, considering the interaction between the particles with the reactive gas [20]. However, they did not validate their results against experimental data. Yakaboylu and coworkers proposed a kinetic model involving 74 reactions steps in the supercritical region and 55 others, in the subcritical

region with validity in the range of temperatures around 650 °C and pressure in the range of 25−30 MPa [21]. They implemented the scheme in Aspen Plus software with different real feeds. Apart from their narrow range of operation, they did not carry out statistical analysis to optimize their operating parameters. It should be noted that none of the previous works compared the compressibility factor predicted by their model to that of a real mixture with the same composition. The study proposed herein will involve thermodynamic model formulation and its validity will be addressed by considering this important parameter of the gaseous mixture.

In terms of experimental studies, biomass gasification with or without catalysts has been the subject of many studies. The catalysts in use currently are largely based on nickel/Al_2O_3, dolomite, and olivine [5]. The advantages of nickel-based catalysts have been listed to include its high efficiency in converting waste carbonaceous materials into hydrogen, due to efficient cleavage of C−C bond; economically viable than noble metals, and the synergistic metal/support effect especially when impregnated on metal oxide supports such as Al_2O_3 [22–24]. Similarly, the metal oxide supports such as Al_2O_3 (having a high thermal stability, high adsorption capacity and excellent mechanical strength) could be tuned to provide a high specific surface area for an excellent dispersion of nickel species thereby inhibiting sintering and crystal growth [25]. Adhikari et al. found that the best set of parameters for generating hydrogen from steam reforming of glycerin at atmospheric pressure are temperatures beyond 900 ^{O}C and water/Carbon ratio of 9.1. They found that at these conditions, methane formation is minimized while coke deposition is thermodynamically inhibited [6]. Lu et al. (2010) developed Ni/γ-Al_2O_3 and Ni/CeO_2-γ-Al_2O_3 catalysts by impregnating the appropriate precursors on a commercial

γ-Al2O3. They applied these catalysts to investigate gasification wet biomass gasification in SCW. They found that carbon deposition and coking results in catalysts deactivation, but that Ceria played some role in inhibiting the deactivation [18]. Zhang et al. (2011) evaluated 17 different catalysts based on four different transition metals: Ni, Ru, Co and Cu on different supports (Zirconia, gamma alumina and activated carbon). They showed that at 600 C, 20 wt. % Ni loaded on Al_2O_3 gave hydrogen yield of 38.4 mol. per kg of glucose, which is 20 folds higher than that obtained in the run without any catalyst. On the other hand, copper and cobalt catalysts showed much less activity for SCWG of glucose [26]. Manzour (2012) screened different Ni-based catalysts to ascertain their performance on H_2 production during supercritical water gasification of glucose. Their best results were for α-Al_2O_3, CNTs and MgO supports [27]. Lu et al. (2012) conducted statistical studies to optimize the process parameters for hydrogen production from wet biomass (corn cob), and found the significant effect of the parameters on hydrogen yield was in the order: temperature (range: 823 – 923 K) > pressure (range: 22.5–27.5 MPa) > feed concentration (2–4.0 wt. %) > residence time (20–40 sec) [9]. Nanda et al. (2015) investigated the effects of four (4) parameters (temperature: 550−700 °C; catalyst concentration: 0.2−0.8 wt. %; feed concentration: 4−10 wt. % and residence time (30−75 s) during SCWG of lactose as a model compound for dairy waste in a tubular reactor [28]. They observed that at a pressure of 25 MPa, the optimum operating parameters for highest hydrogen yield, CGE and gaseous products, were at temperature of 700 °C, feed concentration of 4 wt. % and a residence time of 60 s. Moreover, addition of 0.8 wt. % Na_2CO_3 gave a better yield of hydrogen (22.4 mol/mol lactose) compared with the blank run (16 mol/mol lactose). However, a recent

study on the energetics of SCWG by Yakaboylu, on different conceptual designs of SCWG plants shows that the thermal efficiency of the process is better when the reactor is operated at a lower temperature and with high feed concentration [29]. Wu et al. (2011) loaded Ni on MCM-41 support and obtained a good dispersion of NiO particles while maintaining a high surface area, and high pore volume [30]. The yield of hydrogen increased with the amount of Ni loading (i.e. from 5 to 40 wt.% Ni/MCM-41), and a maximum of 4 % coke was produced. The low degree of coking was attributed to the use of a two-stage reaction, which has the advantage of good temperature control for each of the two process stages as well as excellent contact between formed tar and catalysts [23,30–32]. Mazumder (2014) synthesized fluidizable Ni-La_2O_3/Al_2O_3 catalysts for application in a CREC fluidized bed reactor for steam gasification of biomass [7]. The presence of La_2O_3 not only improved Ni-support interaction but also improved fluidizability of the catalysts. However, he neither apply an experimental design to optimize the process parameters nor did he try other promoters to compare and confirm the role La_2O_3 as concluded in his investigations. Some researchers have demonstrated some pilot scale experiments in an effort to commercialize the SCWG. Karlsruhe Institute of Technology (KIT) claimed to have built the first continuous operating plant worldwide named Verena Pilot Plant for biomass gasification in supercritical water. It works up to a pressure of 35 MPa and temperature of 700°C. Boukis in 2007 attempted to improve the process performance of this pilot plant by dividing the heat exchanger into two parts on the feed side to improve its overall efficiency (See Figure 2.1:) [33]. Thus the biomass was heated to subcritical temperatures and then mixed with water at supercritical state in the reactor space. Second, they devised a solid removal method to

get rid of the solids (mainly salts) from the reactor bottom where they settle due to the flow direction and gravity. Boukis and co-workers were able to operate the plant for 10hrs, generating 77% H2 at 20 MPa after integrating CO2 removal system.

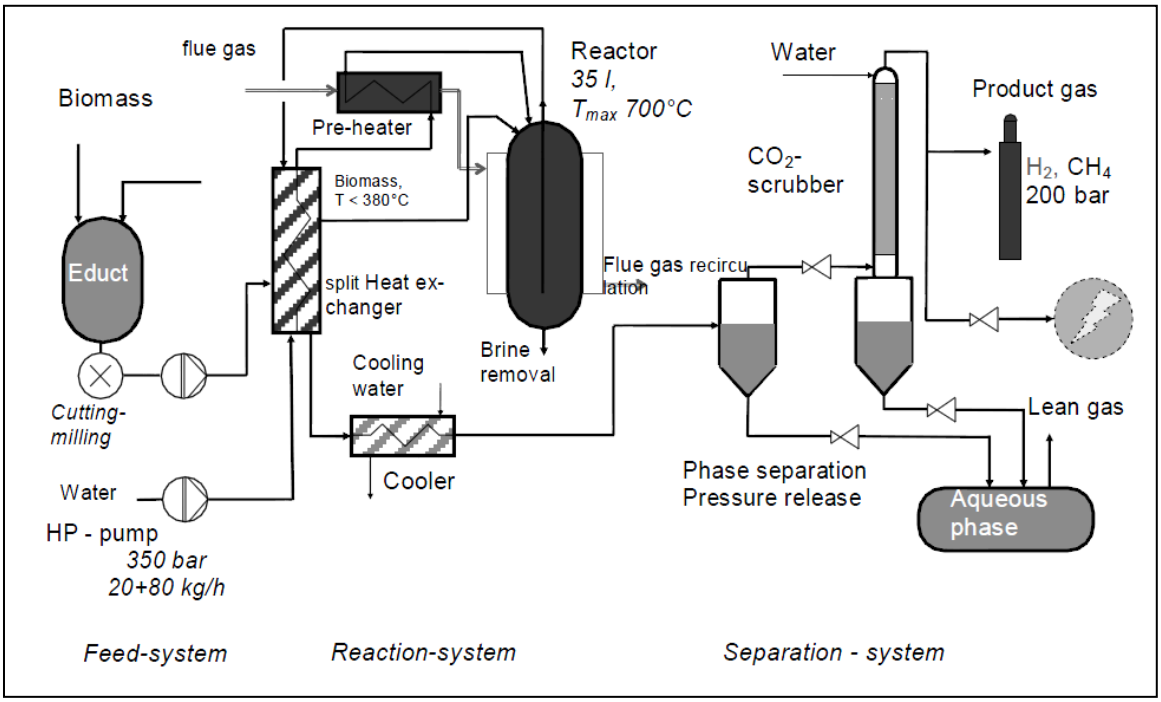

Figure 2.1: Process Flow Diagram of Verena Pilot Plant reported in ref. [33].

Therefore we conclude this part as follows. There is a lot of work to be done to bring the biomass waste to syngas process into a commercially viable technique. Key areas should be the catalyst design and synthesis to reduce the high cost associated with the high-temperature uncatalyzed processes. The reaction kinetics and chemistry will help in the predictability and scale-up of the overall process. Thermodynamics analysis will set the extremum obtainable with the "ideal catalysts".

2.2 The use of model compounds as biomass surrogate

Plant biomass comprises mainly of cellulose, lignin, and hemicellulose. Scheme 2.1: shows a pictorial representation of biomass showing its various components [34].

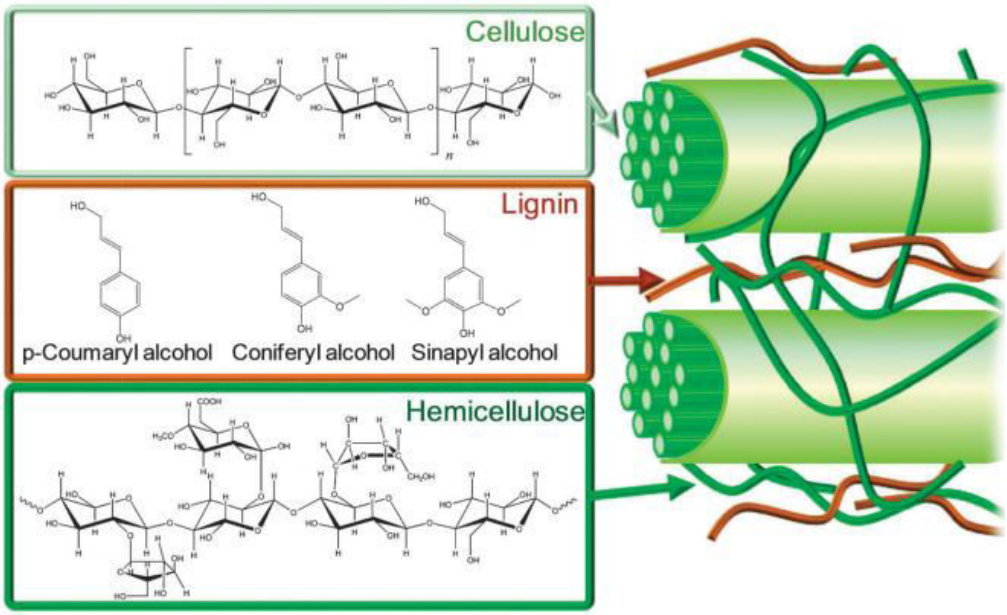

Scheme 2.1: Schematic diagram for lignocellulosic biomass [34].

Because of the complex nature of a real biomass feedstock, it is a great deal of challenge to understand the chemistry of their gasification reaction pathways. Therefore, experiments are usually performed using model biomass feeds to enable the understanding of a real biomass reaction subjected to the same operating conditions [21]. These are generally represented by their monomers.

Table 2.1 shows some of the common feed types used as biomass model compounds, with the motivation for their usage in various studies.

Table 2.1: Some common feed types used as biomass model compounds.

Feed type (model biomass)	Motivation for feed usage	Author
Glycerine	Abundance (from biodiesel production) and cheap	[6,35]
Phenol	Phenol is a model compound for the phenolic structures constituting the *lignin* content of biomass.	[36]
Glucose	Representative for *cellulose.*	[7,26,37–41]
2-methoxy-4-methylphenol.	Representative of *lignin* content/produced tars	[7]
Toluene	Model of stable aromatic compounds found in tar which is formed during high-temperature gasification.	[42,43]
Ethanol	Readily available fuel with ease manipulation and low toxicity (unlike CH_3OH) and is produced from several biomass sources	[44–46]

In order to understand the chemistry of biomass gasification reaction, the mechanism shown in Scheme 2.2 was reported by the authors [47], for gasification of glucose as a model compound for cellulosic biomass. Fructose, furfural, and 5-(hydroxymethyl)

furfural and TOC are the intermediates while char and gas (CH_4+ H_2 +CO +CO_2) are the final reaction products.

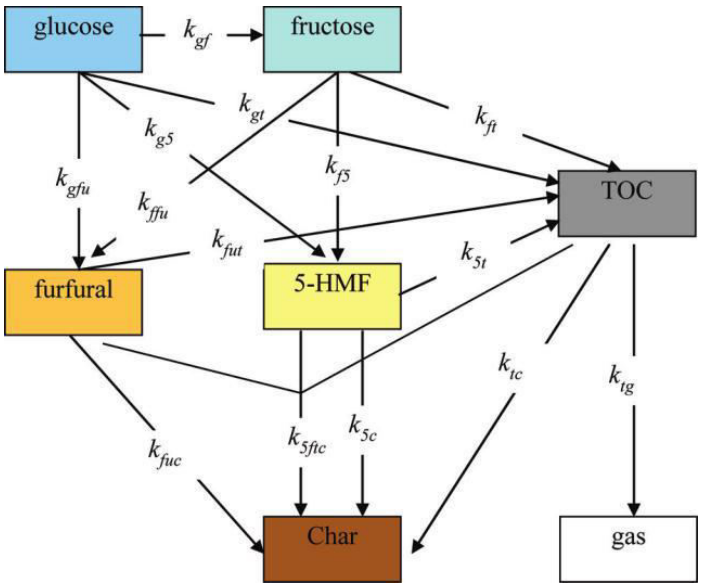

Scheme 2.2: Proposed reaction scheme for SCWG of glucose [48].

Godwin et al. [49], reported a scheme for the gasification of xylose, as a model compound for lignin (See Scheme 2.3). The scheme shows that xylose could be dehydrated directly into furfural and subsequently converted to permanent gases (CH_4+ H_2 +CO +CO_2). Other possible intermediates are glyceraldehyde, methyl formate, propanoic acid, maple lactone, acetic acid, ($C_5H_xO_y$) etc. These intermediate will interact in varying ways with some of the permanent gases, water and carbon to engage in steam reforming, dry reforming, Bourdourd, hydrogenating and methanation reactions to give the final product composition, depending on the catalyst activity and the reaction time.

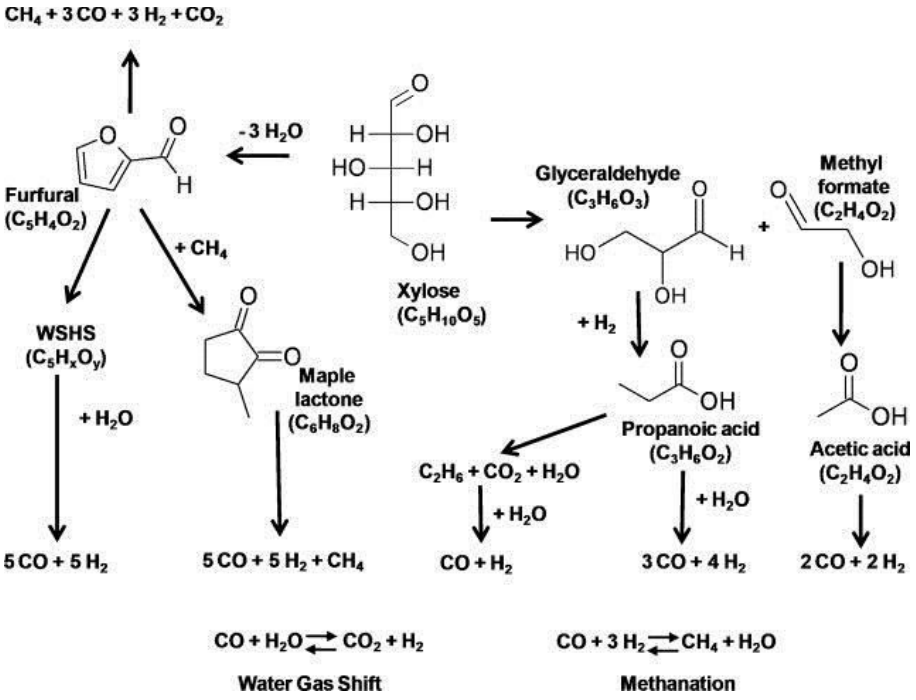

Scheme 2.3: Proposed reaction scheme for SCWG xylose between 450 and 650 °C.

It is seen that biomass comprises of 3 main components—cellulose, lignin, and hemicellulose. One of the cellulosic biomass surrogate compounds often selected for biomass gasification studies is glucose. The molecular formula of glucose is given in Scheme 2.4.

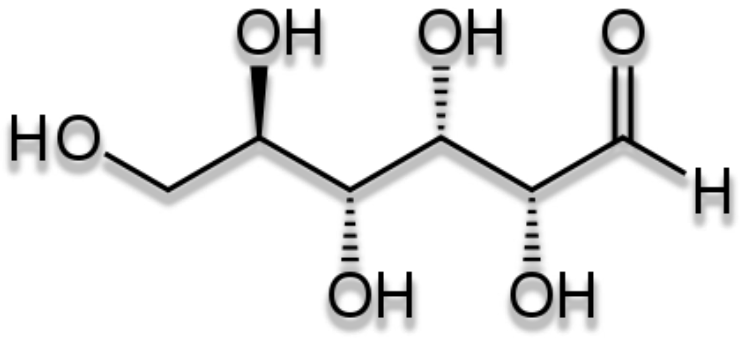

Scheme 2.4: Molecular structure of glucose.

It is hypothesized that the kinetics of glucose gasification will help in understanding the overall mechanism of catalytic biomass conversion [26,50,51]. The proponents of this hypothesis argue that, just like glucose, cellulosic biomass first undergo pyrolysis into permanent gases (CH_4, H_2, H_2O, CO, and CO_2), coke and tar [52], which would later recombine in the presence of a catalyst and redistributed according to the activity and selectivity of the catalyst applied. For example, the reaction network shown in Scheme 2.5 was suggested for gasification of cellulosic biomass, via glucose [53].

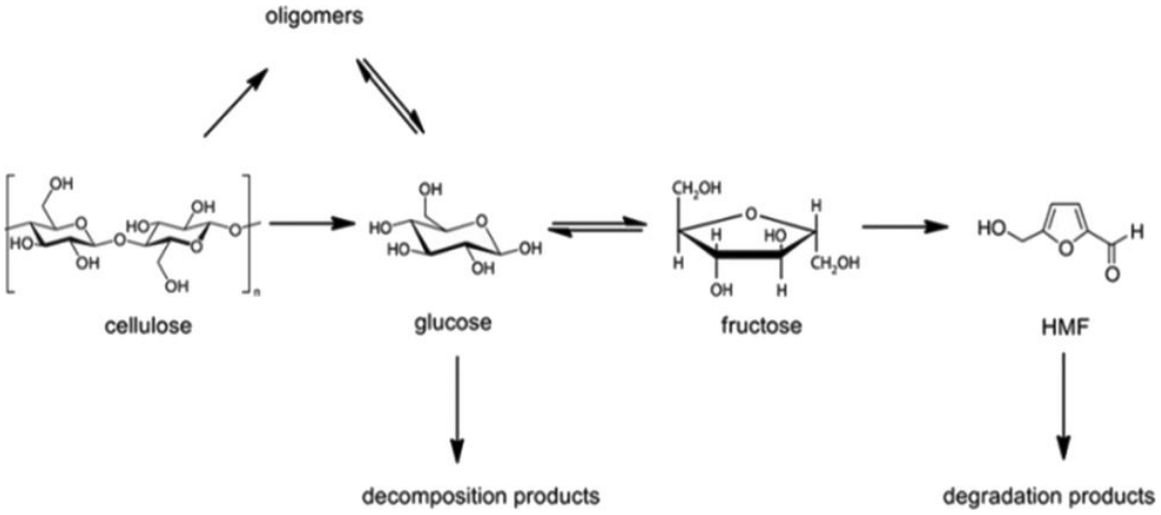

Scheme 2.5: Cellulose transformation to HMF via glucose and fructose [53].

In the above scheme, cellulose will get transformed directly to glucose or converted to some range of oligomers which will eventually form glucose. The glucose will either pyrolyze to decomposition products (CH4, H_2, H_2O, CO, and CO_2), coke and tar [52] or transform to fructose and to hydromethyl furan, and so on.

Wang et al. [54] proposed mechanism shown in Scheme 2.6 for cellulose hydrolysis to glucose and subsequent dehydration to HMF and then levulinic acid as shown below.

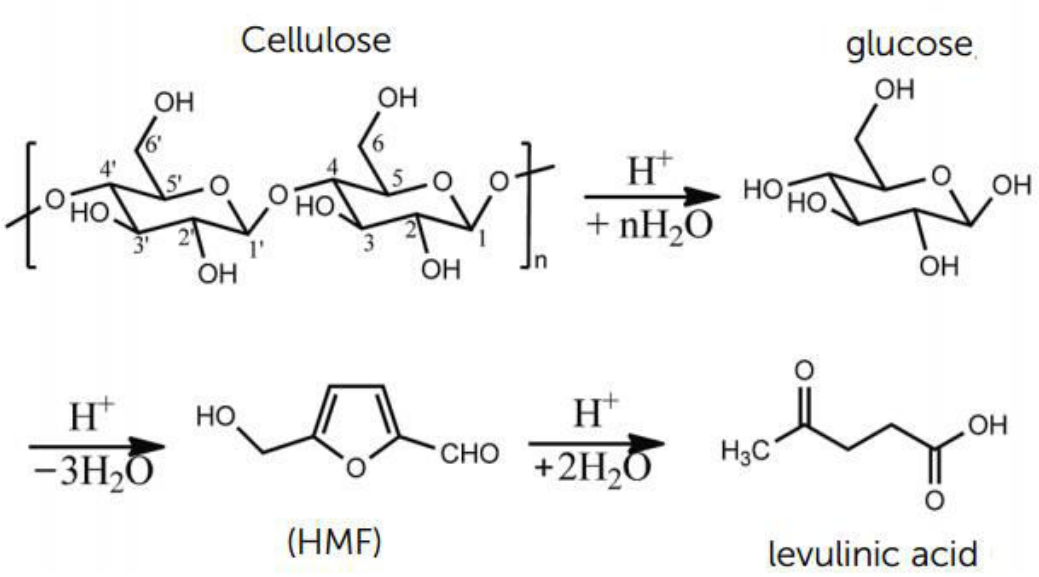

Scheme 2.6: Conversion of cellulose via glucose, HMF and levulinic acid

From the ongoing reaction schemes of cellulose conversion to other chemicals, it is justifiable to use glucose as a biomass surrogate to study the energetics, kinetics, and chemistry of biomass gasification. Since the activation energy of the gasification reactions is high, a high temperature is needed to achieve a reasonable conversion. Alternatively, an appropriate catalyst is utilized at moderate temperature. The next subsection provides an overview of the conventional catalysts used for biomass gasification.

2.3 Conventional catalysts used for biomass gasification

Catalysts are vital in energy-intensive processes such as gasification, in order to attain a high conversion at relatively lower temperatures (< 700 °C) [55]. Catalysts alter the gasification reactions pathways, thereby resulting in a significant decrease in tar and coke formation. Consequently, a catalyzed gasification would show significantly higher product yields and much better carbon gasification efficiency (CGE). Heterogeneous catalysts based on ruthenium, nickel and activated carbon have been widely applied in the

literature [7,8,55–58] for both real and model biomass gasification. This has enabled the possibility of obtaining CGE at low temperatures (e.g 400 °C) [47].

2.4 Current challenges in the application of nickel-based catalysts

These represent a major class of catalytic materials utilized in steam or supercritical water gasification of biomass. Chan and Tankasale summarized recent reports on nickel-based catalyst as applied to biomass gasification [59]. They identified coke as the key factor for catalysts deactivation. On the other hand, small crystallite size and a high degree of dispersion of nickel on the support, as well as the addition of a metal promoter could significantly improve the catalytic activity. The promoters such as La, Co, Pt, and Cu tend to enhance the reducibility of the nickel by moderating the metal support interaction and resisting coke formation [60–62]. Among the catalysts preparation techniques, the most commonly reported are incipient wetness technique, co-precipitation, and co-impregnation. Some authors applied precipitation & impregnation, co-precipitation and co-impregnation techniques to impregnate their active species on the support (e.g. refs. [62,63]). Efika et al. [64] adopted the incipient wetness technique impregnation to obtain a highly active Ni/dolomite catalysts. Chan et al. [59] showed that at 800 °C, Pt-Ni/dolomite and Fe-Ni/dolomite both prepared by precipitation & impregnation showed the highest gas yield of 79 and 78 % respectively. In terms of hydrogen chemisorption analysis of nickel-based catalysts, Srinakruang et al. [65] achieved a very small Ni/α-Al_2O_3 particle size of 7.9 nm. However, their Ni/Mg catalyst showed only 8% TPR reduction degree while other authors [64] were able to achieve up to 149 % on a 5% Ni on CeO_2–Al_2O_3. This hints to a significant role of ceria in

enhancing the catalyst reducibility and hence the availability of its active sites for the desired reaction.

CHAPTER 3

RESEARCH OBJECTIVES

The main objective of the present study is to develop fluidizable Ni/Ce-doped-Al_2O_3 catalysts for gasification of biomass surrogate in a fluidized bed reactor operating at atmospheric conditions.

The specific objectives of this work are:

1. Investigation of the promotional effects of Ce on Ni/Ce-Al_2O_3 catalysts:
    a. To synthesize new ceria stabilized mesoporous alumina support and evaluating its potential applications for hydrothermal operations via relevant characterization techniques and ammonia desorption kinetics from the newly prepared support.
    b. To impregnate differnet amounts of nickel catalyst on the newly prepared support via incipient wetness impregnation.
    c. To characterize the prepared catalyst using XRD, BET, SEM and TPR, TPD, FTIR and Raman Spectroscopy.
    d. To evaluate the performance of the prepared catalysts for biomass gasification in a CREC riser simulator.

e. To investigate the role of catalyst regeneration mode, namely, (i) calcination in the air only (to form NiO), or (ii) calcination in air plus reduction in a hydrogen atmosphere (to form $Ni^{(0)}$), on the recyclability of the spent catalyst.

f. To carry out an experimental design to ascertain the effect of mode of catalyst regeneration and on the catalyst recyclability, hydrogen selectivity and syngas composition in the riser simulator.

2. Development of phenomenological kinetic model for glucose gasification over Ni/Ce-Al2O3 catalyst:

    a. To develop plausible mechanism by which nickel/ceria-alumina catalysts convert glucose to gaseous products.

    b. To develop of a phenomenological kinetic model considering the transient product distributions as well as the amount of catalyst employed and the reactor volume.

3. Comparison between experimental and equilibrium product compositions:

    a. To develop and validate a thermodynamic model based on Gibbs' free energy, which will be minimized according to material balance constraints to give the equilibrium product distributions.

    b. To compare thermodynamic model predictions with experimental gasification results

CHAPTER 4

METHODOLOGY

4.1 Introduction

This Chapter covers the procedures and experimental methods involved in the synthesis of the new ceria-doped alumina and the Ni/Ce-Al_2O_3 catalysts, including the methods for their characterization and testing in the CREC riser simulator. Section 4.2 discusses the synthesis procedures for the new Ce-Al_2O_3 support and the Ni/Al_2O_3 catalysts. Section 4.3 reports the characterization techniques adopted to ascertain the physicochemical properties of the new ceria/alumina support as well as the Ni/Ce-Al_2O_3 catalysts. Section 4.4 gives a detailed explanation on the CREC fluidized bed reactor configuration with its accessories, and the experimental procedures adopted to ascertain the catalysts reactivity for steam gasification of model biomass compounds in the reactor.

4.2 Catalyst synthesis

4.2.1 Materials

The chemicals used are cerium nitrate hexahydrate ($Ce(NO_3)_3.6H_2O$), nickel nitrate hexahydrate ($Ni(NO_3)_2.6H_2O$), aluminum nitrate nonahydrate ($Al(NO_3)_3 \cdot 9H_2O$), ammonium carbonate and glucose. These were all purchased from Sigma–Aldrich.

4.2.2 Preparation of alumina supports

The required amounts of the aluminum nitrate nonahydrate and ceria nitrate hexahydrate were dissolved in a 100 mL of deionized water. This was succeeded by the

gradual addition of 0.1 molar solution of ammonium carbonate hydrolyzer using a burette at the rate of about 5 cm^3/min. While, adding the hydrolyzer, the reaction mixture was stirred vigorously with a magnetic stirrer, until a monolithic gel was formed. At this point, the stirring was stopped immediately, and the molar ratio of $(NH_4)_2CO_3$ to $Al(NO_3)_3.9H_2O$ was in the range 1.0-1.4, and gel pH between 5.0-5.5. The gel in the beaker was then aged at 60 ^OC for 48 h, and then the crude gel was centrifuged and emptied into a crucible and returned to the oven at 100 ^OC for another 24 h. Finally, the solid was thermally treated for 10 h each at 150 ^OC and 200 ^OC, in order to get rid of NH_4NO_3 and then calcined to 750 ^OC for another 10 h.

4.2.3 Ni/Ce-Al_2O_3 Catalyst preparation by incipient wetness impregnation

The already calcined support was characterized by BET to determine its pore volume and pore size distribution (see the section on catalyst characterizations). The required amount of the catalyst together with a magnetic stirrer were both placed inside a conical flask having a lateral opening and closed firmly with a rubber septum. The lateral opening is connected to a vacuum pump whose function is to remove any air/gases trapped within the pores of the support. 120% volume of deionized water was taken and used to dissolve an equivalent of 5 wt. % nickel nitrate hexahydrate ($Ni(NO_3)_2.6H_2O$). A syringe was used to perform the impregnation under vacuum and 500 rpm magnetic stirring. The paste obtained was dried overnight at laboratory conditions, subjected to calcination at 750 °C, and then reduced in a gaseous stream of 10% hydrogen in helium.

4.3 Catalyst characterizations

4.3.1 Nitrogen physisorption

The new alumina support surface area, pore size and pore size distribution were obtained from a Micromeritics ASAP 2020 instrument using nitrogen as probe molecule at 77 K. Prior to analysis, the sample was first degassed at 300 °C for 2.5 h. The adsorption and desorption isotherms were measured in the relative pressure range of 10^{-6} to 1.0. The multiple point BET was used to calculate the surface area, total pore volume and cumulative desorption surface areas were obtained using Barrett, Joyner and Halenda (BJH) method [66], while the pore size distribution was evaluated using Dollimore and Heal (D-H) method [67].

4.3.2 Thermal gravimetric analysis

The thermal behavior of the prepared mesoporous supports and spent catalysts were studied under air in an SDT Q600 analyzer. About 5.0 mg of the sample was used for the analysis. The temperature was first equilibrated at 25 °C and then ramped at 10 °C/min till 900 °C. The weight percent and the differential weight percent—temperature data were recorded and reported herein.

4.3.3 Ammonia temperature program desorption (TPD)

It is known that solid catalysts have a wide range of application in the conventional petrochemical industries as well as in the emerging biofuel industries. The proponents of green chemistry emphasize on the reduction of solid waste at their sources and elimination of toxic by-products, by applying the appropriate solid acidic catalysts. It is also known that the total and relative amounts of Lewis and Brønsted acid site types on

the solid catalyst surfaces are related to their catalytic activity [68,69]. Therefore, the turnover frequency of a particular reaction, which is defined as the amount of feed converted to the desired product by 1 mole of the active site per hour, could be correlated to the total acidity. Thus, it is necessary to quantify the total and relative acidity of the solid catalysts. The application of ammonia temperature programmed desorption (TPD) has a number of advantages: (1) NH_3 TPD protocol is simple and reproducible (2) Weak and strong acid site types could be easily distinguished (3) the total area under the concentration-time curve gives the total acidity or acid strength of the solid catalyst. On the other hand, it is not obvious how ammonia is adsorbed at a surface, and different kinds of adsorption sites (Lewis and Brønsted sites) can be hardly distinguished. On the other hand, pyridine FTIR provides a clearer picture of the different acid site types (i.e. Lewis or Brønsted). The two methods give virtually similar results, with slight variation from the fact that NH_3 molecule is smaller than pyridine and hence it can access more active sites in obscure locations inside the catalyst.

The ammonia TPD was performed in an Autochem II 2920 analyzer from Micromeritics. For a typical analysis, about 0.1 g of the catalyst was sandwiched between quartz wool, within a U-shaped quartz tube reactor, which is placed into the sample port. The sample is initially prepared by reducing it in a stream of 10% H_2 in helium at 500 °C followed by degassing at the same temperature for 2 h under Argon. Ammonia (5.52% NH_3 and 94.48% helium) was then flown for 1h at a rate of 50 ml/min to saturate the catalyst at 120 °C. The system is then ramped at a rate of 10 °C/min until 750 °C during which ammonia desorption was monitored by a sensitive thermal conductivity detector (TCD).

4.3.4 Temperature program reduction (TPR)

Micromeritics Autochem 2920 equipment, having a thermal conductivity detector was employed to carry out the temperature programmed reduction (TPR). The TPR experiment was conducted by loading about 0.l0 g of the catalyst into the U-shaped reactor and oxidized at 750°C for 1 h by a gaseous stream containing 5% O_2 and the balance Helium. This was followed by the passage of the reducing gas i.e. 10 % H_2 in Helium at the rate of 50 mL/min, while the temperature was ramped from ambient to 750 °C at a rate of 10 °C/min. The sample was then cooled to ambient conditions.

4.3.5 X-ray diffraction

The crystalline structure of the new alumina supports was investigated by applying X-ray diffraction (XRD) technique, using a Rigaku Miniflex diffractometer operating at 40 kV and 20 mA. The samples were scanned at the rate of 2°/min every 0.02° during the interval: 10° to 90°. The Joint Committee on Powder Diffraction Standards (JCPDS) data was applied in identifying the phase(s).

4.3.6 Fourier transform infrared spectroscopy

FTIR spectral signatures of the Al_2O_3 phase were confirmed using Nicolet 6700 Thermo Fischer Scientific instrument for all the samples involved. About 3 mg of each catalyst was well mixed with ~0.4 g of KBr. The resulting mixture was then pelletized and subjected to the FTIR scan. Data were collected in the range of 400-4000 cm^{-1}

4.3.7 Raman spectroscopy

An iHR320 imaging spectrometer equipped with a CCD detector, from Horiba Scientific, was used to characterize the Al_2O_3 and $NiAl_2O_4$ phases, and to also investigate the nature of the deposited carbon in the spent samples. The scanning was conducted at a laser wavelength of 532 nm.

CHAPTER 5

DEVELOPMENT OF NOVEL Ni/Ce-Al_2O_3 CATALYSTS

5.1 Introduction

The novelty in this research originates from the synthesis of new catalysts for biomass gasification in a CREC riser simulator under turbulent fluidized bed conditions. Therefore this section is organized as follows:

- Synthesis of new ceria stabilized mesoporous alumina and applying it to support an appropriate amount of nickel catalyst.
- Characterization of the prepared catalyst using XRD, BET, SEM and TPR, TPD, FTIR and Raman Spectroscopy.
- Evaluation of the performance of the prepared catalysts for biomass gasification in a CREC riser simulator.
- Investigating the role of catalyst regeneration mode (calcination in air only, or calcination in air plus reduction in a hydrogen atmosphere) on the recyclability of the spent catalyst.

To the best of our knowledge, no such systematic work has been reported elsewhere.

5.2 Properties of the new ceria-doped alumina support

The samples involved were labeled as shown in Table 5.1.

Table 5.1 Composition of and nomenclature of the Ce-Al_2O_3 supports

Sample	Composition (Ceria/Al_2O_3)	Abbreviation
γ-Alumina	100	γ-Al_2O_3
Ceria-doped alumina	0.5/99.5	0.5Ce-Al[a]
Ceria-doped alumina	1.0/99.0	1.0Ce-Al[a]
Ceria-doped alumina	1.5/98.5	1.5Ce-Al[a]

The results and discussions of the findings and observations are reported in the following subsections.

5.2.1 Acidic properties

Figure 5.1 compares the ammonia TPD profiles for a commercial gamma alumina and the newly synthesized support.

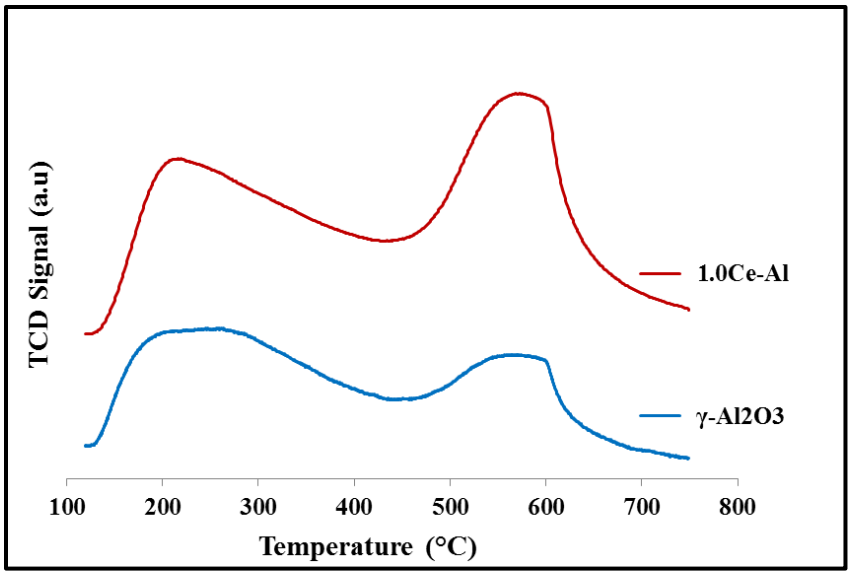

Figure 5.1: TPD profiles for a bare alumina and 1.0Ce-Al.

Both samples display regular features of gamma alumina, with ammonia desorption peaks around 225 °C and 580 °C each. The bare alumina sample desorbed more ammonia earlier (around 225 °C), while the ceria doped sample desorbed more ammonia at a higher temperature (peak around 580 °C). Therefore, the new support seems to have stronger acid sites than the commercial gamma alumina.

5.2.2 Thermal properties

The thermogram obtained for the three samples 0.5Ce-Al; 1.0Ce-Al and 1.5Ce-Al is depicted in Figure 5.2.

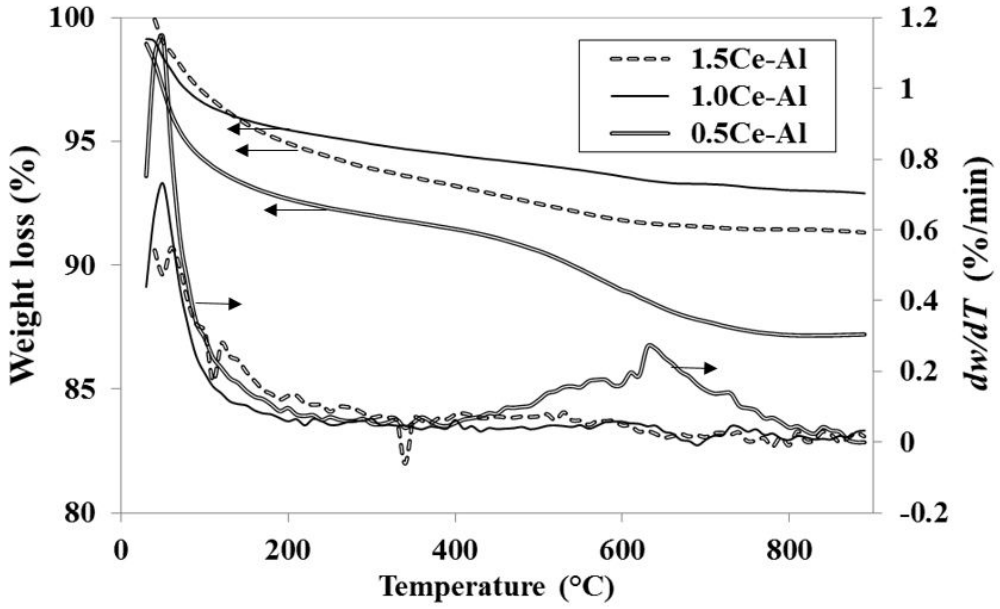

Figure 5.2: Thermograms of the newly-prepared supports.

All the samples showed stable behavior after the initial moisture weight loss (up to 200 ^{O}C). This is more evident considering the near zero values of the *dw/dT* profiles. Because the samples were initially calcined to 750 °C, most of the hydrated alumina hydroxides and boehmite phases must have been transformed into γ-phase. This is consistent with the findings from the thermodynamics of γ-Al_2O_3 hydration to boehmite [70]. Smith and coworkers [71] studied the phase-progression of nanostructured Al_2O_3 from synthesis to calcination at varying temperatures ranging from 300 to 1050°C. They observed that even at 300°C, the material was mostly in gamma phase (up to 60%), riddled with boehmite-phase. By increasing the calcination temperature, the boehmite fraction changed steadily to γ-phase until 950 °C, beyond which it disappeared completely and the whole matrix abruptly transformed to α-phase. Therefore, we propose

that in this work, the following reaction set might have occurred during the thermal analysis:

$$Ce_xAl(OH)_3.nH_2O \rightarrow Ce_xAl(OH)_4^- + H_3O^+ + (n-2)H_2O \quad (5\text{-}1)$$

$$Ce_xAl(OH)_4^- + H_3O^+ \rightarrow Ce_xAlOOH.nH_2O + (3-n)H_2O \quad (5\text{-}2)$$

$$2Ce_{0.5x}AlOOH.nH_2O \rightarrow Ce_xAl_2O_3 + (1+2n)H_2O \quad (5\text{-}3)$$

Since our calcination stopped at 750 °C, we expected that the alumina shown in Equation (3) will consist largely of the gamma phase [71,72]. Considering all the thermal profiles, we find that 1.0Ce-Al experienced the highest extent of this transformation (illustrated in Equations 1–3) into γ-phase during calcination, leaving behind a negligible amount in the boehmite-phase. Thus, it is evident that further addition of ceria (from 1.0 to 1.5 wt. %) into the alumina support matrix did not make any significant effect in improving the thermal stability. This conforms to the findings reported by Xiong et al. [73], for lanthanum stabilized alumina. For this reason, and the fact that dopants are often added in small quantities, 1.0 wt. % Ce seems to be a reasonable proportion to stabilize the alumina support.

5.2.3 Crystalline properties

Figure 5.3 illustrates XRD of the newly synthesized alumina supports after calcination. The dominant peaks occurred at diffraction angles (2θ) of 37, 43 and 67°. These correspond to the peaks in gamma alumina (JCPDS 01-074-2206). No notable

peak was observed for either ceria, CeO_2 (2θ = 28.5, 33, 47.6, 56.4°) or cerium aluminate, $CeAlO_3$ (2θ = 23.5, 33.5, 41.4 and 60˚) [60]. This may not be unconnected with the small amount of ceria incorporated or due to defect in the crystalline structure of the new mesostructured gamma alumina, which might have helped in a greater dispersion of the ceria dopant.

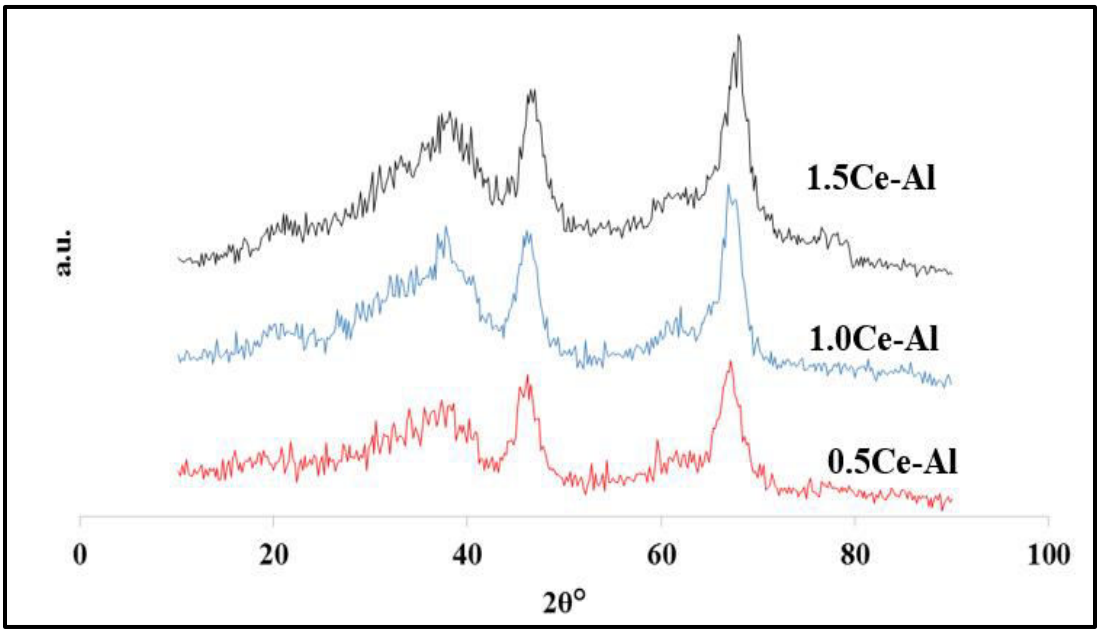

Figure 5.3: X-ray diffraction patterns for the newly prepared catalyst supports.

It is particularly important to note that all the supports showed similar XRD patterns irrespective of the differences in the amounts (0.5 to 1.5 wt. %) of ceria added. This indicates consistency and reproducibility of our synthesis methodology.

5.2.4 Textural properties

Figure 4 shows the adsorption-desorption isotherm of the 1.0%Ce-Al_2O_3 support calcined at 750 °C. The surface area, pore size distribution and average pore sizes were obtained from the Brunauer, Emmett and Teller analysis. The results shown in Figure 5.4 are typical of type IV adsorption isotherm of the IUPAC classification, because they exhibit a hysteresis loop (non-coincidence of the adsorption and desorption paths over some regions of higher relative pressures) [74].

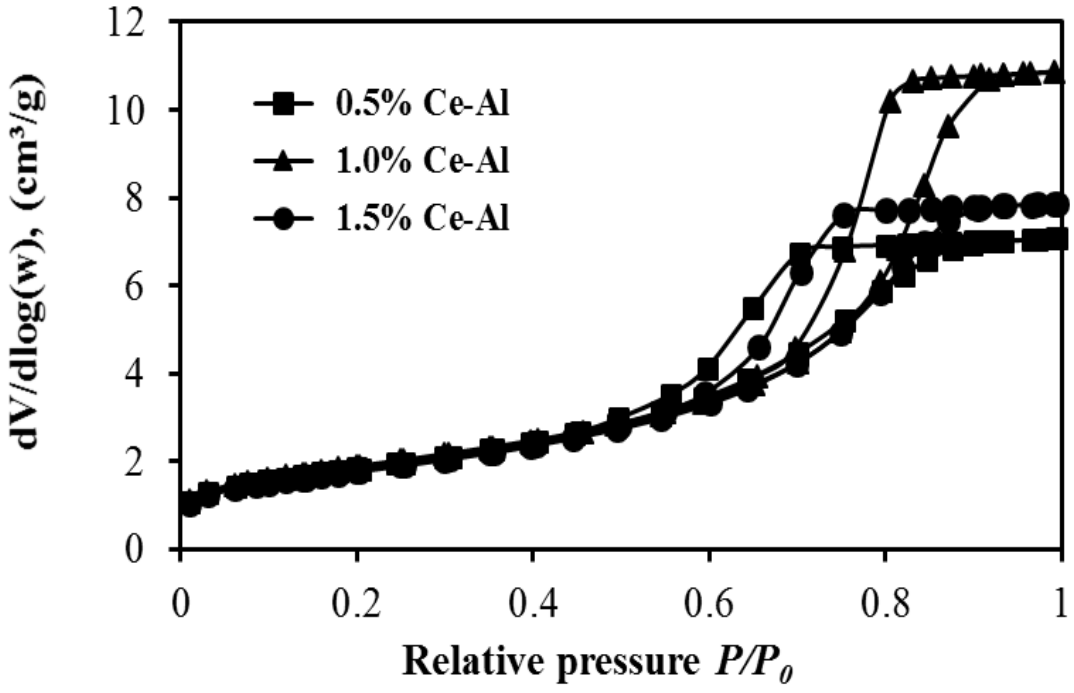

Figure 5.4: Adsorption/desorption isotherms of the Ce-Al_2O_3 supports.

It is evident from Figure 5.5 that the newly prepared supports are mesoporous. It this reported that these mesoporous alumina supports are characterized by a strong affinity for adsorbents [75].

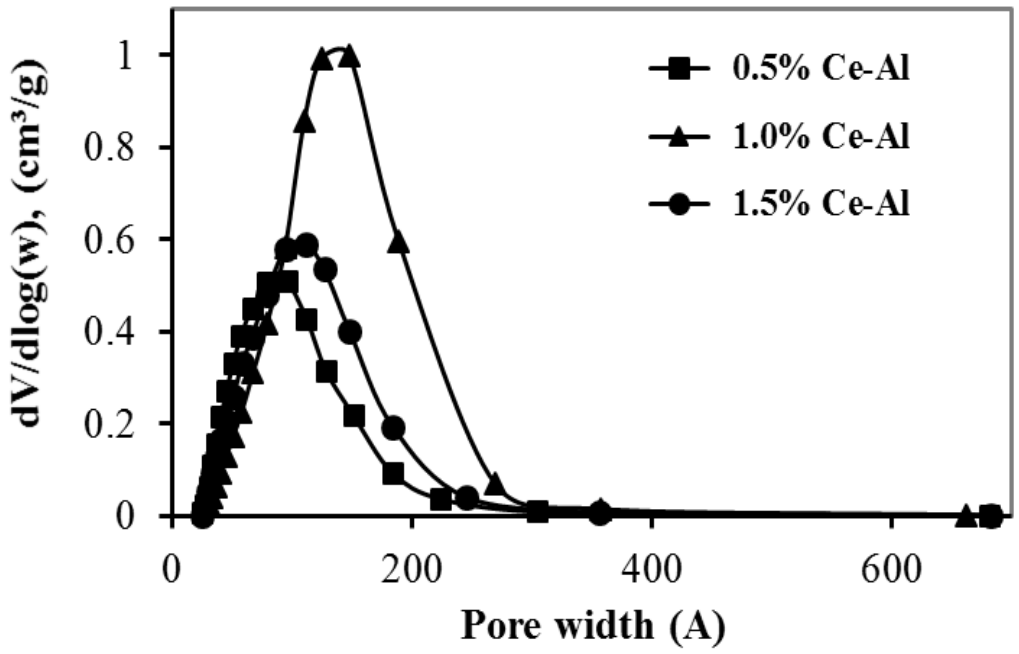

Figure 5.5: Pore size distribution of the Ce-Al_2O_3 supports.

At low pressures (up to $P/P_0 \approx 0.5$), both adsorption and desorption paths coincide, which is attributable to the occurrence of monolayer-multilayer adsorption, which is in turn indicative of weak adsorbate-adsorbent interactions [76]. The onset of the hysteresis loop indicates the beginning of the capillary condensation within the pores, which is a prominent feature of mesoporous materials [76]. The pores get filled up at an external pressure corresponding to the upper closure point of the hysteresis loop [74,75]. This fact is very vital in estimating the pore volume of the support.

The textural properties are summarized in Table 5.2. This quantifies the characteristics observed in Figure 5.4 and Figure 5.5. For the sake of comparison, the properties of a commercial γ-Al_2O_3 before and after calcination were given as reported previously by one of the authors [77].

Table 5.2: Textural properties of the new alumina supports.

Sample	S_{BET} (m^2/g)	BJH Cum. Des. SA (m^2/g)	V_T (cc/g)[b]	Pore width w (Å)[c]	Reference
γ-Al_2O_3 (as received)	233.00	-	0.253	-	[77]
γ-Al_2O_3[a]	18	-	0.10	-	[77]
0.5Ce-Al[a]	149	208	0.29	68	This work
1.0Ce-Al[a]	152	205	0.43	98	This work
1.5Ce-Al[a]	142.90	199.84	0.32	76.22	This work

[a] Sample calcined at 750 °C.
[b] Obtained from desorption component using BJH equation [66].
[c] Obtained from adsorption component using D-H equation [67].

BET surface areas of the calcined supports fall within a range of 143-152 m^2/g, with the 1.0%Ce-Al having the highest surface area. Whereas the other supports appear to have lesser pore widths, implying that their internal mesoporosity contributed significantly to the total surface area. Thus, the BET surface area for all the samples fell within same range and thereby indicating that the varying amount of ceria dopant did not significantly affect the surface area.

5.2.5 Structural properties

The newly synthesized samples were characterized by scanning electron microscopy to ascertain their structural properties. This is illustrated in Figure 5.6. The support denoted as1.0%Ce-Al obtained by doping 1.0% Ceria on Alumina exhibits a heterogeneous structure. This is owing to its inherent cation defect resulting from its characteristic tetragonally deformed spinel type structure of gamma alumina [72].

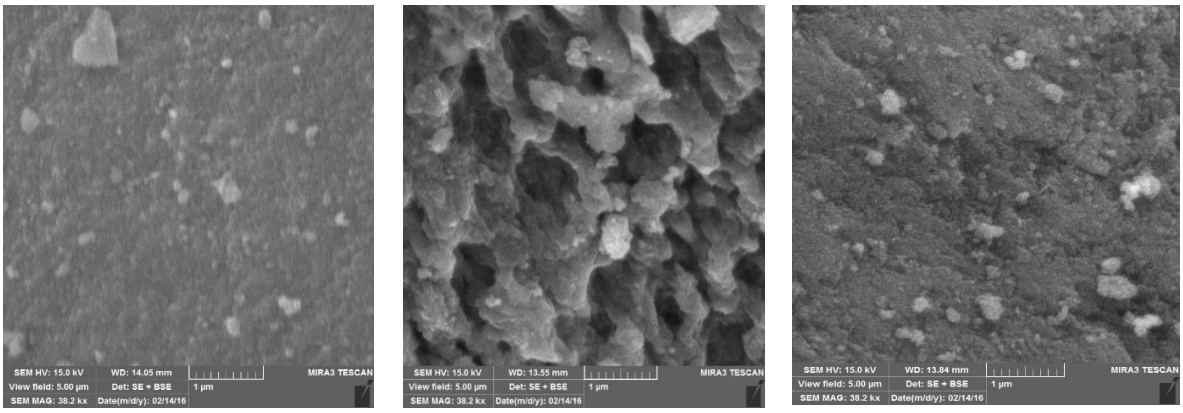

(a) 0.5%Ce-Al (b) 1.0%Ce-Al (c) 1.5%Ce-Al

Figure 5.6: SEM images of the new ceria-doped alumina supports.

The SEM images further confirmed that the three supports exhibited an excellent dispersion of the ceria dopant. This is attributed to adequate mixing and controlled hydrolysis during the synthesis work. In particular, 1.0% Ce-Al support appears to have a network of pores with the dopant phase particles dispersed uniformly within the mesoporous alumina matrix. This is also evident from the result of pore size distribution (See Figure 5.5). This catalyst structure can improve percolation of reactants to the catalyst active sites, and could, therefore, result in significant catalytic activity. Referring to Table 5.2, it is obvious that addition of ceria has helped in conserving the textural properties of the newly synthesized ceria-doped alumina even after calcination at high temperature. In the light of these morphological and textural findings, we suggest, therefore, that the high oxygen carrying capacity of ceria coupled with the synthesis methodology which ensured high dispersion of ceria within the alumina matrix, have both assisted to stabilize the newly prepared alumina support. While the interaction

between alumina and the ceria dopant has been shown to be moderate, it is sufficient to prevent the phase transformation of gamma to alpha phase up to a temperature of 750 °C. This is probably due to the ability of ceria to prevent excessive loss of bridged hydroxyl species [78] and hence mitigated the excessive loss in surface area during high-temperature calcination.

5.2.6 Deconvolution of pore size distribution

Deconvolution technique was applied to investigate the apparent pore network of 1.0Ce-Al sample using its pore size distribution, as envisaged in its texture and structure. We saw that in Figure 4b the pore size distributions were apparently broad (in the range of 2.4-25 nm), implying that all the new supports possess mesoporous–broad pore size distribution, but within the same span. In particular, sample 1.0Ce-Al exhibit a relatively broader distribution, which hints to a possibility of occurrence of differing pore networks. In order to investigate these networks, we carried out deconvolution of the pore size distribution as follows:

$$f(w) = f(w_0) + \sum_{i=1}^{n} \frac{A(i)}{w(i)\sqrt{\pi/2}} e^{-2\frac{(x-x_c(i))^2}{w(i)^2}} \qquad (5\text{-}4)$$

Where $f(w)=dV/dlog(w)$, $A(i)$, $w(i)$ and $x_c(i)$ refer to the area, width, and center of i^{th} peak respectively. n refers to the number of peaks, which is chosen such that the sum of square errors (*SSE*) between the Gaussian model $f(w)$ and $dV/dlog(w)$ experimental points is minimized. Thus, the pore size distribution for 1.0CeAl was deconvoluted in PeakFit® software, and shown in Figure 5.7.

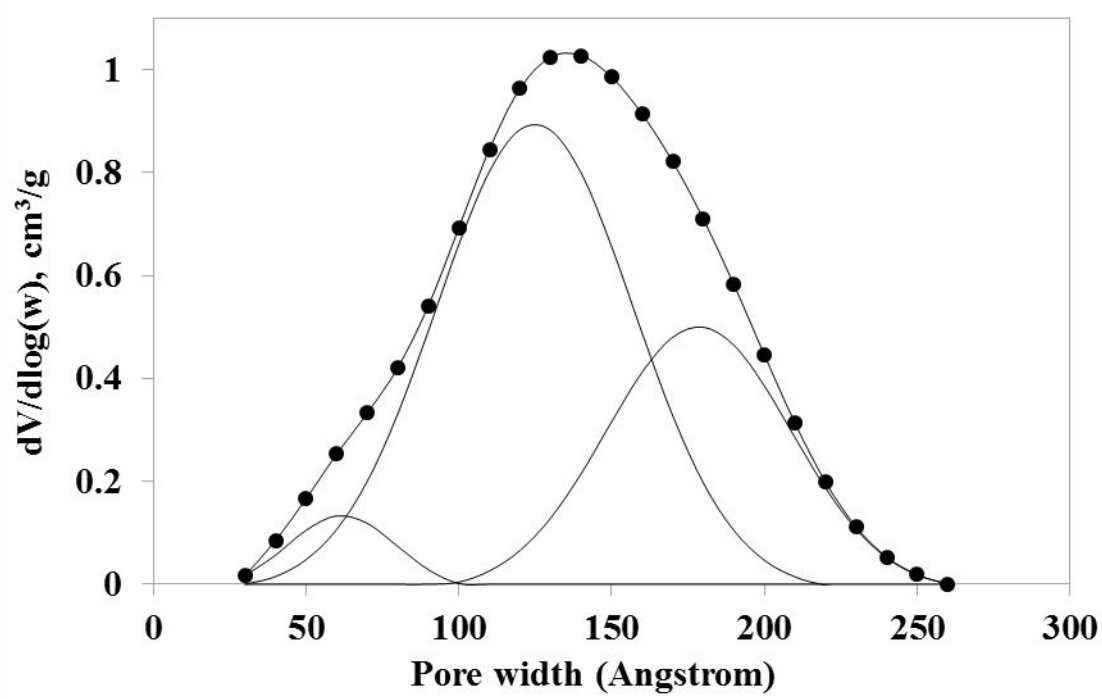

Figure 5.7: Deconvolution of pore size distribution for 1.0Ce-Al.

The curves within the broad distribution in Figure 5.7 represent the components into which the latter was decomposed. Therefore, the pore sizes of the new catalyst support could be grouped into three Gaussian distributions with most probable values of 62, 125 and 179 Angstrom, and corresponding to volume-fractions of 0.06, 0.62 and 0.32 respectively. These results can be interpreted as follows. The sample denoted as 1.0Ce-Al is largely constituted by pores centering around 125 Angstrom interconnected with broader groups of network centering around 179 Angstrom. This type of pore networks will promote percolation of reactants into the catalyst particle interiors [79], improve the heat and mass transfer properties and lower the pressure drop [80]. Therefore, sample 1.0Ce-Al would make a better catalyst for conversion of intermediate products of biomass gasification than the narrowly distributed 0.5Ce-Al or 1.5Ce-Al. Thus, the

synthesis methodology adopted in this work has given some new insights into developing a stable mesoporous alumina supports, with high post-calcination surface area and desirable pore volume and pore size distribution.

5.2.7 Desorption kinetics

We investigated how the Ceria dopant influences the catalytic properties of the parent alumina phase by conducting ammonia desorption kinetics. The desorption rate constant plus activation energy for ammonia desorption from the surface of the support could be used to ascertain their potential performance in steam biomass gasification. Therefore we adopted the method of Cvetanovic and Amenomiya [81–85], involving the following assumptions:

(i) Surface of the support is homogeneous for ammonia adsorption such that the desorption rate constant obeys Arrhenius law and is independent of the surface coverage

$$k_{des} = k_{des0} Exp\left(-\frac{E_{des}}{RT}\right) \tag{5-5}$$

(ii) Once desorbed, there is no re-adsorption of ammonia molecules onto the surface of the support.

(iii) The rate of desorption of ammonia from the surface varies linearly with surface coverage.

(iv) The concentration of ammonia gas remains uniform throughout the catalyst bed.

(v) Temperature of desorption varies linearly with time.

At high gas flow rate across the bed, assumption (ii) is satisfied. Assumptions (iv) and (v) are satisfied by appropriately selecting the operating conditions. White [86] reported that some porous catalysts may experience ammonia re-adsorption due to their pore network, and thereby exhibiting low activation energy. This will be investigated with respect to the recent contributions for ammonia TPD desorption kinetics in gamma alumina catalyst systems.

A differential material balance on the catalyst bed for the desorbing ammonia molecules give the following equation:

$$-V_m \frac{d\theta_{des}}{dt} = -k_{des0}\theta \exp\left(-\frac{E_{des}}{RT}\right) \tag{5-6}$$

By chain rule, and the assumption that temperature varies linearly with time, we have;

$$\frac{d\theta_{des}}{dt} = \frac{d\theta_{des}}{dT}\frac{dT}{dt} = \beta \frac{d\theta_{des}}{dT} \tag{5-7}$$

where β is the heating rate in (°C/min).

θ_{des} represents the fractional surface coverage (i.e. the concentration of ammonia on the surface of the support). Thus,

$$\theta_{des} = 1 - V_{des} / V_m \tag{5-8}$$

Combining equations (6) and (7), we obtained

$$\frac{d\theta_{des}}{dt} = \frac{k_{des0}}{V_m \beta}\theta_{des} \exp\left[-\frac{E_{des}}{R}\left(\frac{1}{T} - \frac{1}{T_m}\right)\right] \tag{5-9}$$

Where T_m is the centering temperature, chosen as the average of the temperature vector, so as to circumvent the stiffness of the nonlinear regression problem and to obtain kinetic parameters with low values of cross-correlation coefficients. Equation 9 may be regressed directly or transformed into an algebraic equation by separating the variables and integrating. Therefore, by applying the initial value condition that $\theta(T_0) = 1$, where T_0 is the temperature of adsorption, and also the temperature at which the desorption begins, we obtained the following algebraic nonlinear form:

$$\ln\theta_{des} = \frac{k_{des0}}{V_m\beta}\exp\left(\frac{E_{des}}{RT_m}\right)\left[T\exp\left(-\frac{E_{des}}{RT}\right)+\frac{E_{des}Ei\left(-\frac{E_{des}}{RT}\right)}{R}-T_0\exp\left(-\frac{E_{des}}{RT_0}\right)-\frac{E_{des}Ei\left(-\frac{E_{des}}{RT_0}\right)}{R}\right] \tag{5-10}$$

Where the exponential integral, $Ei(x)$ is defined as:

$$Ei(x) = -\int_{-x}^{\infty}\frac{e^{-x}}{x}dx \tag{5-11}$$

This function is available in MATHEMATICA software. The instantaneous volume of ammonia desorbed, $V_{des}(t)$ was obtained by integrating the NH_3-TPD concentration-time profile from 0 to t. V_m is the cumulative volume of ammonia at the end of the desorption program, corresponding to the total area under C-t curve while θ_{des} was obtained by applying Equation 8 accordingly. Alternatively, we can obtain the coverage directly from the TPD calibrated data using the elation;

$$\theta_{des} = \frac{\sum_{0}^{t}C(t)dt}{\sum_{0}^{t_{end}}C(t)dt} \tag{5-12}$$

The data was fitted against the model (Equation 10) in MATHEMATICA using NonlinearModelFit command. This command minimizes the sum of squares of the residuals between the model and experimental data points. The criteria for assessing the goodness of the fit are the coefficient of determination, R^2 at 95% confidence interval (i.e. α = 0.05 level of significance), standard error and p-values. The results for the kinetic parameters are given in Table 5.3

Table 5.3: Desorption kinetic parameter estimates.

Sample	E_{des} (kJ/mol)	k_{des} (cm^3/min.K)	R^2	*p-value*
γ-Al_2O_3	27.60±0.80	0.0311±0.0005	0.998	0.000
1.0Ce-Al	35.56±2.00	0.0317±0.0010	0.993	0.000

Table 5.3 shows that the coefficients of determination R^2 were greater than 0.99 for both samples, implying that the fit is excellent. Moreover, the standard error at 95% confidence interval for both E_{des} and k_{des0} are low indicating that the phenomenological model is acceptable and satisfactorily represents the experimental data. Statistical p-values were effectively zero for both cases, implying that the model parameters, k_{des0} and E_{des} are not only non-zeroes, but also produce model predicted amounts of ammonia desorbed that are not significantly different from the experimental values along the whole temperature range. This is confirmed by the parity plot for both samples studied [See Figure 5.8]. Furthermore, since the proposed model is one that is non-linear, the residuals between the fitted and experimental values should show some non-linear, and non-random pattern.

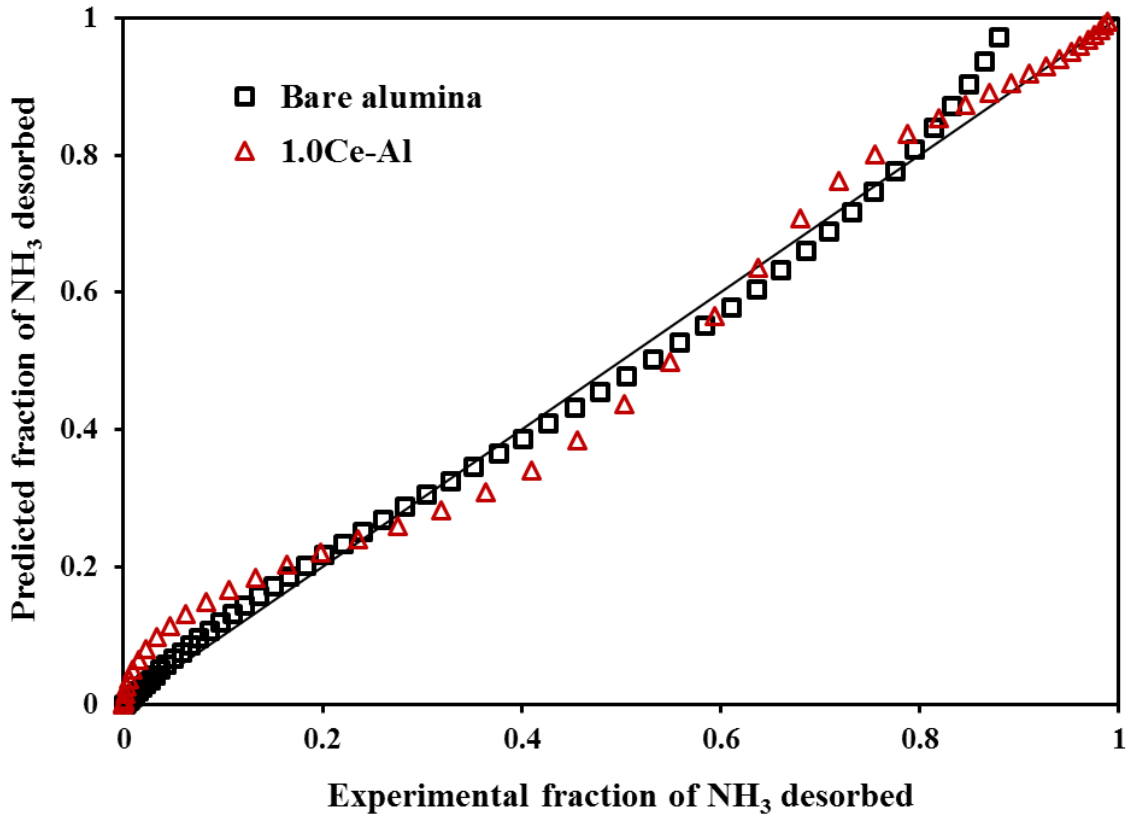

Figure 5.8: Parity plot for the amounts of NH_3 desorbed from 1.0Ce-Al and γ-Al_2O_3.

Interestingly, the residual plot, depicted in Figure 5.9 shows that the distribution is non-normal, and therefore the statistical normality assumption for linear systems is not obeyed. In fact, this is a very important result, as it further reiterates the non-linearity of the relation between the quantities of ammonia desorbed versus temperature.

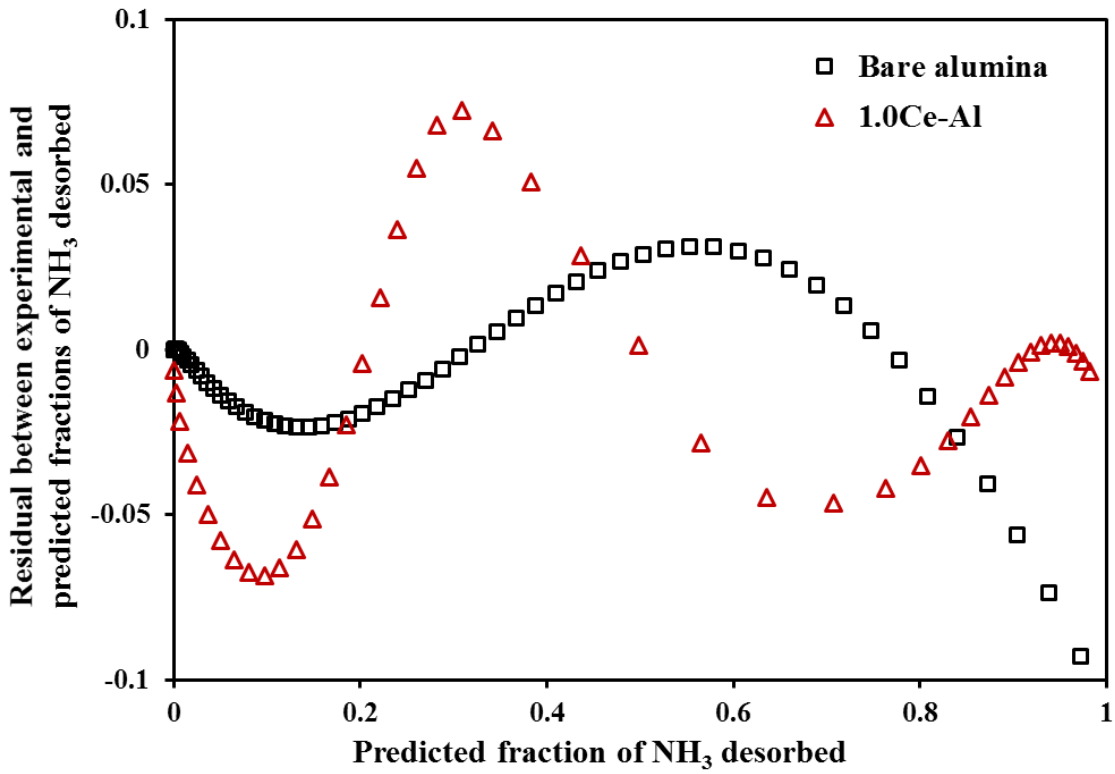

Figure 5.9: Residual plot for bare alumina and 1.0Ce-Al

It is seen from Table 5.3 that bare γ-Al_2O_3 has a lower desorption activation energy of 27.6 kJ/mol as compared to the new 1.0 wt. % Ceria-doped-Al_2O_3 support which has only 35.56 kJ/mol. Considering the total amounts of ammonia desorbed, we find that 1.0Ce-Al sample has a relatively lower amount (6.87 cm^3 NH_3/g-sample) than the bare support, which has about 7.60 cm^3 NH_3/g-sample. This justifies the higher ammonia desorption activation energy of 1.0Ce-Al according to the authors [84,85,87]. The slight over-prediction around the extreme ends of the desorption process, as seen in Figure 5.8, can be explained as follows. At low temperature, desorption process is slow, and hence the rate is overestimated by the surface coverage (which is high initially) [See Figure 5.11].

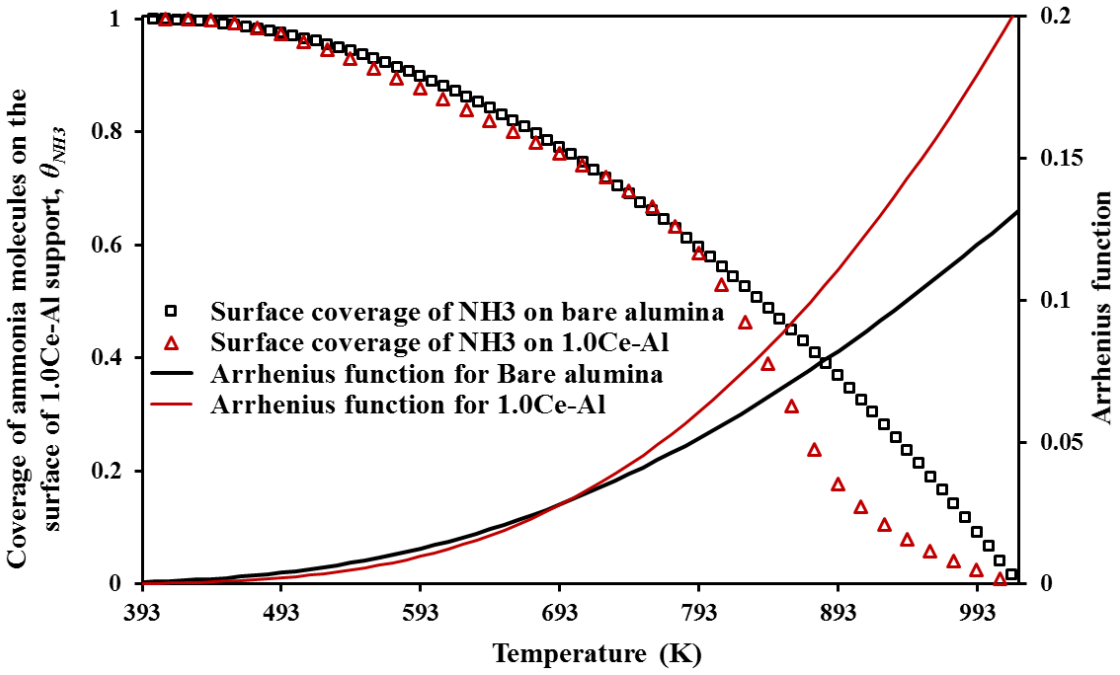

Figure 5.10: Surface coverage and Arrhenius function for 1.0Ce-Al and bare alumina.

Similarly, the rate is slow at the end of the desorption process considering the fact that most of the ammonia molecules in the vicinity of the alumina surface have been desorbed. Hence, the rate is overestimated by the Arrhenius term of the rate equation, which is exponential, and very significant at high temperature [See Figure 9]. This is observed for the bare alumina. However, for 1.0Ce-Al, we observed that towards the end of the desorption process, there was better agreement between the theoretical and experimental fractional coverage. Overall, we conclude that the first order desorption satisfactorily predicts the ammonia desorption kinetics of the two samples.

In summary, the methodology developed for synthesizing Ce-doped-alumina is highly effective in stabilizing the support and conserving its post-calcination surface area. Ceria dopant of 0.5 wt. % is sufficient for stabilizing mesoporous- or gamma- alumina for

gasification applications. However, thermal gravimetric analysis indicates that 1.0 wt. %Ceria will give a more stable γ-phase alumina, upon calcination to 750 °C. Morphological and textural properties indicate that ceria is well dispersed in the alumina phase, such that the oxygen storage capacity of ceria has helped in preventing excessive loss of bridged hydroxyl species, and hence avoided excessive loss in surface area. At 1.0 wt. % ceria doping, a network of mesopores with pore size distribution suitable for tar cracking reactions was formed. This could lead to a better biomass conversion to fuel gas or enhance the selectivity to light olefins during catalytic heavy oil cracking. Mathematical treatment in the form of deconvolution of the pore size distribution revealed that the sample (1.0%Ce-Al), with a significantly broader pore size distribution, indeed possesses largely two groups of pores centering around 125 and 179 Angstrom. These pore network could enhance reactants percolation to the catalyst active sites. The activation energy of ammonia desorption for 1.0Ce-Al was 35.56 kJ/mol unlike the bare alumina with 27.6 kJ/mol. This increase indicates some moderate interaction between the dopant and the support matrix. This will allow for reactants accessibility to the catalysts active sites, and hence enhance water gas shift and tar cracking reactions, which dominate steam gasification of biomass. Overall, the sample denoted as 1.0%Ce-Al exhibits better catalytic properties in terms of higher post-calcination surface area, texture, structure, product desorption capability, and higher pore volume, and could, therefore, accommodate more active metal in a well-dispersed fashion and without unwanted agglomeration.

5.3 Properties of the new Ni/Ce-Al_2O_3 catalysts

5.3.1 Surface properties

The surface and textural properties of the best ceria-modified alumina support were investigated via nitrogen/desorption experiments. Figure 5.11 shows the nitrogen adsorption-desorption isotherm along with the pore size distribution for the ceria-modified support. The data between relative pressure (P/P_0) values from 0 to 0.3 was used with the linearized form of BET equation to calculate surface area. The BET surface area as obtained from the adsorption branch of the isotherm is 152 m^2/g, while the average pore size determined by BJH method from the desorption branch is 0.429 cm^3/g

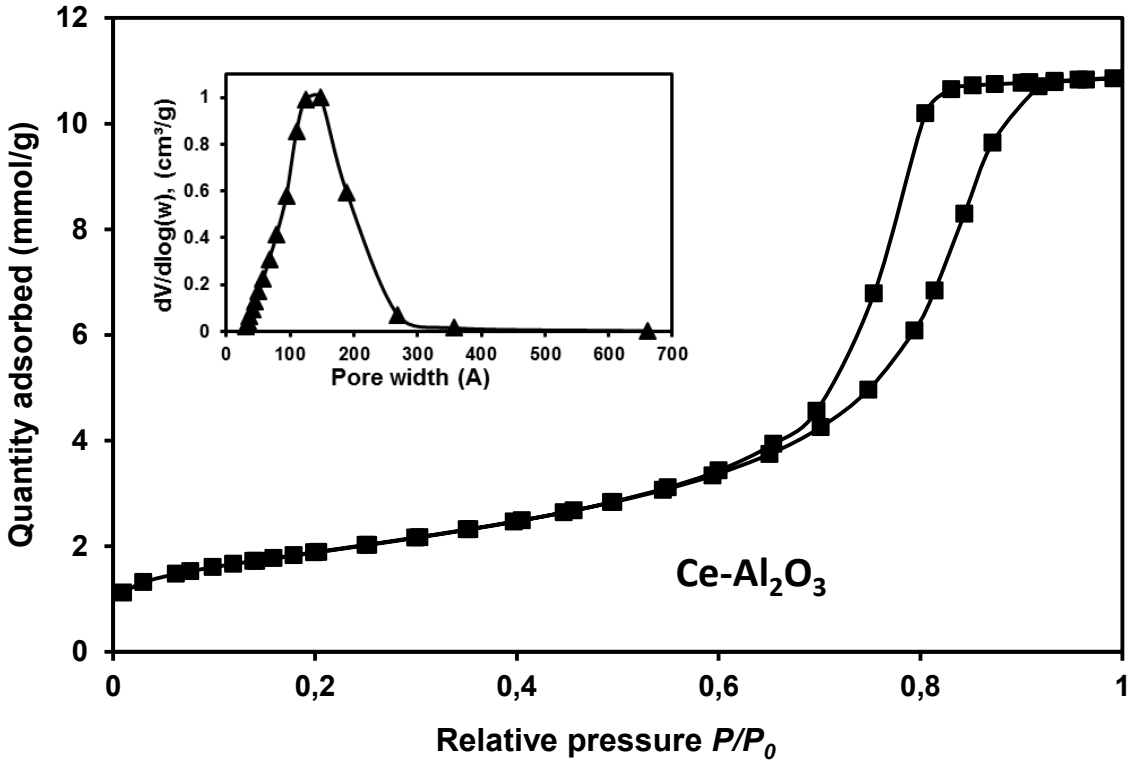

Figure 5.11: BET analysis for the fresh Ce(1)-Al_2O_3 after calcination at 750 °C.

This post-calcination textural parameters for the modified support showed that the 1.0 wt. % ceria is sufficient to stabilize the support, unlike bare commercial γ-alumina whose surface area could decrease from 233 to as low as 18 m^2/g when calcined to 750 ℃ [77]. Thus, the calcined support could withstand the harsh gasification environment without any deformation. Henceforth, we shall refer the newly prepared calcined support as Ce-meso-Al_2O_3 or simply alumina support.

5.3.2 Crystalline properties

Figure 5.12 depicts the X-ray diffraction patterns of the nickel ceria-alumina catalysts. The dominant peaks observed at diffraction angles of 38, 46.2 and 67° are attributable to γ-alumina (JCPDS: 01-074-2206). It should be noted that the peaks actually shifted slightly to the right (i.e. from 37° to 38°, and from 43° to 46.2°), as compared to those in the reference XRD card. These shifts are likely due some level of coalescence of Al_2O_3 grain boundaries, resulting in a change of the lattice parameters. Ceria (CeO_2) and cerium aluminate $CeAlO_3$ have characteristics peak around 2θ = 28.5, 33, 47.6, 56.4°; and 2θ = 23.5, 33.5, 41.4, 60˚ respectively [88]. The non-appearance of these peaks is partly due to the small amount of ceria (1.0 wt%) doped, and partly due to defects in the crystalline structure of the new mesoporous alumina, which has helped in a high dispersion of the ceria dopant. The successive incipient wetness methodology adopted, led to the high dispersion of nickel at all loadings (5–20 wt%), as evident by the broad XRD peaks.

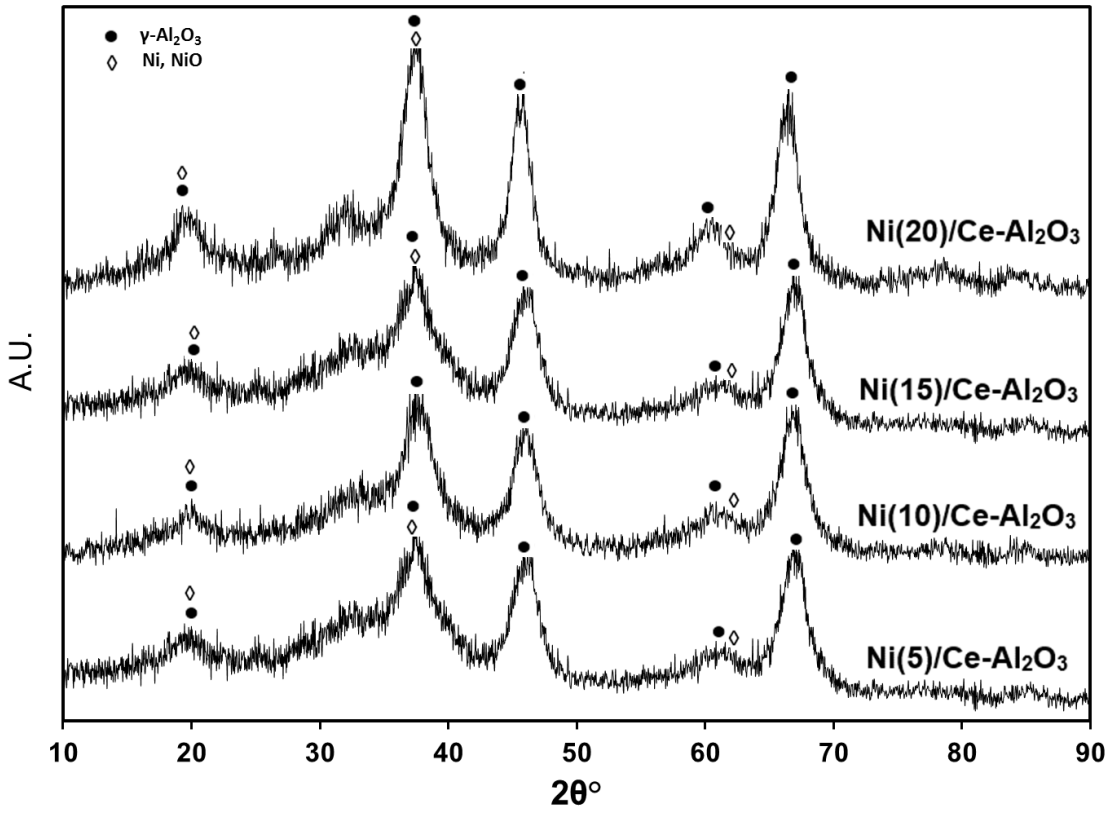

Figure 5.12: X-ray diffraction patterns for the newly prepared catalyst supports.

It should be noted that the highest nickel loading was limited to 20 wt%, in order to avoid the possibility of metal sintering or agglomeration of nickel on Al_2O_3 at higher loading [89].

5.3.3 Catalyst dispersion on the support material (TEM)

Figure 5.13 shows the TEM image of the fresh Ni(20)/Al_2O_3 catalyst. The dispersion is excellent due to our successive metal impregnation protocol. The nickel particles are represented by the dark spots in the TEM image. Nickel particles are mostly dispersed on

the surface of the ceria-doped alumina support, with a few observable clusters of sizes far below 100 nm. Thus, small crystallites of nickel were successfully prepared on the surface of the new ceria-doped-alumina. It is logical also, that the rest of the Ni(x)/Al_2O_3 (i.e. x = 5, 10 and 15 wt%) will have much better particle dispersion since the successive metal impregnation protocol was adopted.

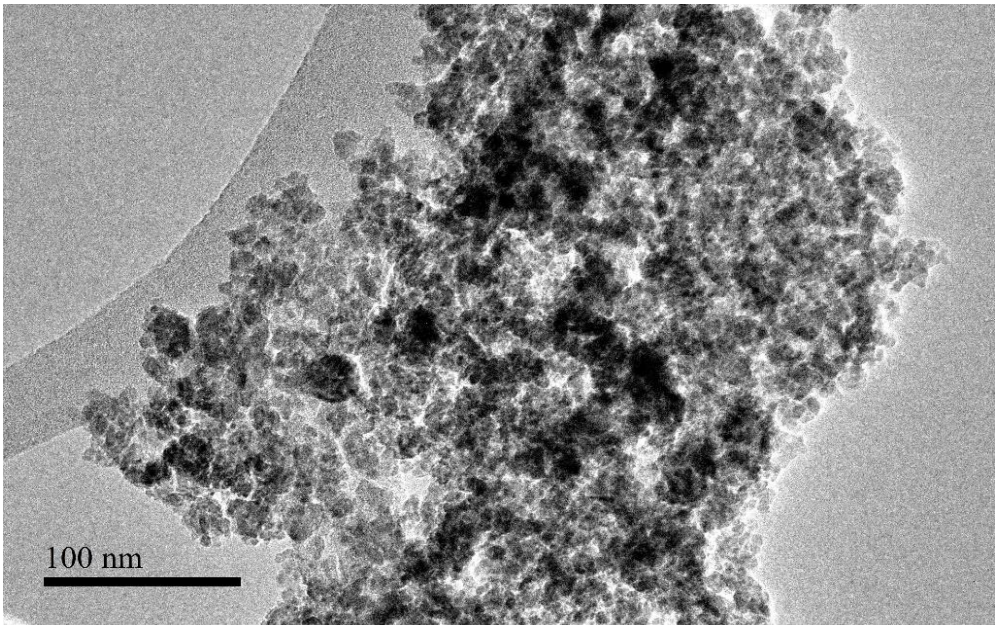

Figure 5.13: TEM image of Ni(20)/Ce-Al_2O_3 catalyst.

It should be noted that the highest nickel loading was limited to 20 wt. %, in order to avoid the possibility of metal sintering or agglomeration of nickel on Al_2O_3 at higher loading [89].

5.3.4 Raman spectroscopy

Raman spectroscopy is a non-destructive technique for investigating the extent of dispersion of active metal on the support [90]. Therefore, it was applied to investigate nickel (Ni°) or nickel oxide (NiO or $NiAl_2O_4$) and ceria (CeO_2) phases present in the as-synthesized catalysts (See Figure 5.14). Bare Al_2O_3 support does not show Raman active modes [91]. On the other hand, pure ceria crystallites show intense Raman spectral peak around ~463 cm^{-1}, which is attributed to the symmetrical stretching vibrational mode of $Ce\text{-}O_8$ crystal unit [92].

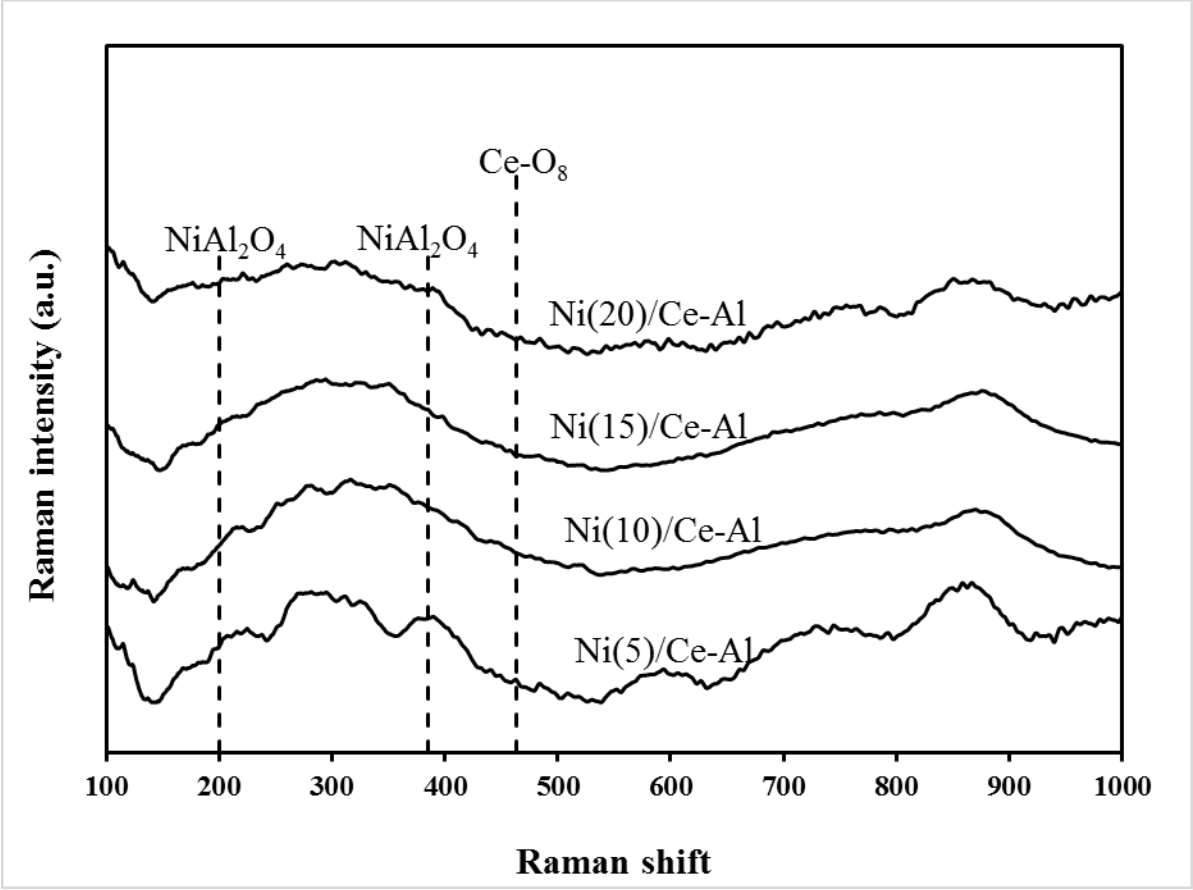

Figure 5.14: Raman spectra of the freshly prepared catalysts.

Nickel supported on gamma alumina exhibits Raman spectral peaks at 200, 375 and 600 cm^{-1}. Therefore the peaks within this range as depicted in Figure 5.14 could be attributed to Ni/Al_2O_3 or $NiAl_2O_4$ [93]. Comparing all the Raman spectra of $Ni(x)/Ce\text{-}Al_2O_3$ samples, we see that there is gradual flattening of the peak ranging between 200 cm^{-1} and 375 cm^{-1}. This is obviously due to the increasing nickel concentration on the $Ce\text{-}Al_2O_3$ support which affects the crystalline nature of the Ni/Al_2O_3 interacting phases. Considering, the results shown in Figure 5.14, we can see that there are no observable peaks CeO_2 phases in the newly synthesized catalyst. Therefore, both ceria crystallites is well dispersed on the Al_2O_3 support. This high level dispersion of ceria on the support is attributable to its low concentration and the unique properties at 1.0 wt.%) and the proper mixing conditions.

5.3.5 Acidity

The net acid strength of the prepared catalysts was investigated via ammonia TPD. Moreover, the TPD spectra are useful in assessing the nature of the available acid sites present in the catalysts. Figure 5.15 illustrates the ammonia TPD of the as-prepared $Ni(x)/Ce\text{-}Al_2O_3$ catalysts.

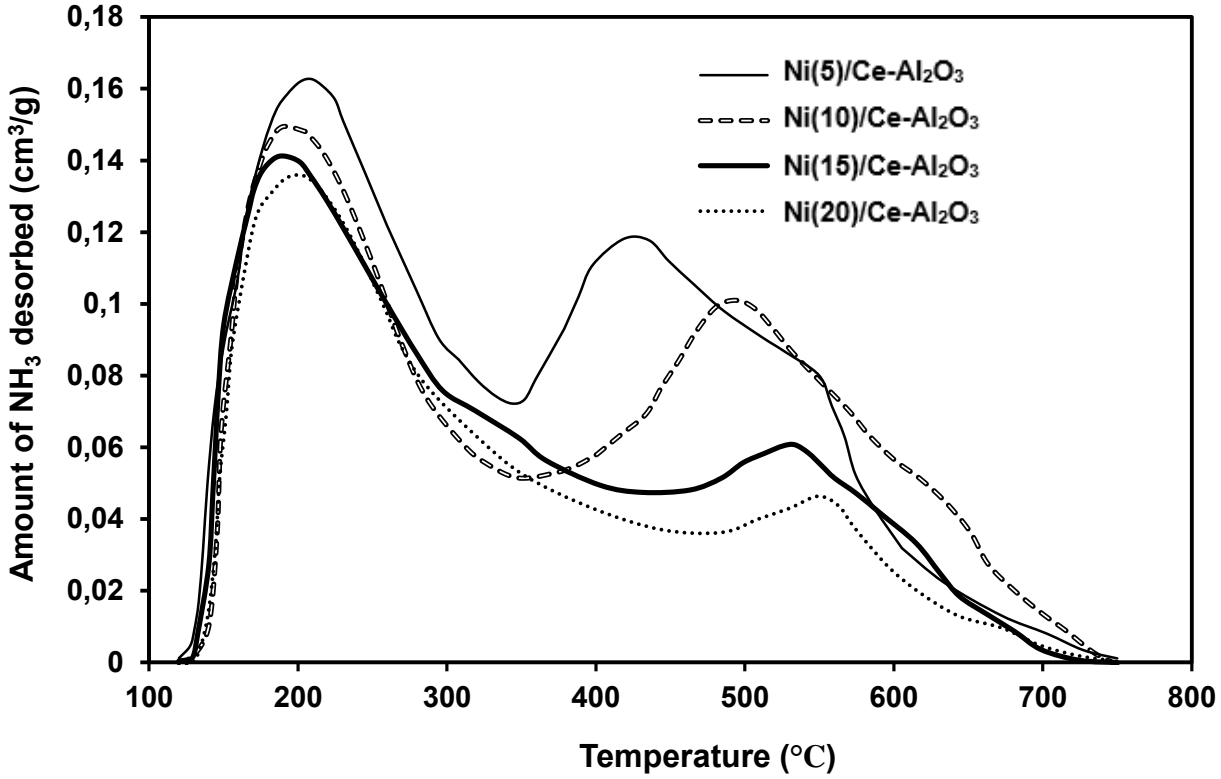

Figure 5.15: TPD profiles of as-synthesized Ni/Ce-Al_2O_3 catalysts

It is seen that most of the NH_3 adsorbed on the weak acid sites were desorbed at $T < 300$ °C. There is a significant decline in the volume of these low-temperature peak, as the nickel loading is increased from 5 wt% to 10 wt%. From 10 wt% nickel loading to 20 wt% these peaks virtually collapsed into a similar trajectory within the range $120 < T < 350$ °C. As regards the high-temperature desorption peaks, it is seen that the peak center is gradually displaced forward as the nickel loading increases. The forward shift of the peaks is most significant from 5 to 10 wt% nickel loading, followed by the shift from 10 to 15 wt% and then from 15 to 20 wt%. The implication is that there could be convergence of these high temperature desorption peaks, as the nickel content is successively increased beyond 20 wt%. This hints to a possible optimum for the nickel

loading on this new Ce-Al_2O_3 support, beyond which we may encounter agglomeration of the nickel species on the surface of the support. Table 5.4 gives the total acidity for the four samples.

Table 5.4: Acidity of the newly synthesized catalysts.

Catalyst	Total acidity (mL NH_3/g-sample)
Ni(5)/Ce-Al_2O_3	7.20
Ni(10)/Ce-Al_2O_3	6.25
Ni(15)/Ce-Al_2O_3	5.25
Ni(20)/Ce-Al_2O_3	4.58

At 5.0 wt% nickel loading, the catalyst exhibits a relatively higher acidity (7.2 mL NH_3 desorbed per gram of the catalyst). As the nickel loading was increased the total acidity gradually decreases. This is expected by observing the relative areas of the curves shown in Figure 5.15. This is due to coordination of more nickel species with the electron deficient aluminum Lewis acidic centers [61,94]. This is observable in Figure 5.15, as the decrease in the volume of the high-temperature desorption peak.

5.3.6 Reducibility

TPR spectra is useful for extracting information regarding the metal catalyst reducibility, peak reduction temperature, and metal/support interaction. The peak

reduction temperature informs us about the temperature range in which we could regenerate the spent catalysts. The TPR profiles for the four catalysts are shown in Figure 5.16.

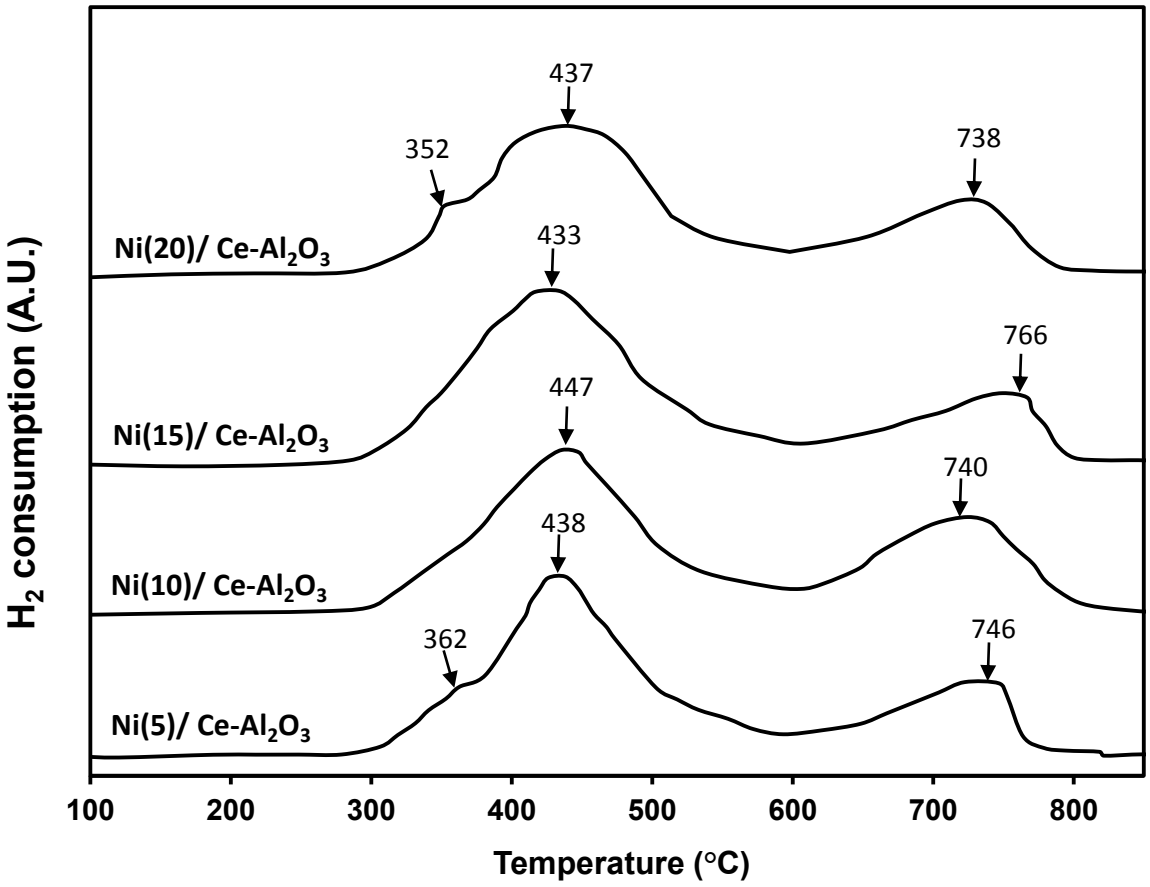

Figure 5.16: TPR profiles of as-synthesized Ni/Ce-Al_2O_3 catalysts

In general, all the catalysts exhibited two major reduction peaks around 433 – 447 °C and 738-766 °C. The low-temperature peak denote surface Ni^{2+} species which are easily reducible, while the high-temperature peaks indicate $NiAl_2O_4$ spinel, in which the nickel interacts strongly with Al_2O_3 support. This is in conformity with the report of

Richardson and coworkers [95], that Ni^{2+} species are reduced within the range 325−700 °C, whereas nickel aluminate is reduced beyond 650 °C. The volume of the low-temperature peaks increases with a gradual increase in nickel loading, providing more reducible Ni species. In addition to the two main peaks, a small kink (around 350 – 360 °C) occurs in Ni(5)/Ce-Al_2O_3 and Ni(20)/Ce-Al_2O_3 catalysts near the low-temperature peaks. A second derivative of the TPR spectra (H_2-time data) indicates that these kinks are not local maxima. Instead, they constitute low-temperature peak broadening, which will increase the number of reducible species at low temperature. A pairing is observed in the behavior of the peak shifting with an increase in nickel loading. Ni(5)/Ce-Al_2O_3 and Ni(10)/Ce-Al_2O_3 exhibit low-temperature peaks at 438 and 447 °C respectively. The corresponding values for Ni(15)/Ce-Al_2O_3 and Ni(20)/Ce-Al_2O_3 were 433 and 437 °C respectively. This pair shifting for an incremental nickel loading (i.e. 5 to 10 wt. % and 15 to 20 wt. %), suggests a relative increase in Ni/Al_2O_3 interaction than Ni/$CeAlO_3$. That is, at a fixed ceria loading (1.0 wt. %), an increase in nickel loading results in an increasing tendency to form nickel aluminate, rather than Ni-O-Ce species. Overall, we conclude that Ni(10)/Ce-Al_2O_3 catalyst, which shows the highest low-temperature reduction peak (i.e. 447 °C) may not be the optimal nickel loading on the newly synthesized Ce-Al_2O_3 mesoporous support.

5.3.7 Fourier transform infrared spectroscopy

The spectrum (See Figure 5.17) in the range 400–1000 cm^{-1} depicts a fairly crystalline structure with and void of sharp peaks. The broad band, extending

within the range of 400–700 cm^{-1} particularly denotes γ-Al_2O_3 phase, with its characteristic amorphous or disordered structures [96].

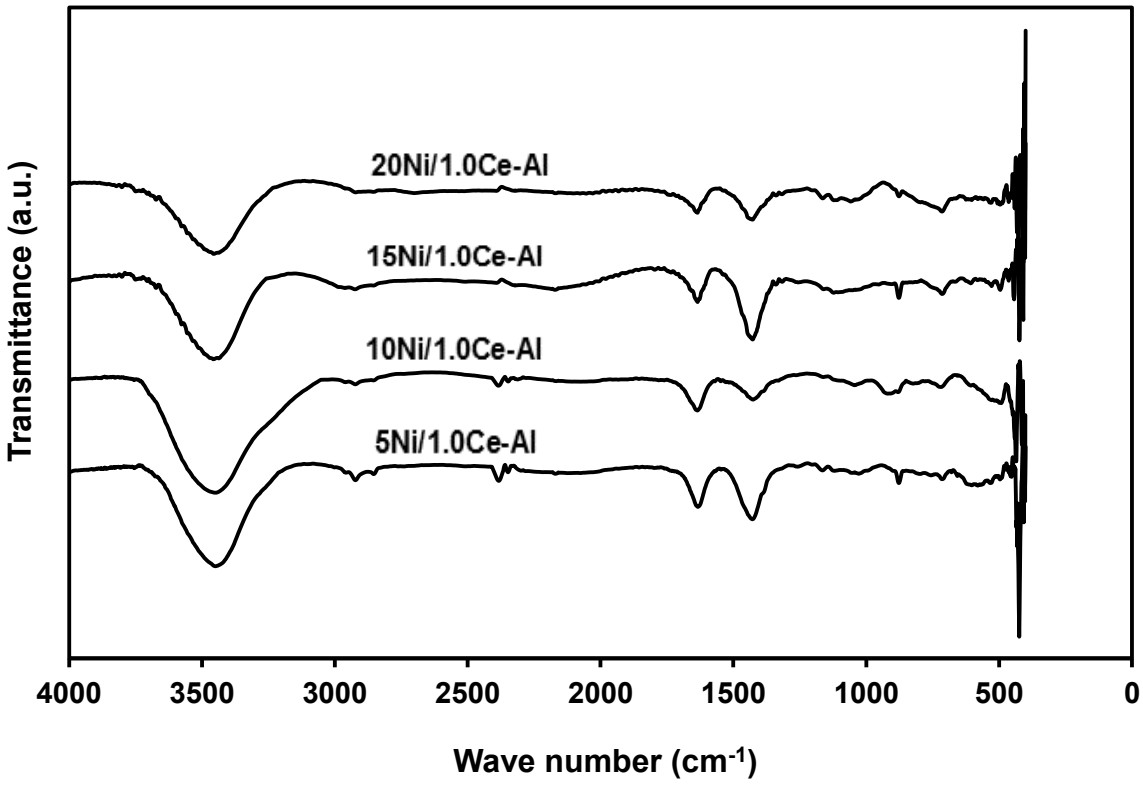

Figure 5.17: Infrared spectra of the Ni/Ce-Al_2O_3 catalysts

The band at 1490cm^{-1} is associated with all three types of adsorbed pyridine listed above. Pyridine coordinated with Lewis acid sites are characterized by bands in the region 1590–1635cm^{-1} and 1440–1455cm^{-1}, while protonated pyridine on Brønsted centers corresponds to the bands at 1640 and 1540cm^{-1} [97–100].

5.4 Performance of the new Ni/Ce-Al_2O_3 catalysts

5.4.1 Activity in biomass (glucose) gasification

Figure 5.18 depicts the results of Ni(20)/Ce(1)-Al_2O_3 catalyst test in the CREC riser simulator. It is seen that for Case 1, where the catalyst was regenerated by calcination in air, the catalyst activity decreased and produced only about 30 mol. % H_2, which is much lower than amount obtained during the first feed injection (i.e. 44 mol. % with the fresh catalyst). However, in Case 2, where the catalyst was regenerated by calcination and reduction in H_2/Ar, we obtained statistically non-varying amounts of gaseous products for all the subsequent 4 injections (with intermittent regeneration), as with the fresh catalyst.

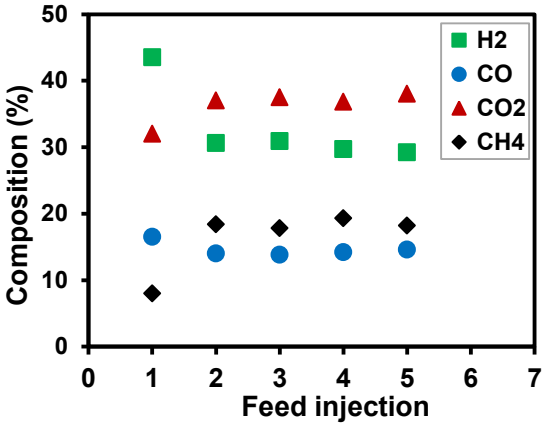

(a) Catalyst was regenerated by calcination in air

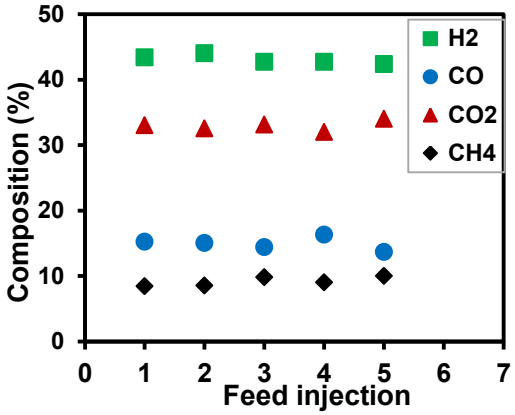

(b) Catalyst was regenerated by calcination in air followed by reduction in H_2/helium

Figure 5.18: Results of catalyst evaluation at 650 °C

Therefore, by subjecting the used catalyst to regeneration in air plus reduction in a hydrogen atmosphere, we have restored its activity and fluidizability for repeated usage

in the riser simulator. It can be inferred also that the air regenerated catalyst was transformed into the oxide form (NiO and $NiAlO_4$). The excellent performance of the catalysts could be elaborated as follows. The mesoporous nature of the support material itself favors the cracking of large intermediate tar compounds [43]. Moreover, the established role of ceria dopant in ensuring the thermal stability of the alumina support [101], makes the catalysts suitable for gasification reaction in a fluidized bed reactor with several cycles of usage and regeneration. Furthermore, the ceria dopant helped in suppressing coke formation during the gasification reactions [See the discussion on coke studies in section 3.4]. The ceria also reduced the nickel-alumina support interaction, as evident from the XRD, TPD, and TPR data. Furthermore, it is seen in Figure 5.18b that the regenerated catalyst performed as effectively as the fresh catalyst, during 4 cycles of re-use. Revisiting Figure 5.18 a and b again, it is observed that the catalysts regeneration procedure has a significant effect on the selectivity for hydrogen and syngas composition. This brings us to the role that the catalyst regeneration method plays and the mechanism by which these new nickel/Ce-Al_2O_3 facilitate the biomass conversion. It is reported that the nickel plays a significant role in C-C bond cleavage [27,58]. Tarry compounds are likely to form a covalent bond via their π-orbital electrons with the 3d electrons of the metallic nickel species [102]. Thus, the resulting nickel-tar intermediate compounds are broken down into more H_2, CO, CO_2, and CH_4. The presence of ceria enhances the nickel dispersion over the surface of the support, thereby enhancing the reaction between steam and adsorbed species on the nickel surface. Table 5.5 compares our findings in terms of hydrogen yield, with the best results reported recently for glucose gasification.

Table 5.5: Results for hydrogen yield from previous studies.

Catalyst	Reactor type/ Material	Reaction conditions	Equilibrium H_2 Yield	Experimental H_2 Yield	Reference
KOH	Continuous tubular reactor	250 bar; 600 °C; 3.6 wt%; 30-120 s	11.85[a]	9.10	Schmieder et al., 2002 [103]
None	Continuous tubular reactor	280 bar; 750 °C; 10.8 wt%; 30 s	11.29[a]	7.00	Lee at al., 2002 [51]
None	Batch autoclave	300 bar; 500 °C; 5 wt %; 1 h; heating rate of 3 K/min	9.31[a]	1.68	Sinag et al., 2004 [104]
Ru/Al_2O_3	Inconel 600	248 bar; 700 °C; 1 wt%, 2 s	11.94	12.00	Byrd et al., 2007 [105]
None	Inconel 600	248 bar; 700 °C; 1 wt%, 4 s	11.94	7.25	Byrd et al., 2007 [105]
None	Continuous tubular reactor	248 bar; 700 °C; 1 wt%, 2 s	11.94	6.50	Byrd et al., 2007 [105]
None	Continuous tubular reactor with updraft configuration made with Haynes®	25 MPa, 767 °C, and 1.8 wt% feed; 60 s	11.89[a]	11.50	Susanti 2012 [37]
20% Ni/5% La_2O_3-γ-Al_2O_3	CREC riser simulator	650 °C, 1 atm; S/B=1.0 g/g; catalyst/biomass =12.5; 20s	9.46[a]	6.24	Jahirul and de Lasa 2014 [94]
$Ni20/CeO_2/Al_2O_3$	Batch reactor	400 °C; 230 bar, 2 wt% feed 1g catalyst	9.34[a]	12.70	Manzour et al. 2012 [27]
H_2O_2 oxidant	Fluidized bed reactor made of 316 stainless steel	650 °C; Pressure, 25MPa; Feedstock flow rate, 10 wt%; 25g/min	11.08[a]	1.61	Jin et al. 2010 [106]
None	Continuous tubular reactor with updraft configuration made with Haynes®	740 °C; 250 MPa; 10wt%; 60 s	11.34[a]	6.49	Susanti 2014 [107]
$Ni_{0.5}/Zr_{0.8}Y_{0.2}O_2$	Batch reactor	500 °C, 23–24 MPa; 10 wt.% feed	6.46[a]	3.96	Jianbing Huang et al. 2017 [108]
$Ni20/CeO_2$-meso-Al_2O_3	CREC riser simulator	650 °C, 1 atm; 15 wt%; 0.2g Catalyst; 20s	11.4[a]	10.17	This work

[a]Calculated under the given experimental conditions [i.e. Considering *T, P and Glucose wt%,* using a thermodynamic model, which is based on direct minimization of total Gibbs' free energy of all the species (See ref. [109])]

The catalyst and reactor types with the respective experimental conditions are given. Our results underscore the efficiency of the both the CREC fluidized bed reactor and the new $Ni(20)/Ce\text{-}Al_2O_3$ catalyst in enhancing hydrogen production from biomass sources.

Precisely, the experimental yield obtained (10.17 mol H_2/mol glucose) is very close to the Thermodynamic limiting value of 11.4 mol H_2/mol glucose.

5.4.2 Catalyst regeneration and re-use for repeated cycles

A general factorial design of experiment (DOE) was carried out to determine the effect of catalyst regeneration mode (A) and feed injection cycle (B) on the composition of gasification products. Table 5.6 shows the experimental run orders with the combination of all the levels of the two factors—A at 2 levels and B at 5 levels.

Table 5.6: Effect of catalyst regeneration mode and feed injection on H_2/CO

StdOrder	RunOrder	Regeneration mode	Feed Injection	H_2 [mol. %]	H_2/CO ratio [-]
23	1	1	5	29.2	2.021
11	2	2	3	42.7	2.97
18	3	1	3	30.8	2.24
16	4	2	1	43.4	2.86
2	5	2	5	42.4	3.09
15	6	1	2	30.7	2.19
20	7	1	2	30.6	2.19
13	8	1	5	29.4	2.00
9	9	2	1	43.3	2.88
19	10	1	4	29.7	2.09
17	11	2	4	42.7	2.62
21	12	2	2	44.0	2.90
24	13	2	4	42.7	2.63
8	14	2	5	42.4	3.11
4	15	1	3	30.9	2.25
3	16	1	1	43.5	2.64
5	17	1	4	29.3	2.08
10	18	2	2	44.0	2.93
14	19	1	1	43.3	2.64
7	20	2	3	42.6	2.98

The responses studied are (1) percentage mole of hydrogen in the gasification products and (2) H_2/CO ratio, which represents the syngas composition. The Box–Cox method, was utilized to select a response transformation, which will ensure the validity of a Gaussian distribution, normality assumption, and randomness of the errors assumptions [110].

Table 5.7 shows the results of ANOVA for the effect of catalyst regeneration mode and biomass feed injection on percentage hydrogen in the gasification product. Since all the P-values for the overall model, linear components (i.e. A and B) as well as interaction (A*B), are all less than $\alpha = 0.05$, it means that the model is satisfactory in predicting the response (hydrogen composition) with respect to the experimental factors.

Table 5.7: ANOVA on H_2 composition

Source	DF	Seq SS	Contribution	Adj SS	MS	F-Value	P-Value
Model	9	2595.09	99.86%	2595.09	235.92	756.67	0
Linear	5	2421.41	93.17%	2421.41	484.28	1553.26	0
A	1	489.17	18.82%	489.17	163.06	522.98	0
B	4	1932.24	74.35%	1932.24	966.12	3098.69	0
2-Way interactions	4	173.68	6.68%	173.68	28.95	92.84	0
A*B	4	173.68	6.68%	173.68	28.95	92.84	0
Error	10	3.74	0.14%	3.74	0.31		
Total	19	2598.83	100.00%				

Therefore, both catalyst regeneration mode (Factor A: at levels 1 or 2) and the injection number (Factor B: 1^{st} to 5^{th}), are significant in determining the percentage hydrogen composition in the gasification products. The value of adjusted $R^2 = 0.998$ indicates that the fitting is excellent.

The results of the analysis of variance in the syngas ratio (H_2/CO) is shown in Table 5.8.

Table 5.8: ANOVA on syngas composition.

Source	DF	Adj SS	Adj MS	F-Value	P-Value
Model	9	0.463	0.051	2496.90	0
Linear	5	0.400	0.080	3883.62	0
A	1	0.345	0.345	16761.05	0
B	4	0.055	0.014	664.26	0
2-Way interactions	4	0.063	0.016	763.51	0
A*B	4	0.063	0.016	763.51	0
Error	10	0.000	0.000		
Total	19	0.463			

Again since all the P-values for the overall model, linear (A and B) and interaction (A*B) components are all less than $\alpha = 0.05$, it means that the model is satisfactory in predicting the response (H_2/CO ratio) with respect to the experimental factors, which are catalyst regeneration mode and the injection number (1^{st} to 5^{th}). The value of adjusted $R^2 = 0.998$ indicates that the fitting is excellent. From these statistical analyses, we infer that the activity and recyclability of the catalyst during 5 cycles of usage and regeneration are dependent upon the mode of catalyst regeneration. This further confirms that the drop in hydrogen selectivity after the first feed injection as observed in Figure 5.18, is indeed significant and did not occur by chance.

5.5 Coke analysis

The spent catalyst further analyzed to investigate the nature of the carbon deposited on during the biomass gasification in the CREC riser reactor. Because of the susceptibility of a nickel catalyst to coke deposition during gasification reactions [111], thermal gravimetric analysis (TGA) was conducted on the spent catalysts to ascertain the extent of carbon deposited during catalyst evaluation in the riser simulator. Figure 5.19 shows the thermograms of the spent catalysts, obtained from using a TGA in the presence of air stream.

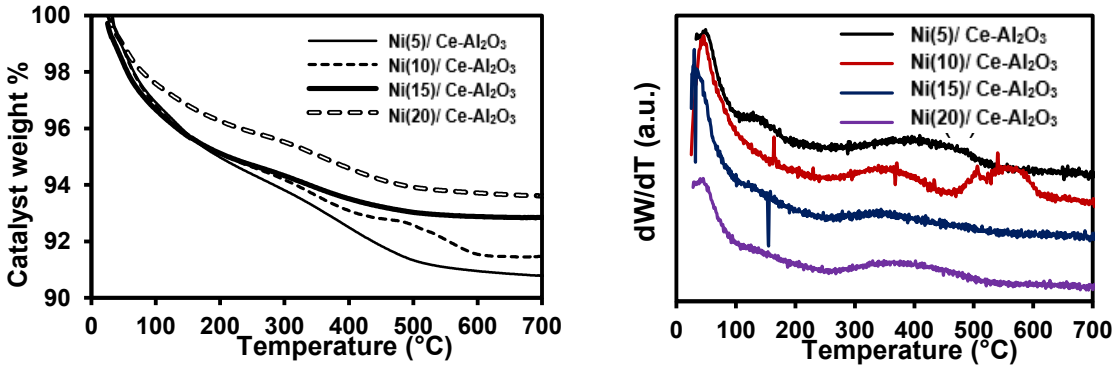

Figure 5.19: Thermograms of the spent catalyst after testing in the riser simulator

The results indicate a rapid weight loss up to 168 °C, followed by a gradual weight loss, up to 320 °C. The first transition is related to water desorption and partly due to oxidation of volatile compounds (e.g. low molecular weight organic acids) adsorbed on the catalyst during biomass gasification [48]. Beyond, 168 °C, the moisture trapped within the pore network is desorbed, while the oxidation of the volatile deposits continues. Amorphous coke oxidization ensues from 320°C [112,113] and continues

until 500 °C. Beyond 500 °C, the refractory coke begins to oxidize [114], as evidenced by the gradual decrease in the sample weight, until a constant weight was attained around 600 °C. The transformation occurring beyond 500 °C is attributed to the decomposition/oxidation of stable coke compounds, which are responsible for catalyst deactivation. TGA of the spent catalysts indicated that indeed ceria addition has tackled the tendency of nickel carbide formation and hence mitigated catalyst coking. Interestingly, the extent of coke formation was lowered as the nickel loading was increased from 5 to 20 wt%. This further confirmed that the presence of ceria dopant inhibits the nickel-carbide formation [42,102], resulting in higher carbon gasification efficien**cy.** Figure 6.4 indicates that catalyst Ni(10)/Ce-Al_2O_3 is exceptionally more prone to this refractory coke formation. This may be connected with the catalyst electronic environment at the 10 wt. % loading. Therefore, this particular loading (i.e. 10 wt. % Ni) may be far from the optimal catalyst loading required to gasify 15 wt. % glucose at the given experimental conditions. Future work in this area should be dedicated to optimizing the catalyst loading and experimental conditions.

Furthermore, FTIR spectra of the spent catalysts were recorded to observe the fate of the active sites after a gasification cycle (See Figure 5.20). Comparing these spectra with those of the fresh catalyst shown in Figure 5.17, we see that the band at 1430 cm^{-1} disappeared after biomass gasification. This means that some of the Ni/Ce-Al_2O_3 catalyst active sites might have been blocked by carbon deposition [115], and hence the need for regeneration. Also, this confirms that the Lewis acidic centers are responsible for the conversion of the intermediates compounds—arenes, acids, aldehydes and ketones to permanent gases (i.e. H_2, CO, CO_2 and CH_4) [41].

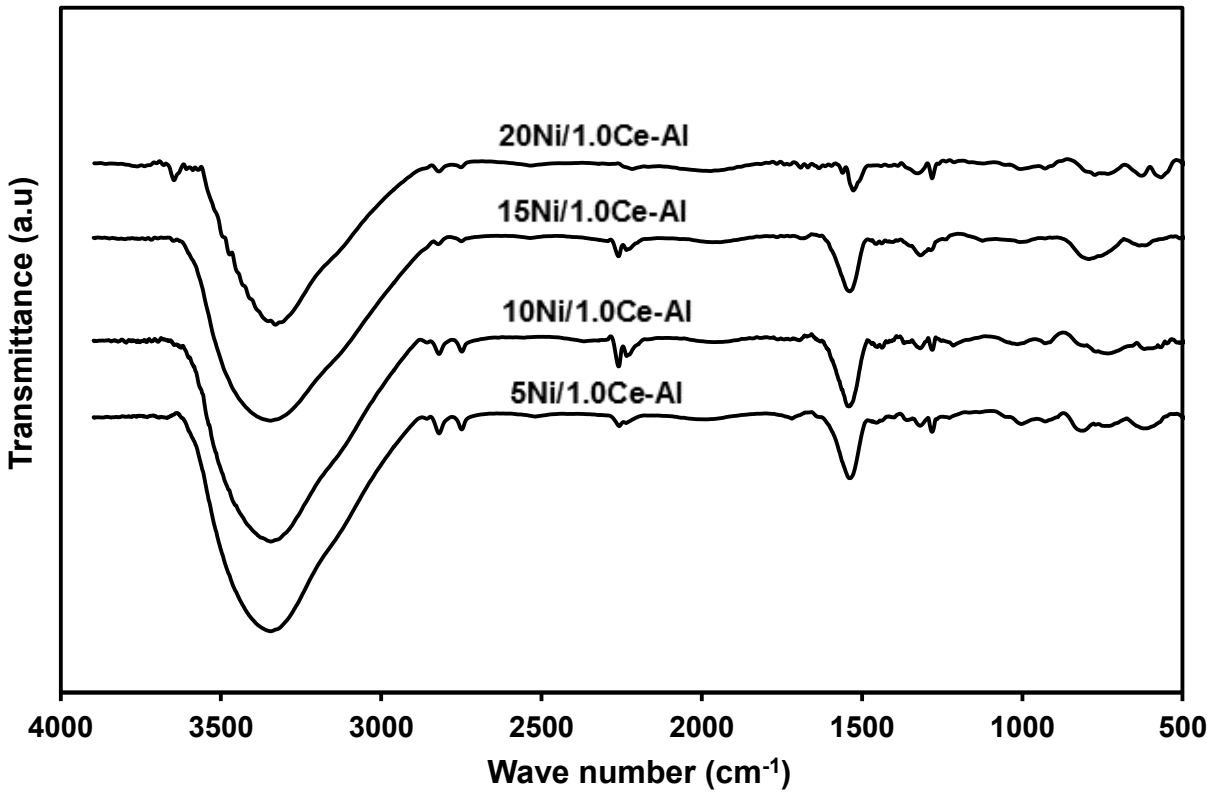

Figure 5.20: Infrared spectra of the spent Ni/Ce-Al_2O_3 catalysts

It is observed that the band centered around 3330 cm^{-1}, which are assigned to the bending, combination and stretching mode of adsorbed water molecules within the pore of the catalysts are very broad, as compared with those for the fresh catalysts shown in Figure 5.17. More, specifically, the catalysts loaded with 5–15 wt. % Ni have stronger band than the catalyst containing 20 wt. % nickel at this wavenumber. This could be ascribed to the gradual increase in the agglomeration tendency as the nickel loading is increased to 20 wt. %. Therefore these three (i.e. Ni(5)/Ce-Al_2O_3, Ni(10)/Ce-Al_2O_3, Ni(15)/Ce-Al_2O_3) catalyst will be similar in terms of adsorption capacity for the reactants (biomass + water), and could probably have similar performance for water gas shift reaction. The band around 1530 cm^{-1} is related to hydroxyl groups.

To further confirm that the catalyst was fully regenerated, we examined one of the catalysts (i.e. Ni(20)/Ce-Al_2O_3) for Raman spectroscopy. The purpose is to probe the regenerated catalyst of any remnant carbon deposit. Figure 5.21 illustrates the Raman spectra of the catalyst sample after regeneration in air followed by reduction with a hydrogen stream. Prior to regeneration, the spent catalyst is expected to show Raman peaks at ~1385 and ~1585 cm^{-1} for deposited coke [91].

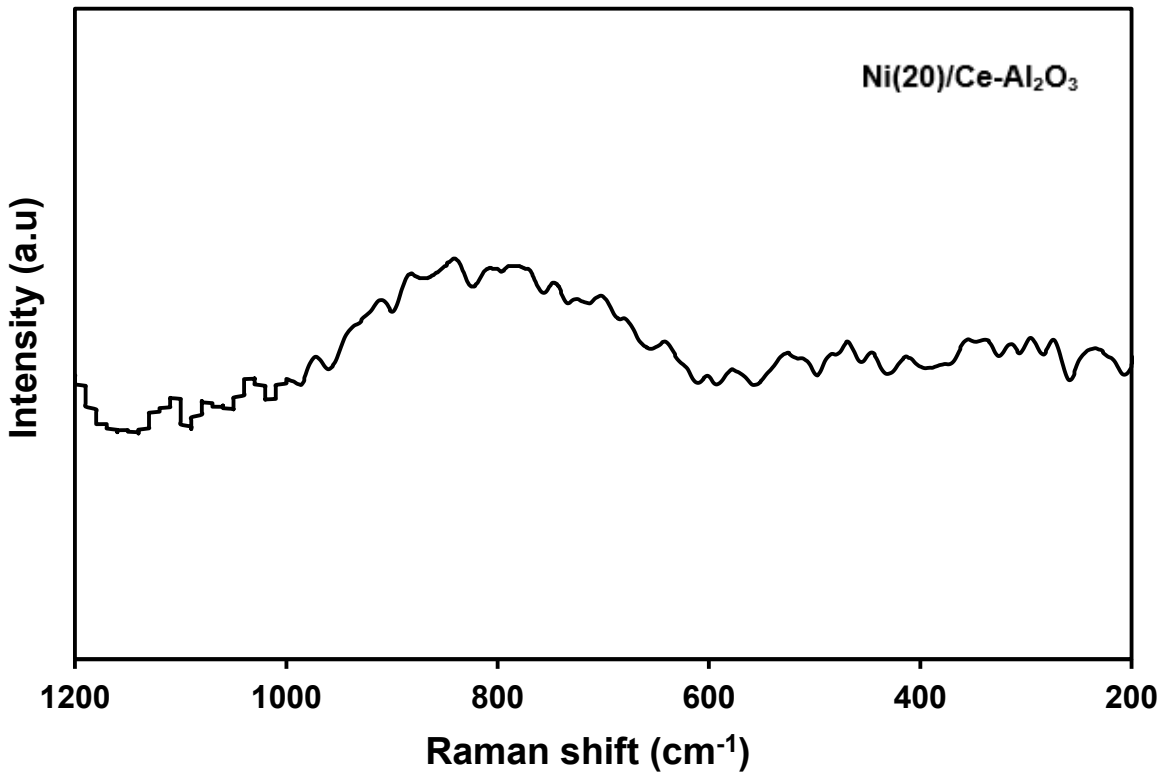

Figure 5.21: Raman spectra of the regenerated catalyst.

The results indicates the absence of any remnant of deposited carbon in the regenerated catalyst after the 5th injection. Therefore, it is expected that after regeneration, the catalyst will perform as much as the newly prepared catalyst for at least 5 feed injections.

5.6 Mechanism of glucose gasification over Ni/Ce-Al_2O_3

Starting from the synthesis methodology and going through the whole picture of the results for catalysts characterization and coke studies, we propose the following pictorial overview (See Figure 5.22) for mechanism of glucose conversion to syngas over the newly prepared Ni/Ce-Al_2O_3 Catalysts in the riser simulator.

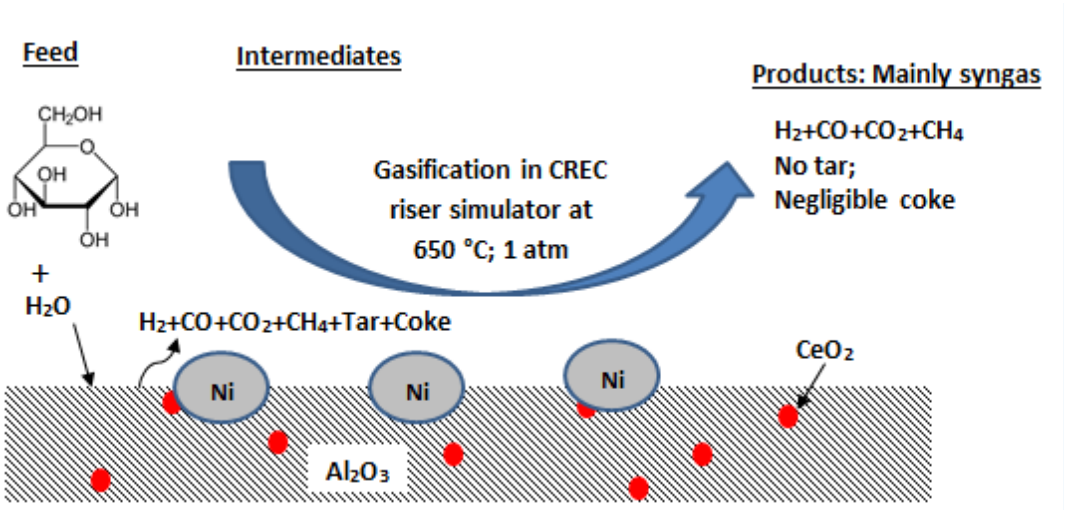

Figure 5.22: Mechanism of glucose conversion to syngas over Ni/Ce-Al_2O_3.

The feed (glucose solution) vaporizes instantly into permanent gases (H_2, CO, CO_2, and CH_4), coke and tar (e.g. phenol, furfural, alcohols, arenes etc.) [52]. The acidic ceria-

doped Al_2O_3 support would crack the higher organic compounds to lower hydrocarbons and water via a dehydrogenation reaction step [52,116]. The reaction temperature (650 °C) is also thermodynamically suitable for the conversion of tar to syngas [7]. The supported nickel ($Ni^{(0)}$) at the catalyst surface would cleave the intermediate gasification compounds into permanent gases and other tarry compounds. The appropriate agitation speed (i.e. 4000 rpm) will maximize the contact among the gases and, they would engage in different reactions simultaneously (See Table 5.9), to selectively produce hydrogen and reduce coke and methane to the minimal level depending on the catalyst loading and reaction time.

Table 5.9: Reactions network engaged by the permanent gases (ref. [94]).

Water gas shift reaction	$CO + H_2O \leftrightarrow H_2 + CO_2$	ΔH^0 = -41.2 kJ/mol	(5-13)
Steam reforming of methane	$CH_4 + H_2O \leftrightarrow CO + 3H_2$	ΔH^0 = 206 kJ/mol	(5-14)
Dry reforming of methane	$CH_4 + CO_2 \leftrightarrow 2CO + 2H_2$	ΔH^0 = 247 kJ/mol	(5-15)
Coke gasification	$C + H_2O \leftrightarrow CO + H_2$	ΔH^0 = 131.3 kJ/mol	(5-16)
Boudouard reaction	$2CO \leftrightarrow C + CO_2$	ΔH^0 = -172.5 kJ/mol	(5-17)
Hydrogeneting reaction	$C + 2H_2 \leftrightarrow CH_4$	ΔH^0 = -74.5 kJ/mol	(5-18)

In the case of the oxide form of the catalyst, the results for catalyst evaluation together with the literature studies suggest that the catalyst would first undergo reduction to metallic nickel ($Ni^{(0)}$), by the reducing gases (i.e. H_2 and CO). This will eventually

decrease the relative amount of hydrogen or syngas in the reaction product. Therefore, we conclude that the varying modes of catalyst regeneration have given an insight into the mechanism by nickel catalyzes glucose gasification.

From the foregoing results and discussion, we can conclude this section as follows. It is known that one of the main challenges with the use of Ni/Al_2O_3 for biomass gasification is coke deposition, which can poison the catalyst or render it inactive [18]. Hence, the typical fluidized bed reactor makes provision for regeneration in an air stream. The CREC riser simulator mimics the industrial fluidized bed reactor, and in fact has a provision of air inlet for catalyst regeneration. On the other hand, biomass gasification using nickel based catalyst requires that the catalyst should be in its metallic form [40,117]. Thus, once the catalyst is used, it should be subjected to regeneration by oxidation (to burn off the coke) and reduction (to reduce the NiO to metallic Ni). Therefore, we applied $10\%H_2$/helium stream to achieve reduction after air oxidation. Results obtained in the CREC riser shows that the activity is fully regained after this oxidation-reduction sequence (See Figure 5.18 b). In the case where the regeneration stops at the air oxidation (as provided is the conventional riser simulator setting), we observed a decline in the catalyst activity (See Figure 5.18 a). This is partly due to the fact that nickel is in an oxide form, and therefore consumed some of the gasification products (especially $CO+H_2$), which were formed during pyrolysis, to reduce it to the $Ni^{(0)}$ form [102]. This is corroborated from our knowledge from temperature reduction experiments, that NiO phases are easily reducible by H_2 or CO [40]. The thermograms of the spent catalysts shown in Figure 6.4, indicate that the extent of coking was generally low, with $Ni(5)/Al_2O_3$ having the

maximum of 0.092 g (Coke+Moisture)/g-catalyst. An increase in nickel loading from 5 to 20 wt. % further mitigated the extent of coking during the gasification process. This is ascribed to the higher carbon conversion with increase in nickel loading. So far, we have seen how 1.0 wt. % ceria dopant could alter the alumina support properties and eventually influence the catalytic and thermal properties of the Ni/Ce-Al_2O_3 catalysts. In subsequent studies we shall look at the interplay of support acidity/basicity as well as the alumina support type on the catalytic activity of nickel based catalysts in biomass gasification.

Now, we will summarize this Chapter as follows. The combined template free method for Al_2O_3 synthesis with the subsequent metal impregnation via successive incipient wetness impregnation is a promising method for developing highly active, moderately acidic and well dispersed Ni/Al_2O_3 based catalysts for biomass gasification. Ni(20)/Ce-meso-Al_2O_3 was the best in terms of hydrogen production, and showed the lowest degree of coking. It shows an outstanding performance relative to other catalysts considered in this work, and those reported recently in the open literature suggest that there is a synergy between the ceria promoter and our methodology for developing Ni/Ce-doped-Al_2O_3 catalysts at 20 wt% nickel loading.

CHAPTER 6

KINETIC MODELING

6.1 Background

From the results of catalyst evaluation, it is obvious that the experimental product compositions are time dependent. Therefore a kinetic model is desired to describe the process adequately. It is sufficient to develop a phenomenological kinetic model which is simple but adequate enough to represent glucose gasification over the new Ni/Ce-meso-Al_2O_3 catalyst. The model to be developed should be able to capture the main processes and the detailed mechanism of the individual elementary reaction steps occurring during the entire gasification process.

Therefore this Chapter is dedicated to the development of a reaction mechanism to model the kinetics of biomass gasification, catalyzed by the newly prepared Ni/Ce-meso-Al_2O_3 in CREC riser reactor. This Chapter is reproduced mainly from a manuscript prepared for a journal publication titled "Kinetics of Glucose Gasification over Ni/Ce-meso-Al_2O_3 in a Fluidized Bed".

6.2 Synopsis

The catalytic conversion of biomass to fuels and chemicals is a promising approach for clean energy production. An appropriate catalyst system is required to curtail the high energy requirement and maximize the selectively for the desired product during biomass gasification. Hence a number of ways of improving the catalytic activity, stability and applicability of nickel-based catalysts for low-temperature gasification were investigated and reported in the literature [5,45,122,123]. The role of Ni/Al_2O_3 catalysts in C-C and C-O bond cleavage during biomass and tar conversion is reported in the literature [27,58]. It is worth mentioning that Ni/Al_2O_3 is cheap, relatively stable with favorable metal support interactions [124]. The acidic alumina support provides a high surface area, good thermal stability, high adsorption capacity and excellent mechanical strength, for the active nickel species, with minimal agglomeration, sintering or crystal growth especially when the nickel loading is not more than 20 wt% [25,101,125]. It was reported that the incorporation of an appropriate promoter could enhance catalytic properties and give rise to new set of kinetic parameters for the same reactive system [101,114,124]. Sang et al. [114] reported that ceria in $Ni/CeO_2/Al_2O_3$ catalyst assisted in improving hydrogen yield, attenuating coke deposition during autothermal reforming of iso-octane. Furthermore, the reactor type is very vital in ensuring that a reasonable biomass or tar conversion is achieved. A number of investigations on glucose gasification indicate that long reaction times are necessary for achieving reasonable amounts of hydrogen or syngas per unit mole of glucose in batch reactors [104,124]. The riser simulator favors high yield of gaseous products at atmospheric pressure with concentrated or diluted biomass feedstock, and within short time intervals. This offers an

overall low operational cost, considering the high energy implication of biomass drying in conventional gasifiers [126,127]. Moreover, the fluidized bed configuration makes a provision for easy catalyst regeneration and reuse over several cycles. This is, in fact, a significant advantage over the batch and fixed bed reactors. The available reports on the kinetic modeling of biomass gasification are quite a few and mostly based on lump-species approach [128]. Matsumura and coworkers [129] attempted to model glucose gasification by monitoring its conversion with time. The application of this approach is limited by the fact that glucose decomposes instantly at 460 °C [130]. This implies that monitoring glucose concentration with time at regular gasification conditions may be grossly inaccurate. Hejazi et al. [131] developed a two-step kinetic model consisting of (1) primary pyrolysis involving 3 parallel first order reactions producing gaseous products, tar and char, and (2) Secondary pyrolysis represented by a first order homogeneous thermal cracking of tar. The yields of pyrolysis products were lumped together, whereas the proportions of major compounds in the pyrolysis gas were predicted on the basis of CHO elemental balances. This is indeed a good attempt at modeling biomass gasification. However, the intrinsic parameters used in their work were obtained from the literature. Weiss-Hortala et al. [132] reported that the rate of hydrogen production is kinetically limited, showing a slight decrease with increase in glucose concentration (from 0.25 – 2 wt%) at 500 °C, 25 MPa and 1.385 kg/h. Bernard et al. [133] used the immediate products of glucose decomposition to elucidate the reaction kinetics of glucose decomposition at low temperature (300 – 400 °C), high pressure (25 – 400 MPa) and short reaction times (i.e. 0.02 – 2 seconds). They encountered a number of tarry compounds which are undesirable products of biomass

gasification. Furthermore, some researchers modeled the kinetics of glucose gasification on the basis of the dominant reactions as deduced from the composition of gasification products. Weiss-Hortala et al. [132] developed a kinetic model in which glucose is mainly reformed to water and CO_2, which will subsequently undergo water gas shift (WGS) and methanation reactions to yield the final product composition. Hejazi et al. [131] adopted an additive kinetic model based on boudouard reaction (E_a = 215 kJ/mol), coke gasification (E_a = 237 kJ/mol), methanation (E_a = 94.8 kJ/mol), steam reforming of methane (E_a = 12.5 kJ/mol), and WGS (E_a = 15.1 kJ/mol) including the corresponding n^{th} order rate equations as obtained from the literature.

The present work is aimed at investigating the gasification kinetics of glucose as a biomass model compound over a new Ni/Ce-doped-mesoporous-Al_2O_3 catalyst. The excellent properties of the new Ce-doped-meso-Al_2O_3 support are described in our previous work [101]. The new Ni/Ce-meso-Al_2O_3 catalysts were prepared by loading 5 – 20 wt. % nickel on the Ce-meso-Al_2O_3 support via successive incipient wetness impregnation method. The physicochemical properties of Ni/Ce-meso-γ-Al_2O_3 catalysts were probed using XRD, NH_3 TPD, and N_2 physisorption. The spent catalyst was subjected to thermogravimetric analysis to ascertain the extent of carbon deposition. The phenomenological kinetic model considers catalyst properties, time progression of the gasification product composition, as well as their participation in the reactions described above. We envision that this contribution will give a new outlook on the kinetic modeling of catalytic biomass gasification, and be a good contribution to the literature.

6.3 Kinetic model development

It is informative to have a simple kinetic model that is sufficient to represent a reactive system. However, the kinetic model should be able to account for the time progression of the reacting components as well as to capture the detailed mechanisms of the entire reactive system. We have therefore developed a Langmuir-Hinshelwood type mechanism to account for the adsorptive, reactive and desorption steps during reactant activation, surface reaction and subsequent product desorption from the reaction sites

6.3.1 Overall reaction

During biomass gasification, the biomass macromolecule is first converted into permanent gasses (i.e. H_2, CO, CO_2, CH_4 and H_2O), coke and tars (phenolics and aromatic compounds etc.). Hence the overall reaction is represented as follows.[5,94,134,135]

$$C_xH_yO_z + nH_2O \xrightarrow{heat} H_2 + CO + CO_2 + H_2O + CH_4 + C + Tars \qquad 6\text{-}1$$

The relative amounts of the products shown in the equation above are dependent upon the gasifier operating conditions as well as the activity and selectivity of the catalyst used. The gaseous products will re-combine in the following set of complex and competing reactions, to give the final product distribution [94,135–140].

The Langmuir-Hinshelwood type of mechanism has been satisfactorily applied to model the rate of catalytic biomass gasification [137,138,141–143] However, different sort of assumptions and approximation were incorporated, which may hamper with the phenomenological kinetics of biomass gasification. This work intends to incorporate all possible steps taking place during glucose gasification in a fluidized bed reactor, on the

basis of the selectivity of the new Ni(x)/Ce-meso-Al_2O_3 catalytic system for the various gasification products.

The detailed kinetic model was developed on the basis of the following assumptions/steps

(i) The biomass surrogate (i.e. glucose solution) is converted instantly (i.e. at $t << 5$ s) to CO, CO_2, H_2, CH_4 with negligible tar and coke. Where $t = 5$ s, is the smallest time at which measurements were taken during the kinetic experiments.

(ii) The species CO, CO_2, H_2, CH_4 and H_2O get adsorbed onto the catalyst surface, undergo a number of reactions and desorb back to the product bulk stream

(iii) The dominant reactions are WGS, DRM and SRM reactions.

Assumption number (i) is true considering the constancy of the reactor pressure (about 57 psi) during the reaction irrespective of the reaction time from $t = 5 - 25$ s. Moreover, the products area mainly CO, CO_2, H_2, CH_4 during the time interval 5 – 25 sec. Assumption number (iii) is valid considering the high value of the activation energies reported for other possible reactions like coke gasification, boudouard and methanation reactions as compared with SRM, WGS, and RDRM.[131] Assumption number (ii) together with (i) and (iii) were used to develop the phenomenological kinetic model in the following subsections.

6.3.2 Steam reforming of methane

The overall reaction for steam reforming of methane is given by:

$$CH_4 + H_2O \rightarrow CO + 3H_2 \qquad 6\text{-}2$$

The detailed mechanism involves the following adsorption/reaction/desorption steps:

1. Adsorption of methane onto the nickel active site

$$CH_4 + S \underset{k_2}{\overset{k_1}{\rightleftarrows}} CH_4 - S \qquad 6\text{-}3$$

2. Adsorption of steam onto the catalysts active site

$$H_2O + S \underset{k_4}{\overset{k_3}{\rightleftarrows}} H_2O - S \qquad 6\text{-}4$$

3. Surface reaction on the catalysts active site

$$CH_4 - S + H_2O - S + 2S \underset{k_6}{\overset{k_5}{\rightleftarrows}} CO - S + 3H_2 - S \qquad 6\text{-}5$$

4. Desorption of CO from the catalyst surface

$$CO - S \underset{k_8}{\overset{k_7}{\rightleftarrows}} CO + S \qquad 6\text{-}6$$

5. Desorption of H_2 from the catalyst surface

$$H_2 - S \underset{k_{10}}{\overset{k_9}{\rightleftarrows}} H_2 + S \qquad 6\text{-}7$$

The overall site balance is

$$C_T = C_V + C_{H_2-S} + C_{H_2O-S} + C_{CO-S} + C_{CO_2-S} + C_{CH_4-S} \qquad 6\text{-}8$$

Applying the pseudo steady state assumption for all the adsorption steps, we obtained:

$$r_{SRM} = \frac{k_{SRM} P_{CH_4} P_{H_2O}}{\left(1 + K_{H_2} P_{H_2} + K_{H_2O} P_{H_2O} + K_{CO} P_{CO} + K_{CO_2} P_{CO_2} + K_{CH_4} P_{CH_4}\right)} \left(1 - \frac{P_{CO} P_{H_2}^3}{K_{SRM} P_{CH_4} P_{H_2O}}\right) \qquad 6\text{-}9$$

where $K_{SRM} = \frac{k_6 K_{CO} K^3_{H_2}}{k_5 K_{CH_4} K_{H_2O}}$, is the equilibrium rate constant and $k_{SRM} = C_T^4 k_5 K_{CH_4} K_{H_2O}$ is the lumped reaction rate constant for SRM.

6.3.3 Water gas shift reaction

The overall water gas shift reaction is given by:

$$CO + H_2O \rightarrow CO_2 + H_2 \qquad 6\text{-}10$$

The mechanism involves the following adsorption/reaction/desorption steps:

1. Adsorption of CO onto the nickel active site

$$CO + S \underset{k_2}{\overset{k_1}{\rightleftarrows}} CO - S \qquad 6\text{-}11$$

2. Adsorption of steam onto the catalysts active site

$$H_2O + S \underset{k_4}{\overset{k_3}{\rightleftarrows}} H_2O - S \qquad 6\text{-}12$$

3. Surface reaction (1 & 2) on the catalysts active site

$$CO - S + H_2O - S + 2S \underset{k_6}{\overset{k_5}{\rightleftarrows}} CO_2 - S + H_2 - S \qquad 6\text{-}13$$

4. Desorption of CO_2 from the catalyst surface

$$CO_2 - S \underset{k_8}{\overset{k_7}{\rightleftarrows}} CO_2 + S \qquad 6\text{-}14$$

5. Desorption of H_2 from the catalyst surface

$$H_2 - S \underset{k_{10}}{\overset{k_9}{\rightleftarrows}} H_2 + S \qquad 6\text{-}15$$

Applying the pseudo steady state assumption for all the adsorption steps, we obtained;

$$r_{WGS} = \frac{k_{WGS} P_{CO} P_{H_2O}}{\left(1 + K_{H_2} P_{H_2} + K_{H_2O} P_{H_2O} + K_{CO} P_{CO} + K_{CO_2} P_{CO_2} + K_{CH_4} P_{CH_4}\right)^2} \left(1 - \frac{P_{CO_2} P_{H_2}}{K_{WGS} P_{CO} P_{H_2O}}\right) \qquad 6\text{-}16$$

where $K_{WGS} = \frac{k_6 K_{CO_2} K_{H_2}}{k_5 K_{CO} K_{H_2O}}$ is the water gas shift reaction equilibrium rate constant, and $k_{SRM} = C_T^2 k_5 K_{CO} K_{H_2O}$ is the lumped WGS reaction rate constant.

6.3.4 Reverse dry reforming of methane

The overall reverse dry reforming of methane is given by:

$$2CO + 2H_2 \rightarrow CH_4 + CO_2 \qquad 6\text{-}17$$

The mechanism involves the following adsorption/reaction/desorption steps:

1. Adsorption of CO onto the nickel active site

$$CO + S \underset{k_2}{\overset{k_1}{\rightleftarrows}} CO - S \qquad 6\text{-}18$$

2. Adsorption of hydrogen onto the catalysts active site

$$H_2 + S \underset{k_4}{\overset{k_3}{\rightleftarrows}} H_2 - S \qquad 6\text{-}19$$

3. Surface reaction (1 & 2) on the catalysts active site

$$2CO - S + 2H_2 - S + 2S \underset{k_6}{\overset{k_5}{\rightleftarrows}} CO_2 - S + CH_4 - S + 2S \qquad 6\text{-}20$$

4. Desorption of CO_2 from the catalyst surface

$$CO_2 - S \underset{k_8}{\overset{k_7}{\rightleftarrows}} CO_2 + S \qquad 6\text{-}21$$

5. Desorption of CH_4 from the catalyst surface

$$CH_4 - S \underset{k_{10}}{\overset{k_9}{\rightleftarrows}} CH_4 + S \qquad 6\text{-}22$$

Applying the pseudo steady state assumption for all the adsorption steps, we obtained;

$$r_{RDRM} = \frac{k_{RDRM} P_{CO}^2 P_{H_2}^2}{\left(1 + K_{H_2} P_{H_2} + K_{H_2O} P_{H_2O} + K_{CO} P_{CO} + K_{CO_2} P_{CO_2} + K_{CH_4} P_{CH_4}\right)^4} \left(1 - \frac{P_{CO_2} P_{CH_4}}{K_{RDRM} P_{CO}^2 P_{H_2}^2}\right) \qquad 6\text{-}23$$

where $K_{RDRM} = \frac{k_5 K_{CO}^2 K_{H_2}^2}{k_6 K_{CO_2} K_{CH_4}}$ is the RDRM reaction equilibrium rate constant, and $k_{SRM} = C_T^4 k_5 K_{CO}^2 K_{H_2}^2$ is the lumped RDRM reaction rate constant.

6.3.5 Additive rate equations for the component species

The rate equation for each component in the CREC fluidized bed reactor is given by:

$$r_i = \frac{V}{W}\frac{d}{dt}\left(\frac{p_i}{RT}\right) \qquad 6\text{-}24$$

The additive rate expression for each of the five reacting species could be written in terms of the major reactions as follows:

$$r_i = \sum_j \nu_{i,j} r_j \qquad 6\text{-}25$$

where $\nu_{i,j}$ is the stoichiometric coefficient of component i in the j^{th}reaction.

Combining equations 6-24 and 6-25, we have:

$$\frac{dp_i}{dt} = \frac{RTW}{V}\left(\sum_j \nu_{i,j} r_j\right) \qquad 6\text{-}26$$

Where $\nu_{i,j}$ are given in Table 6.1, as deduced from equations 6-2, 6-10 and 6-17

Table 6.1: Stoichiometric coefficients for the reacting components.

Component	H_2	CO	CO_2	CH_4	H_2O
WGS	1	-1	1	0	-1
SRM	3	1	0	-1	-1
RDRM	-2	-2	1	1	0

The reaction rate constants were represented by the Arrhenius equation

$$k_j = k_j^0 \exp\left[-\frac{E_A}{RT}\left(\frac{1}{T}-\frac{1}{T_0}\right)\right] \qquad 6\text{-}27$$

Similarly, for the adsorption rate constants, we have

$$K_i = K_i^0 \exp\left[-\frac{\Delta H_i^{ads}}{RT}\left(\frac{1}{T}-\frac{1}{T_0}\right)\right] \qquad 6\text{-}28$$

The resulting kinetic model was then regressed against the experimental (partial pressure-temperature/time) data generated during the reaction in the riser.

6.4 Properties of the catalysts

6.4.1 Surface properties of the new Ni(x)/Ce-Al_2O_3 catalysts

Table 6.2 shows the surface areas, average pore sizes and pore volumes of the fresh Ni(x)/Ce-Al_2O_3 catalysts and that of the Ce-Al_2O_3 support. In general, all the catalysts exhibit high specific surface areas greater than 104 m^2/g. Also, the table indicates that the pore sizes and pore volumes were not significantly affected by the successive nickel loading up to 20 wt%. These results imply that there is a high dispersion of nickel on the new Ce-Al_2O_3 support at nickel loading up to 20 wt%.

Table 6.2: Surface properties of the newly synthesized catalysts.

Catalyst	BET surface area (m^2/g-sample)	Pore volume (mL/g)	Average pore size (Å)
Ce-Al_2O_3	152	0.43	97
Ni(5)/Ce-Al_2O_3	139	0.37	95
Ni(10)/Ce-Al_2O_3	128	0.32	93
Ni(15)/Ce-Al_2O_3	109	0.29	96
Ni(20)/Ce-Al_2O_3	104	0.26	93

6.4.2 Crystalline properties

The XRD patterns of the freshly prepared Ni(x)/Ce-Al_2O_3 catalysts are shown in Figure 6.1. The peaks at 37.5, 46.2, and 67° are assigned to γ-alumina (ref. JCPDS: 01-074-2206). Ceria peaks were not observed due to its low amount (1.0 wt%) and the high extent of dispersion. The intensity of the peaks at 37.5, 46, and 67° increased greatly after nickel impregnation. This is due to crystalline nickel interacting with Al_2O_3 or $CeAlO_3$ in a different fashion. Furthermore, the formation of $NiAl_2O_4$ spinel may not be ruled out considering the fact that NiO/$NiAl_2O_4$ are not easily distinguishable[144]. The peaks at $2\theta = 61°$ are due to metallic nickel species[123]. In particular, Ni(20)/Ce-Al_2O_3 shows relatively shaper peaks than the rest of the catalysts. This may be connected with the fact the sample was further annealed after the impregnation of each additional 5 wt% nickel according to the successive incipient impregnation protocol. Thus, we conclude that the incipient wetness technique is effective in ensuring a high dispersion of nickel as evident by the absence of sharp XRD peaks related to nickel species.

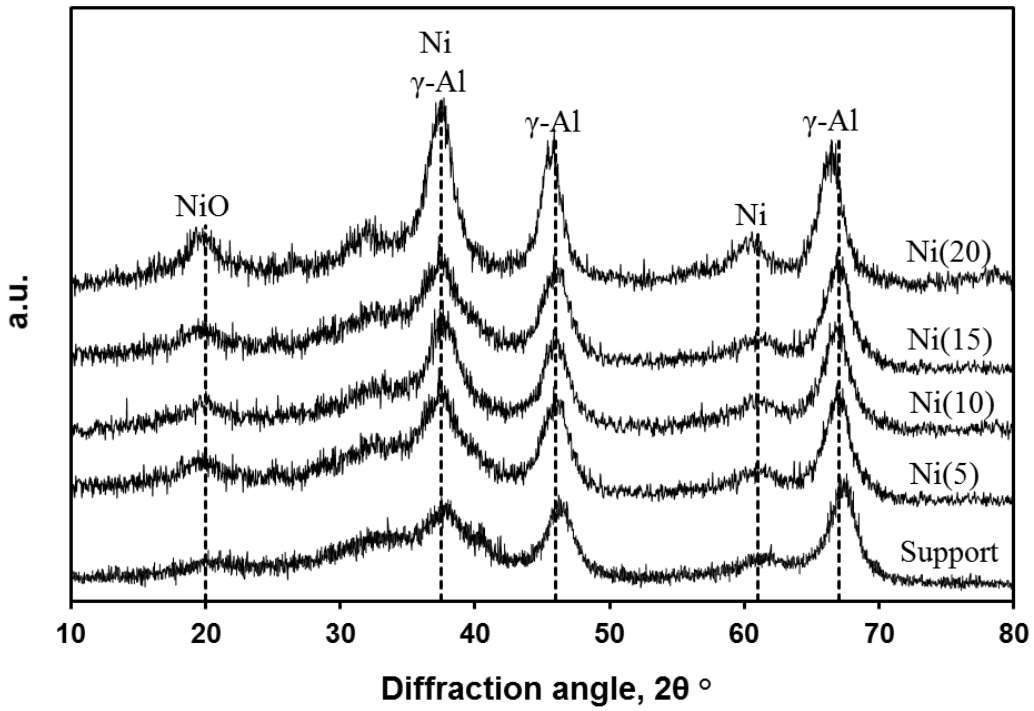

Figure 6.1: XRD patterns of the new Ni(x)/Ce-Al_2O_3 catalysts

6.4.3 Acidity of the catalysts

The total acidity of the Ni(x)/Ce-Al_2O_3 catalysts was quantified using NH_3 TPD. Figure 5.15 (in Chapter 5) illustrates the TPD profiles of the fresh Ni(x)/Ce-Al_2O_3 catalysts. It is observed that NH_3 desorption from the weak acid sites was completed below 300 °C. The volume of these low-temperature peaks declined with increase in the nickel loading (from 5 to 10 wt%). This is due to a partial blockage of some of alumina acidic sites by the nickel species. From 10 wt% nickel loading to 20 wt% and within the range $120 < T < 350$ °C, the profiles progressed in a similar fashion.

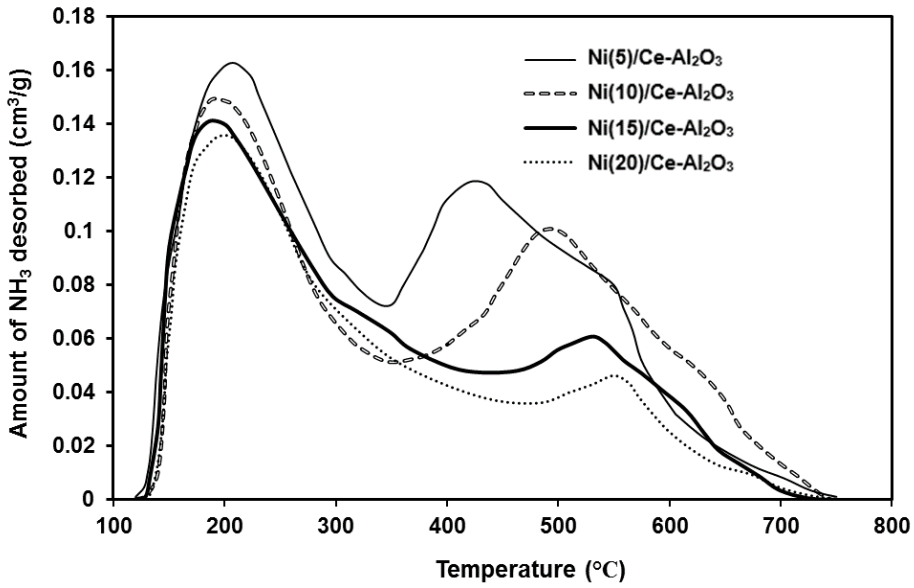

Figure 6.2: NH_3 TPD of freshly prepared Ni(x)/Ce-Al_2O_3 catalysts

Furthermore, as the nickel loading was increased from 5 to 20wt%, the centers of the high-temperature desorption peaks shifted forward. The extent of this shifting decreased gradually as we move from 5 to 20 wt%, implying a possible convergence as the nickel loading was successively increased above 20 wt%. This points to a possible optimum for the nickel impregnation on our novel Ce-Al_2O_3.

Table 5.2 presents the total acidity for each of the four catalysts. At 5.0 wt% nickel loading, the catalyst exhibits a relatively higher acidity (0.321 mmol NH_3/g). As the nickel loading was increased, the total acidity gradually decreased. This could be ascribed to coordination of more nickel species with the Lewis acidic centers of alumina, which are electron deficient [61,94]. In Figure 5.15, this phenomenon is translated as the decrease in the relative amounts of the high-temperature desorption peak volumes.

Table 6.3: Acidity of the newly synthesized catalysts.

Catalyst	Total acidity (mmol NH_3/g-sample)
Ni(5)/Ce-Al_2O_3	0.321
Ni(10)/Ce-Al_2O_3	0.279
Ni(15)/Ce-Al_2O_3	0.234
Ni(20)/Ce-Al_2O_3	0.204

The catalyst acidity has a significant role in the performance of a biomass gasification catalyst. Hence, it will be used as one of the criteria in screening the four catalysts for kinetics studies in the next section.

6.5 Screening of Ni(x)/Ce-Al_2O_3 catalysts for kinetics studies

It was desired to select the catalyst with the highest hydrogen (or syngas) production rate and least tendency for coke formation. Therefore, the four catalysts with the general composition Ni(x)/Ce-Al_2O_3 (x = 5, 10, 15 and 20 wt%) were screened for fluidized bed gasification at 650 °C, 1 atm and biomass concentration of 15 wt% for 20 seconds. The result of the catalyst evaluation is shown in Figure 6.3. The catalyst with 20 wt% nickel loading turned out to be the best in terms of desired product (i.e. syngas) composition. Moreover, the lowest proportion of CO_2 was observed at this particular loading. We propose that this phenomenon is related to a unique interaction of nickel with the new Ce-Al_2O_3 support at high nickel loading (i.e. above 15 wt%). The additional nickel and Ni-O-Ce species in Ni(20)/Al_2O_3 tend to suppress CO disproportionation to CO2 and coke. This is particularly supported by the fact that the composition of the two other components (i.e. H_2 and methane) remain fairly the same after 15wt% nickel loading. It

is possible that at 20 wt% nickel loading, ceria interacts with excess nickel to induce a strong electronic perturbation which will help in suppressing the conversion of CO to CO_2 and carbon deposits, as reported in Senanayake et al[145].

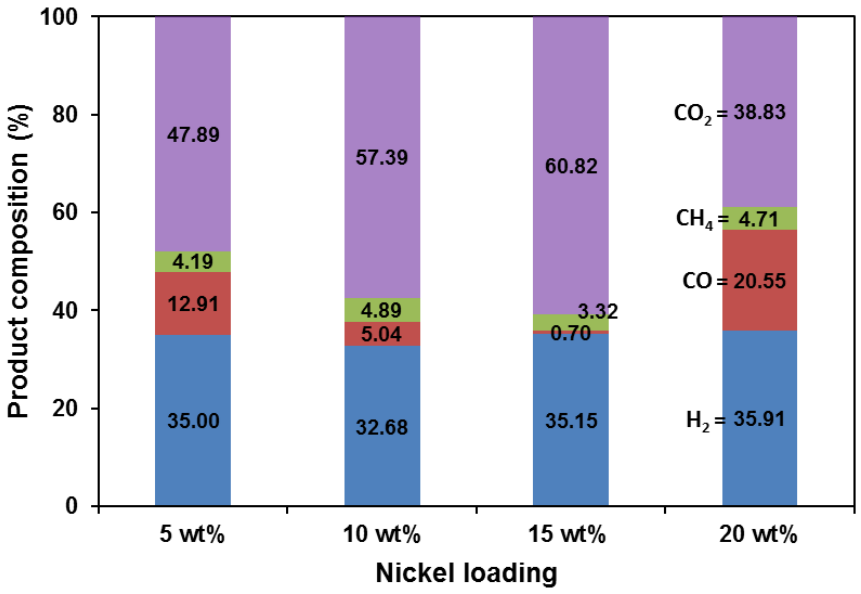

Figure 6.3: Result of catalyst evaluation at 650 °C, 1 atm for 15 wt % glucose, 20 s.

In order to ascertain the extent of carbon deposition during catalyst evaluate (See Figure 6.4). This analysis is very important due to the susceptibility of a nickel catalyst to coke deposition during steam gasification of biomass[94,124,146,147]. Moreover, high acidity leads to a significant extent of cracking, resulting in a high extent of carbon deposition. It is expected therefore that a moderately acidic catalyst with a high nickel loading such as Ni(20)/Al_2O_3 will exhibit the lowest extent of carbon deposition as compared to the rest of the catalyst samples with a higher amount of acid sites.

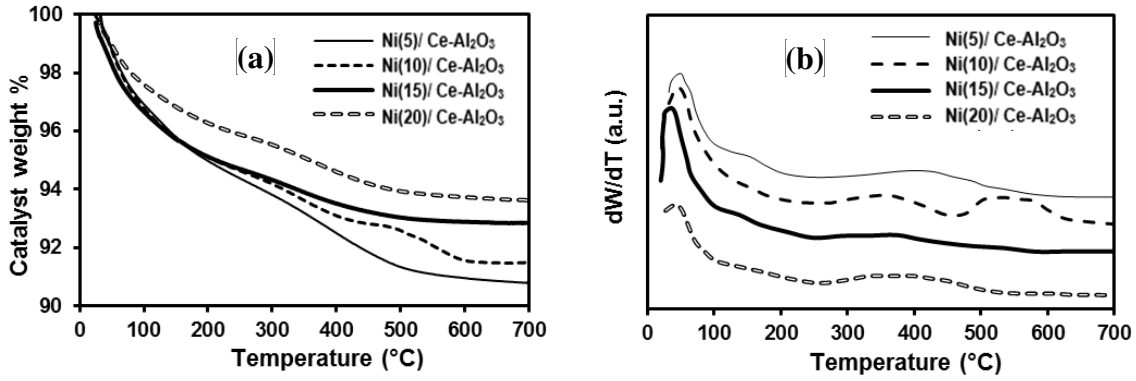

Figure 6.4: Thermograms of the spent catalysts: (a) TGA (b) DTG

Figure 6.4 (a) indicates that the extent of coking decreased as the nickel loading was increased from 5 to 20 wt%. The first transition (up to 500 °C) is due to water desorption, oxidation of volatile intermediate compounds as well as amorphous carbon[48,112,113]. The transformation happening beyond 500 °C is ascribed to the oxidation/decomposition of stable coke and carbides, which are the main causes for nickel catalyst deactivation. This is more pronounced in Ni(10)/Ce-Al_2O_3 [See Figure 6.4 (b)]. Considering the trend in these thermograms and the results of catalyst evaluation (Shown in Figure 4), we infer that the ceria dopant has stabilized the support and reduced the tendency of nickel carbide formation and hence tackled catalyst deactivation. In particular, Ni(20)/Ce-Al_2O_3 which yield the highest amount of syngas exhibit the lowest extent of coke formation by suppressing CO disproportionation as explained earlier.

Combining the catalyst evaluation results with the TG/DTG and NH_3-TPD results, we conclude that the acidity of the catalyst plays a significant role in cracking the biomass

intermediate compounds to generate syngas. However, a highly acidic catalyst such as Ni(5)/Ce-Al_2O_3 catalyst will give a high amount of coke. Hence, the outstanding performance of Ni(20)/Ce-Al_2O_3 is correlated to its moderate acidity, which balances its cracking ability and at the same time reduced the extent of coking.

6.6 Estimation of kinetic parameters

In order to solve the kinetic model, we need to determine some of the parameters independently. This "*decoupling"* minimizes the problem of over-parameterization of the model. Therefore, equilibrium constants for water gas shift, steam reforming and reverse dry reforming of methane were obtained from Thermosolver software (See Table 6.4). For each temperature, we used the product composition after 5 sec. to determine the equilibrium composition for each of the three reactions (i.e. WGS, SRM and RDRM). These data were then used to determine the equilibrium rate constants.

Table 6.4: Equilibrium constants for WGS, SRM, and RDRM.

Temperature (°C)	K_{WGS}	K_{SRM}	K_{RDRM}
550	3.640	0.0799	45.500
600	2.690	0.518	5.190
650	2.060	2.760	0.747
700	1.630	12.400	0.131

First, the coupled ordinary differential equations were solved numerically using 4th order Runge Kutta algorithm (Mathematica's ParametricNDSolveValue function) for the given time interval ($5 \leq t(s) \leq 25$). The initial concentrations were at t = 5 s. The regression

was then performed using Levenberg-Marquardt algorithm (Mathematica's NonLinearModelFit function). This minimizes the sum of square error between experimental data and model predicted values. The results were evaluated on the basis of the following criteria: (i) high coefficient of determination R^2, (ii) Positive values for the kinetic parameters, and (iii) narrow confidence intervals for the kinetic parameters.

Figure 6.5a–d visualize the performance of our model in predicting the experimental data for all the products, each at 550, 600, 650 and 700 °C. In all cases, the fittings were excellent with high R^2 values ($R^2 \geq 0.99$) and AIC = -415.83. In Figure 6.5a (T = 700 °C), methane composition remained fairly the same after 5 s. Both hydrogen and CO_2 increased steadily, while partial pressure of CO decreased proportionally. This indicates that water gas shift reaction was favored with time, and that significant proportion of hydrogen could be obtained at longer residence times or higher temperature. Considering CO and CO_2 profiles, we see that they progressed towards a plateau around t = 25 s, indicating that the active re-distribution of the carbon content in the products, is mainly favored by such reactions involving the consumption of CO species (i.e. WGS) and CO_2 formation (i.e. WGS and RDRM).

In Figure 6.5b (T = 650 °C), hydrogen production improved reasonably as the time progressed. This is ascribed mainly to the water gas shift reaction. Accordingly, the partial pressure of steam decreased while that of CO_2 increased almost proportionately with that hydrogen.

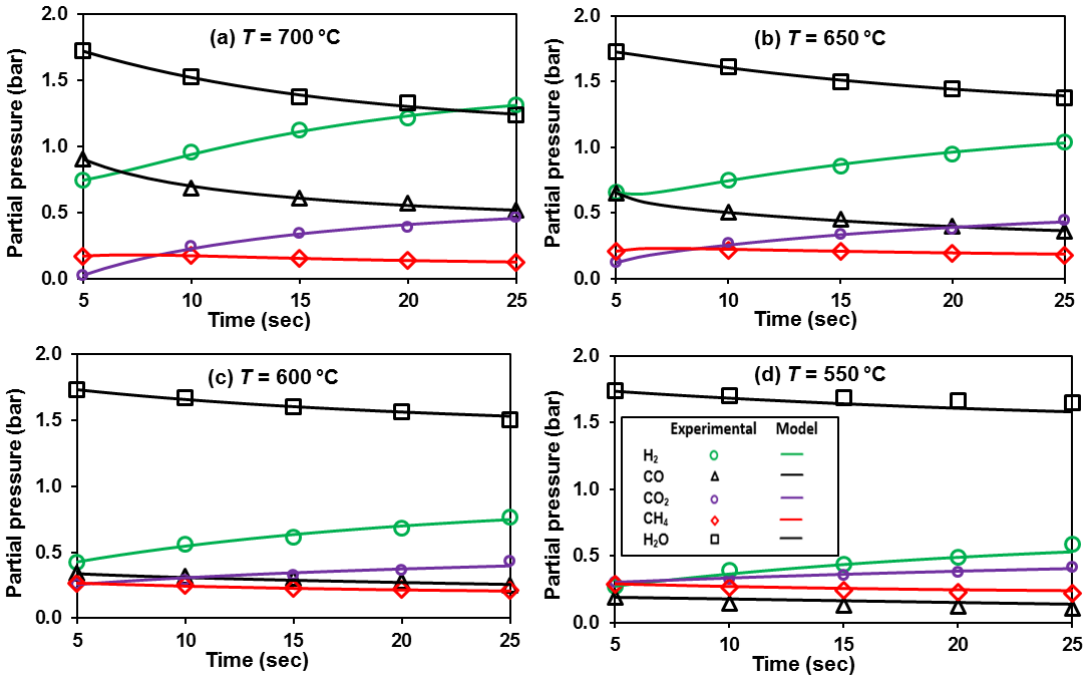

Figure 6.5: Experimental versus predicted product distributions

Finally, the results of Figure 6.5d (T = 550 °C) shows that the gaseous products recombine relatively slowly than at higher temperature. This means that a much longer time will be needed to attain equilibrium at this temperature. This asserts the fact that steam gasification of biomass is favored by a high operating temperature and further justifies the present kinetic studies because the product compositions vary significantly with time.

Table 6.5 gives the kinetic parameters for the model. The values of the degrees of freedom for the model parameters and corrected total were 16, and 99 respectively.

Table 6.5: Kinetic parameters for the model.

Parameter	Present study (Ni(20)/Ce(1)-Al_2O_3	Jahirul 2014 [4] (Ni(20)/La(5)-Al_2O_3	Salaices 2010 [135] Ni/α-Al_2O_3
k^0_{WGS}(mmol/gcat.s.bar^2)	7.76E-2	6.1E-02 ± 1.2E-03	3.07E-03
E_{WGS}(kJ/mol)	20.02±1.06	33.36± 13.06	53.1
k^0_{SRM}(mmol/gcat.s.bar^2)	4.13E-2	1.16E-1 ± 4.18E-2	9.21E-7
E_{SRM}(kJ/mol)	4.23±0.41	68.11±9.88	93
k^0_{RDRM}(mmol/gcat.s.bar^2)	3.57E-2	3.81E-1 ± 1.98E-2	2.22E-6
E_{RDRM}(kJ/mol)	7.90±.63	89.71 ± 19.73	75.8
$K^{ads}_{H_2}$(bar^{-1})	1.11E-5	-	-
$\Delta H^{ads}_{H_2}$(kJ/mol)	0.13	-	-
K^{ads}_{CO}(bar^{-1})	1.10E-5	-	-
ΔH^{ads}_{CO}(kJ/mol)	0.14	-	-
$K^{ads}_{CO_2}$(bar^{-1})	1.73E-5	-	-
$\Delta H^{ads}_{CO_2}$(kJ/mol)	2.06E-9	-	-
$K^{ads}_{CH_4}$(bar^{-1})	1.11E-5	-	-
$\Delta H^{ads}_{CH_4}$(kJ/mol)	0.050	-	-
$K^{ads}_{H_2O}$(bar^{-1})	1.10E-5	-	-
$\Delta H^{ads}_{H_2O}$(kJ/mol)	0.14	-	-

The values of intrinsic rate constants are comparable and fall in the same range with those reported in Salaices et al.[135] and Jahirul[4]. Our assumption that the dominant reactions are WGS, SRM and DRDM is justified considering the high E_a values for the rest of the possible reactions as reported in Hejazi et al.[131]: (1) Boudouard reaction (E_a = 215 kJ/mol), coke gasification (E_a = 237 kJ/mol) and methanation (E_a = 94.8 kJ/mol). Therefore this catalytic system is not only stable but highly selective for syngas at moderate temperature with fast reaction rates.

Figure 6.6 illustrates the parity plot between the experimental data and the model predicted values. It is evident from the plot that the model describes glucose gasification in the riser simulator sufficiently. Therefore, this type of kinetic model could be applied

for the purpose of data prediction or computational fluid dynamics study in the riser, within the experimental conditions.

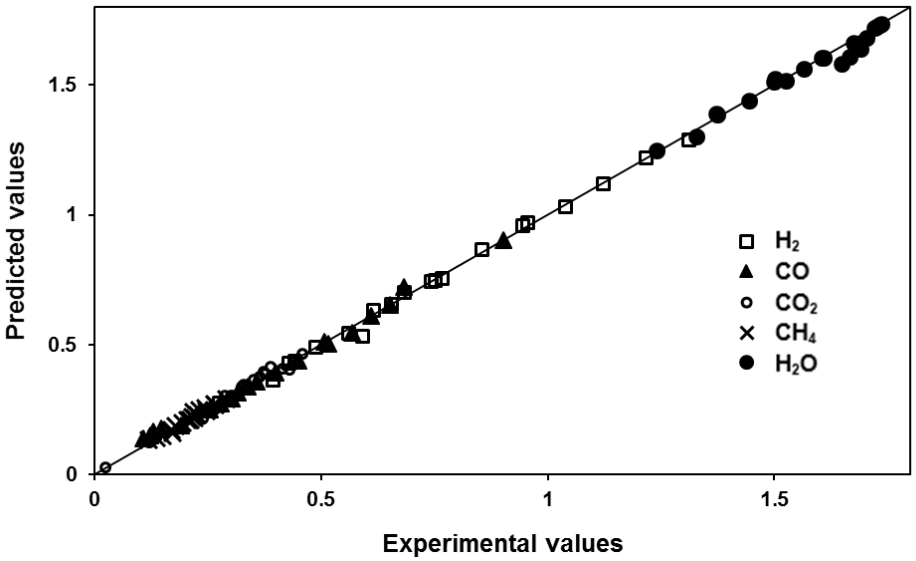

Figure 6.6: Experimental versus predicted partial pressures of all the reacting species.

It should be noted, however, that the kinetic parameters reported in this work, are only valid for this particular catalyst system. For another catalytic system having a similar product composition, the same procedure developed in this work could be applied conveniently to regress the experimental data and obtain the corresponding kinetic parameters.

Table 6.6 shows that most of the cross-correlation coefficients are less than 0.94. This means that the parameters are independent of one another. The fact that the coefficients

in the case of k_{wgs}, k_{srm} and k_{rdrm} are greater 0.94 is due to the fact that the reactions depend on common reacting species.

Table 6.6: Cross-correlation matrix for the model parameters.

	k_{wgs0}	k_{srm0}	k_{rdrm}	E_{wgs}	E_{srm}	E_{rdrm}	$K_{A,H2\_0}$	K_{A,CO_0}	$K_{A,CO2\_0}$	$K_{A,CH4\_0}$	$K_{A,H2O\_0}$	ΔH_{H2}	ΔH_{CO}	ΔH_{CO2}	ΔH_{CH4}	ΔH_{H2O}
k_{wgs}	1.000															
k_{srm}	1.000	1.000														
k_{rdrm}	0.997	0.998	1.000													
E_{wgs}	0.712	0.708	0.700	1.000												
E_{srm}	0.791	0.789	0.785	0.912	1.000											
E_{rdrm}	0.523	0.512	0.462	0.571	0.618	1.000										
$K_{A,H2\_0}$	0.665	0.660	0.641	0.575	0.732	0.650	1.000									
K_{A,CO_0}	0.816	0.817	0.825	0.797	0.765	0.336	0.298	1.000								
$K_{A,CO2\_0}$	0.882	0.886	0.895	0.616	0.629	0.287	0.255	0.905	1.000							
$K_{A,CH4\_0}$	0.280	0.284	0.292	0.295	0.363	0.091	0.363	0.429	0.164	1.000						
$K_{A,H2O\_0}$	0.929	0.927	0.920	0.560	0.639	0.503	0.604	0.614	0.805	-0.068	1.000					
ΔH_{H2}	-0.765	-0.764	-0.755	-0.500	-0.571	-0.463	-0.540	-0.606	-0.649	-0.342	-0.678	1.000				
ΔH_{CO}	-0.441	-0.440	-0.428	-0.463	-0.465	-0.399	-0.221	-0.551	-0.479	-0.254	-0.311	0.262	1.000			
ΔH_{CO2}	0.653	0.525	0.432	0.602	0.904	0.302	0.486	0.593	0.286	0.472	0.792	0.375	0.557	1.000		
ΔH_{CH4}	0.534	0.526	0.507	0.552	0.520	0.499	0.489	0.449	0.380	0.234	0.460	-0.677	-0.385	0.617	1.000	
ΔH_{H2O}	-0.436	-0.440	-0.455	-0.386	-0.430	-0.077	-0.439	-0.432	-0.296	-0.688	-0.221	0.431	-0.149	0.333	-0.312	1.000

This is consistent with the fact that each of these reactions have common reacting species (i.e H_2, CO, CO_2, CH_4 and H_2O). In summary the proposed model adequately fit the experimental data, with reasonable statistical parameters.

In summary, the detailed kinetic modeling of steam gasification of glucose over Ni/Ce-doped-Al_2O_3 was carried out under turbulent fluidized bed conditions. The following points should be stressed. Ni(20)/Ce-meso-Al_2O_3 is the best catalyst loading for steam gasification of glucose at low temperature (i.e. $550 \leq T \leq 700$ °C) under

fluidized bed conditions. This catalyst loading gives the highest percentage of syngas without tempering with hydrogen proportion and minimized coke formation as compared to the catalysts with 5, 10 and 15 wt% loadings. The overall mechanism of steam gasification of glucose over Ni(20)/Ce-meso-Al_2O_3 in a fluidized bed comprises of instantaneous conversion of glucose into CO, CO_2, CH_4, and H_2 with negligible tar and char. The reaction is kinetically limited and tends to approach steady state at 25 s, at a moderate reaction temperature (i.e. 700 °C). Kinetics of steam gasification of glucose over Ni(20)/Ce-meso-Al_2O_3 proceeded via a combination of water gas shift, steam reforming of methane, and reverse dry reforming of methane in a Langmuir-Hinshelwood type of kinetic model with reasonable statistical parameters. The kinetic model adequately fit the experimental data, with R^2 = 0.999, and AIC = -415.83, with pre-exponential Arrhenius rate constants $k^0_{WGS} = 7.76x10^{-2}$; $k^0_{SRM} = 4.13x10^{-2}$; and $k^0_{RDRM} = 3.57x10^{-2}$ mmol/gcat.s.bar^2, within the experimental range of $550 \leq T \leq 700$ °C. The corresponding activation energies were $E_{WGS} = 20.0$ kJ/mol; $E_{SRM} = 4.20$ kJ/mol and $E_{WGS} = 7.90$ kJ/mol respectively. These values of activation energy having the same order of magnitude as those reported in the literature. The kinetic model parameters could be used to determine the desired operating parameters for a target syngas composition from a similar feedstock and similar catalytic system. The modeling procedure could be applied conveniently to a different catalytic system having a similar product composition in a similar reactor set up to obtain the necessary kinetic parameters.

CHAPTER 7

THERMODYNAMICS OF BIOMASS GASIFICATION

7.1 Introduction

The complex reactions network involved in biomass gasification plus the occurrence of several intermediate products necessitates the development of a rigorous non-stoichiometric thermodynamic model [35]. Therefore, Gibbs free energy minimization technique was adopted to predict the equilibrium product composition of biomass gasification experiments. This approach is accurate because the reaction intermediates are not involved. It should be noted however, that the total Gibbs free energy of the solid/gaseous system has a high degree of nonlinearity and therefore the method requires computer programming [148]. In this Chapter, we developed a rigorous thermodynamic model for biomass gasification process under sub and supercritical water conditions.

7.2 Model development

Figure 1 depicts the basic principle of the Gibbs energy minimization (GEM) model. The Gibbs free energy minimization reactor serves as a black box that converts the wet biomass feed to the various species in the product stream (syngas, methane and carbon dioxide). It satisfies (1) the equilibrium requirement of minimum total Gibbs free energy of the mixture, (2) the non-negative constraint on the molar fractions, (3) the conservation of the atomic species (i.e. the material balance), and (4) the cubic EoS,

which involves Z (i.e. the compressibility factor). The model formulation proceeds as follows.

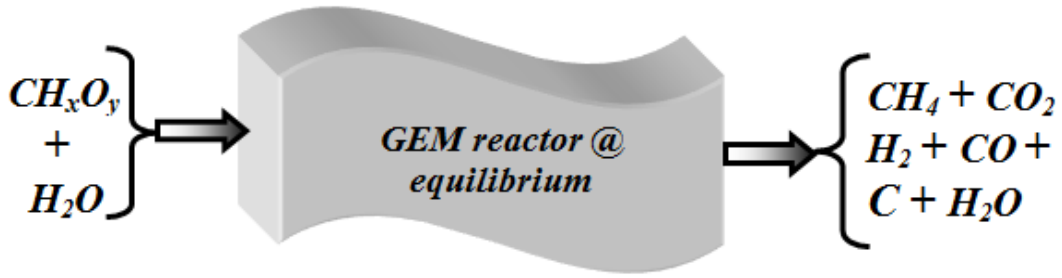

Figure 7.1: Schematic representation of the principle of direct GEM

The total Gibb's free energy consists of the ideal gas component and the residual contribution. Thus,

$$G^{tot} = G^{ideal} + G^{Res} \tag{7-1}$$

Therefore our optimization problem was formulated as follows:

$$obj\ fxn = Minimize\left(G^{tot}\left(n_{H_2}, n_{H_2O}, n_{CH_4}, n_{CO}, n_{CO_2}, n_C\right)\right) \tag{7-2}$$

Subject to;

$$n_j \geq 0 \tag{7-3}$$

$$\begin{bmatrix} 2 & 2 & 4 & 0 & 0 & 0 \\ 0 & 0 & 1 & 1 & 1 & 1 \\ 0 & 1 & 0 & 1 & 2 & 0 \end{bmatrix} \begin{bmatrix} n_{H_2} \\ n_{H_2O} \\ n_{CH_4} \\ n_{CO} \\ n_{CO_2} \\ n_C \end{bmatrix} = \begin{bmatrix} A_H \\ A_C \\ A_O \end{bmatrix} \tag{7-4}$$

$$f(Z) = 0 \tag{7-5}$$

where $f(Z)$ refers to the EoS in terms of the compressibility factor, Z.

Now, the ideal gas Gibbs free energy of the pure component is given by [109]:

$$G_i^{ideal} = G_{i,T_0} + \int_{T_0}^{T} C_{P_i} dT - T \int_{T_0}^{T} \frac{C_{P_i}}{T} dT + RTln\left(\frac{P}{P_1}\right) - S_{i,T_0}(T - T_0) \quad 7\text{-}6$$

where the temperature of T_0 = 298.15 K is the reference temperature, and P_1 is the reference pressure.

Thus, the ideal gas Gibbs free energy could be evaluated as:

$$G^{ideal} = \sum_{i=1}^{n} y_i G_i^{ideal} + RT \sum_{i=1}^{n} y_i ln(y_i) \quad 7\text{-}7$$

7.2.1 Equations of state

We adopted Peng–Robinson and Duan equations of state separately to determine G^{Res} and Z. These equations were employed to account for non-ideality of the gaseous components of our system. Indeed, the EoS were used to derive the residual Gibbs free energy. While Peng–Robinson EoS is widely applied in refinery and gas processing industries for pure- and multicomponent systems [149], Duan EoS has been developed particularly for CH_4-CO_2-H_2O mixture, spanning through a wide range of temperature (i.e. 0 to 1000 °C) and pressure (i.e. 0 to 8000 bar) [150]. It is also worth noting that Duan EoS is very effective in modeling supercritical water.

7.2.2 Peng–Robinson equation

The Peng–Robinson equation of state is given by:

$$P = \frac{RT}{V-b} - \frac{a\alpha(T)}{V^2+2bV-b^2} \quad 7\text{-}8$$

where P is the pressure of the system, T is the absolute temperature, V is the molar volume, R is the ideal gas constant, and a and b are parameters for the Peng–Robinson

equation of state. These are related to the critical temperature T_c and pressure P_c of the gas as follows:

$$a = \frac{0.45724 R^2 T_c^2}{P_c} \quad (7\text{-}9)$$

$$\alpha = [1 + \kappa(1 - T_r^{0.5})]^2 \quad (7\text{-}10)$$

$$T_r = T/T_c \quad (7\text{-}11)$$

$$b = 0.07780 RT_c/P_c \quad (7\text{-}12)$$

$$\kappa = 0.37464 + 1.54226\omega - 0.26993\omega^2 \quad (7\text{-}13)$$

where ω is the acentric factor.

This EoS is applied to gaseous mixtures using the classical mixing rules.

Mixing parameters are thus given by:

$$a_{mix} = \sum_{i=1}^{n} \sum_{i=1}^{n} y_i y_j \sqrt{a_i a_j}\left(1 - k_{i,j}\right) \quad (7\text{-}14)$$

$$b_{mix} = \sum_{i=1}^{n} y_i b_i \quad (7\text{-}15)$$

Finally, one can derive the following expression for G_{P-R}^{Res},

$$G_{P-R}^{Res} = RT(Z - 1 - Log[Z]) + \int_{\infty}^{V} \left(\frac{RT}{V} - P\right) dV \quad (7\text{-}16)$$

$$\frac{G_{P-R}^{Res}}{RT} = Z - 1 - Log\left(Z - \frac{Pb_{mix}}{RT}\right) - \frac{a_{mix}}{2\sqrt{2} b_{mix} RT} ln\left(\frac{V_{mix} + \left(1+\sqrt{2}\right) b_{mix}}{V_{mix} + \left(1-\sqrt{2}\right) b_{mix}}\right) \quad (7\text{-}17)$$

Table 7.1 shows the binary interaction parameters, $k_{i,j}$, for Peng–Robinson EoS, as obtained from Aspen-HYSYS.

Table 7.1: Peng–Robinson EoS Interaction Parameters.

	Methane	Hydrogen	Water	CO	CO_2
Methane	0	0.2020	0.5000	0.0210	0.1000
Hydrogen	0.2020	0	-0.2998	0.0253	0.1202

Water	0.5000	-0.2998	0	-0.3896	0.0445
CO	0.0210	0.0253	-0.3896	0	-0.0314
CO_2	0.1000	0.1202	0.0445	-0.0314	0

7.2.3 Duan's equation of state

The Duans EoS is given by [12,151]

$$P = \frac{RT_m}{V_m}\left(1 + \frac{a_1 + a_2/{T_m}^2 + a_3/{T_m}^3}{V_m} + \frac{a_4 + a_5/{T_m}^2 + a_6/{T_m}^3}{{V_m}^2} + \frac{a_7 + a_8/{T_m}^2 + a_9/{T_m}^3}{{V_m}^4} + \frac{a_{10} + a_{11}/{T_m}^2 + a_{12}/{T_m}^3}{{V_m}^5} + \frac{a_{13}}{{V_m}^2 {T_m}^3}\left(1 + \frac{a_{14}}{{V_m}^2}\right) Exp\left(\frac{-a_{14}}{{V_m}^2}\right)\right) \quad 7\text{-}18$$

where T_m refers to the temperature of the reference-compound (i.e., methane in this case)

$$T_m = \frac{145 * T}{\varepsilon_m} \quad 7\text{-}19$$

The reference volume is related to the volume of the mixture as follows:

$$V = 1000 V_m \left(\frac{\sigma_m}{3.691}\right)^3 \quad 7\text{-}20$$

Here, we calculate the residual Gibbs free energy using the following expression:

$$G_{Duan}^{Res} = RT_m(Z - 1 - Log[Z]) + \int_{\infty}^{V_m} \left(\frac{RT_m}{V_m} - P\right) dV_m \quad 7\text{-}21$$

Hence,

$$G_{Duan}^{Res} = R\mathrm{T_m}(Z - 1 - \mathrm{Log}[Z]) + \mathrm{a13}\left(\frac{\frac{\mathrm{R}}{{\mathrm{T_m}}^2} - \frac{e^{-\frac{\mathrm{a14}}{{\mathrm{V_m}}^2}}\mathrm{R}}{{\mathrm{T_m}}^2}}{\mathrm{a14}} - \frac{e^{-\frac{\mathrm{a14}}{{\mathrm{V_m}}^2}}\mathrm{RT_m}}{2{\mathrm{T_m}}^3{\mathrm{V_m}}^2}\right) + \frac{\mathrm{a10RT_m}}{5{\mathrm{V_m}}^5} + \frac{\mathrm{a12R}}{5{\mathrm{T_m}}^2{\mathrm{V_m}}^5} + \frac{\mathrm{a11R}}{5\mathrm{T_m}{\mathrm{V_m}}^5} + \frac{\mathrm{a7RT_m}}{4{\mathrm{V_m}}^4} + \frac{\mathrm{a9R}}{4{\mathrm{T_m}}^2{\mathrm{V_m}}^4} + \frac{\mathrm{a8R}}{4\mathrm{T_m}{\mathrm{V_m}}^4} + \frac{\mathrm{a4RT_m}}{2{\mathrm{V_m}}^2} + \frac{\mathrm{a6R}}{2{\mathrm{T_m}}^2{\mathrm{V_m}}^2} + \frac{\mathrm{a5R}}{2\mathrm{T_m}{\mathrm{V_m}}^2} + \frac{\mathrm{a1RT_m}}{\mathrm{V_m}} + \frac{\mathrm{a3R}}{{\mathrm{T_m}}^2\mathrm{V_m}} + \frac{\mathrm{a2RT_m}}{{\mathrm{T_m}}^2\mathrm{V_m}} \quad 7\text{-}22$$

Inserting the expressions for V_m and T_m we obtained the final expression as:

$$G_{Duan}^{Res} = \frac{Ra_1 c_2 \sigma_m^3}{Z c_1 \varepsilon_m} + \frac{Ra_2 \varepsilon_m \sigma_m^3}{ZT^2 c_1 c_2} + \frac{Ra_3 \varepsilon_m^2 \sigma_m^3}{ZT^3 c_1 c_2^2} + \frac{Ra_4 c_2 \sigma_m^6}{2Z^2 T \varepsilon_m c_1^2} + \frac{Ra_5 \varepsilon_m \sigma_m^6}{2Z^2 T^3 c_1^2 c_2} + \frac{Ra_6 \varepsilon_m^2 \sigma_m^6}{2Z^2 T^4 c_1^2 c_2^2} + \frac{Ra_7 c_2 \sigma_m^{12}}{4Z^4 T^3 \varepsilon_m c_1^4} + \frac{Ra_8 \varepsilon_m \sigma_m^{12}}{4Z^4 T^5 c_1^4 c_2} + \frac{Ra_9 \varepsilon_m^2 \sigma_m^{12}}{4Z^4 T^6 c_1^4 c_2^2} + \frac{Ra_{10} c_2 \sigma_m^{15}}{5Z^5 T^4 \varepsilon_m c_1^5} + \frac{Ra_{11} \varepsilon_m \sigma_m^{15}}{5Z^5 T^6 c_1^5 c_2} + \frac{Ra_{12} \varepsilon_m^2 \sigma_m^{15}}{5Z^5 T^7 c_1^5 c_2^2} + \frac{Ra_{13} \varepsilon_m^2}{a_{14} T^2 c_2^2} \left(1 - e^{-\frac{a_{14} \sigma_m^6}{c_1^2 T^2 Z^2}} - \frac{e^{-\frac{a_{14} \sigma_m^6}{c_1^2 T^2 Z^2}} \sigma_m^6}{2T^2 Z^2 c_1^2} a_{14} \right) + \frac{RT c_2}{\varepsilon_m} (Z - 1 - \mathrm{Log}[Z])$$

7-23

where σ_m and ε_m are the Lennard−Jones mixing parameters given by:

$$\sigma_m = \sum_{i=1}^{5} \sum_{i=1}^{5} y_i y_j k_{i,j} \frac{(\sigma_i + \sigma_j)}{2} \quad 7\text{-}24$$

$$\varepsilon_m = \sum_{i=1}^{5} \sum_{i=1}^{5} y_i y_j k_{i,j} \sqrt{\varepsilon_i \varepsilon_j} \quad 7\text{-}25$$

Table 7.2 provides the relevant parameters to be used with Eq. 15.

Table 7.2: Parameters for Eq. 15 [151].

Parameter	Value
a_1	0.03755
a_2	-1.0873
a_3	1.1096E+06
a_4	5.4159
a_5	112.0946
a_6	-5921.9139
a_7	4.372E-06
a_8	4.9579
a_9	-164.9029
a_{10}	-7.0744E-08
a_{11}	9.6573
a_{12}	0.4879
a_{13}	16225.7402
a_{14}	0.00899
c_1	0.050284
c_2	145

In order to illustrate the material balance for the system, the following number assignments (Table 7.3) was done to identify the species involved in the biomass gasification:

Table 7.3: Number assignment for each component.

Number	1	2	3	4	5	6
Component	CH_4	H_2	H_2O	CO	CO_2	$C_6H_{12}O_6$

The overall reaction taking place is given below:

$$C_6H_{12}O_6 + rH_2O \rightarrow mCH_4 + (r + 6 - 2m)H_2 + nCO + (6 - m - n)CO_2 \quad 7\text{-}26$$

Thus, the constraint equations writes as follows:

C: $$n_1 + n_4 + n_5 + 6n_6 = 6 \quad 7\text{-}27$$

H: $$4n_1 + 2n_2 + 2n_3 + 12n_6 = 12 + 2r \quad 7\text{-}28$$

O: $$n_3 + n_4 + 2n_5 + 6n_6 = 6 + r \quad 7\text{-}29$$

7.3 Results of thermodynamic modeling

In order to investigate the model performance with respect to the real gasification products, we proceed as follows. Aspen-HYSYS version 7.3 was employed to compute the compressibility Z factor of the product mixture. This was compared with the model value, considering extreme cases for the system's temperature and pressure. In all cases, the percentage error was found to be less than 9% (See Table 7.4), and hence the model is sufficiently validated.

Table 7.4: Comparison of Z-factor of the model and those of similar gas mixture

T (K)	P (bar)	CH4	H2	H2O	CO	CO2	Z-factor, mix	Z model	% error
1000	1.00	0.001	0.419	0.298	0.140	0.141	1.001	1.000	0.10
1000	222.00	0.151	0.101	0.532	0.028	0.188	1.013	1.000	1.30

647	222.00	0.195	0.004	0.605	0.000	0.197	0.867	0.803	7.90
647	1.00	0.167	0.082	0.543	0.002	0.207	0.899	0.989	9.00

2

Figure 7.2 shows a typical range of values of the compressibility factor, *Z* obtained from the model simulation. It is obvious that Z deviates significantly from unity, thereby justifying the need to adequately account for the residual Gibbs free energy of the mixture (Eqs 9, and 14 for Peng–Robinson and Duan, respectively).

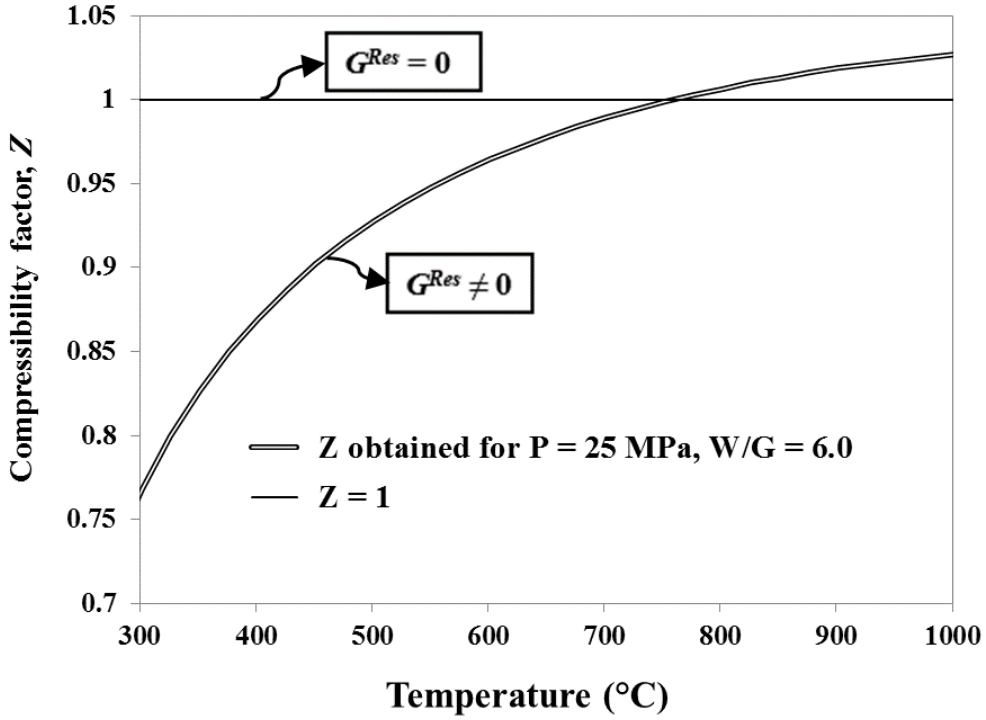

Figure 7.2: Typical range of values of the Compressibility factor.

Figure 7.3 (a), (b), (c), (d) illustrate the results for thermodynamic equilibrium composition of SCWG products obtained using different values of water to glucose ratio (i.e., 6 and 9), and pressure (i.e., 1 and 25 MPa).

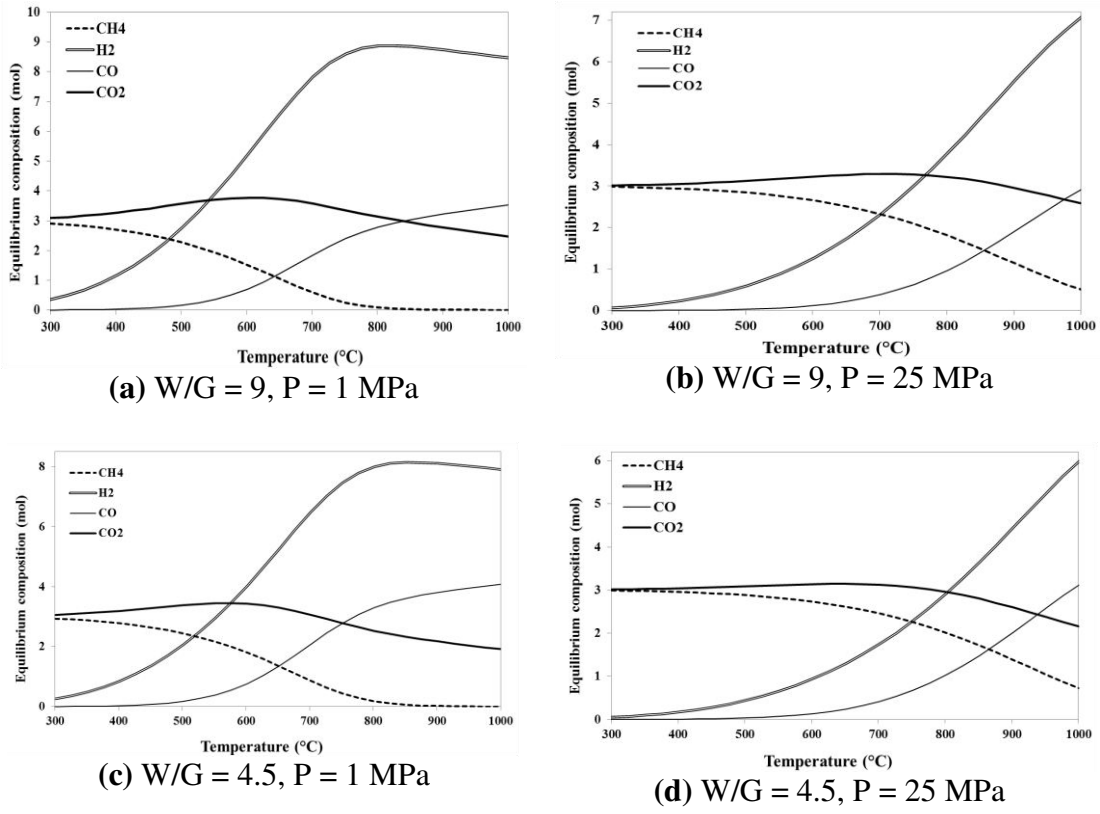

(a) W/G = 9, P = 1 MPa

(b) W/G = 9, P = 25 MPa

(c) W/G = 4.5, P = 1 MPa

(d) W/G = 4.5, P = 25 MPa

Figure 7.3: Equilibrium product composition

Figure 7.4 shows the plots for hydrogen selectivity corresponding to the plots of Figure 7.3. The selectivity is very low below 500 °C (i.e. H_2 selectivity < 20 %, on water free basis). Because the hydrogen forming reaction networks are temperature sensitive, the selectivity increased rapidly, approaching 90% at T > 800 °C.

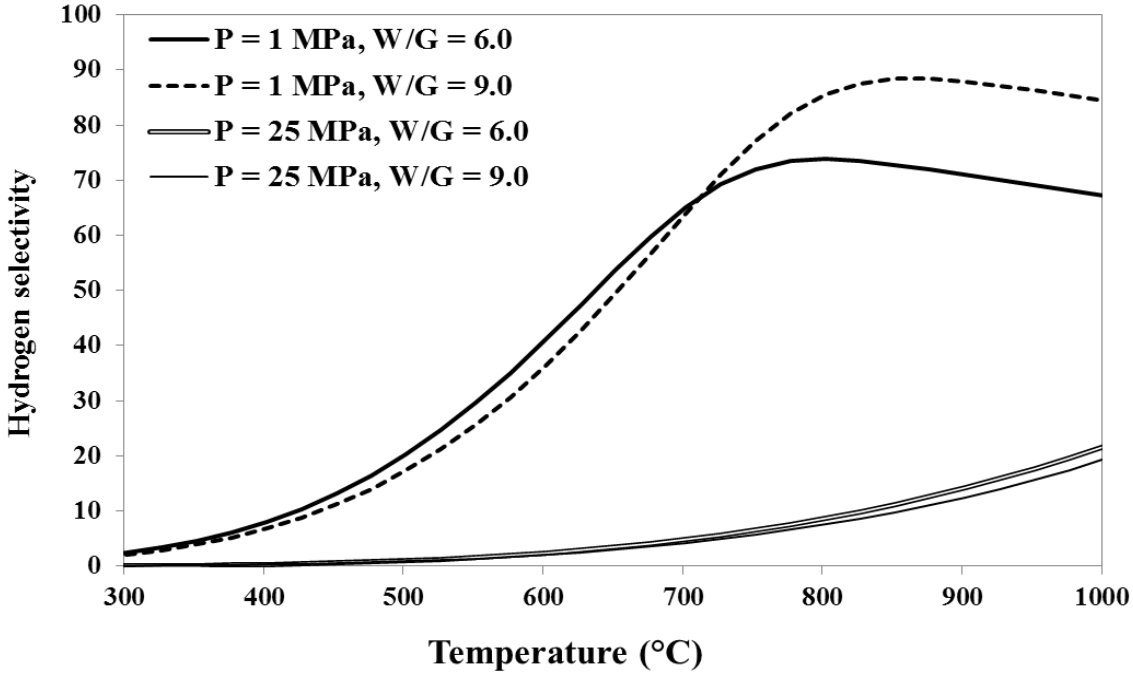

Figure 7.4: Hydrogen selectivity plots for the corresponding plots of Figure 7.3

Figure 8, shows the effect of temperature, pressure and water to biomass ratio on syngas composition. It is noticed that hydrogen to carbon monoxide ratio is very sensitive to operating temperature, especially when the temperature is below 600 °C. For example at 400 °C, the values are in excess of 20:1.

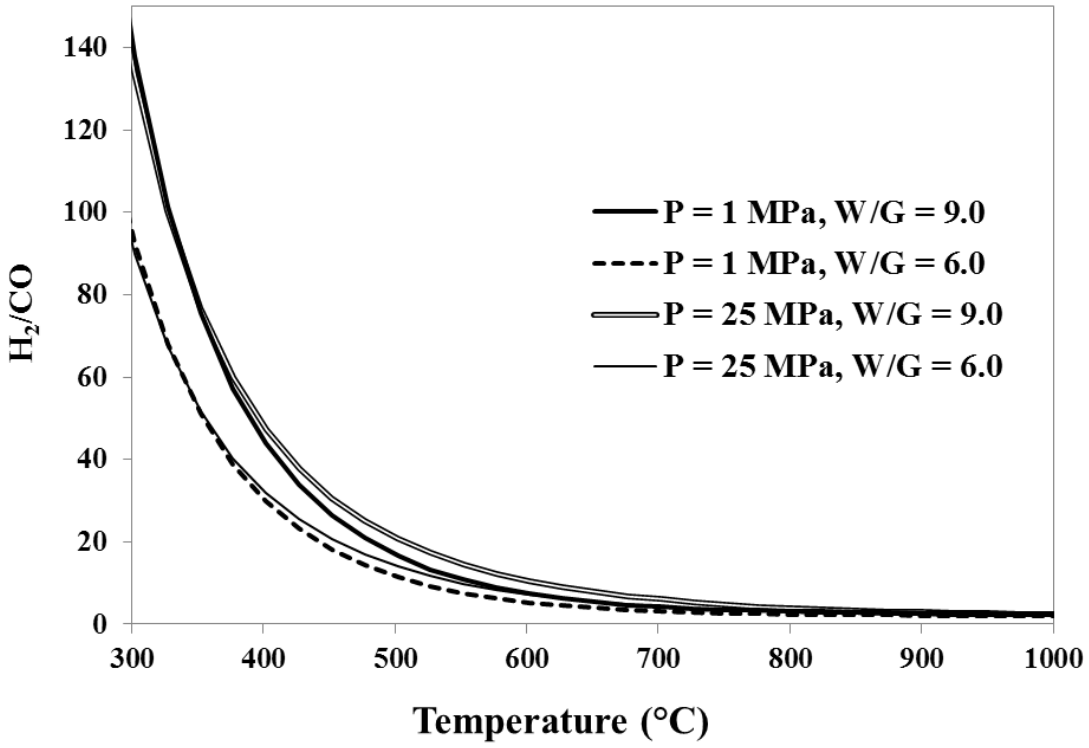

Figure 7.5: H_2/CO ratio plots for the corresponding plots of Figure 7.3.

Since it is desirable to develop catalyst which can be used at low temperatures to achieve reasonable amount of hydrogen or syngas, the information in this Figure 7.5 could be useful for achieving a targeted a gasification composition. Moreover, water to biomass ratio affected the syngas composition. For example, at 400 ^{O}C and 25 MPa, an increase in W/G ratio from 6 to 9 led to an increase in H_2/CO ratio from ~32 to ~47. On the other hand, operating pressure has little or no effect on the syngas composition. This finding could be useful in the design and optimization of SCWG plants.

7.4 Experimental versus thermodynamic analysis

In this section, the results of SCWG of glucose gasification using modified nickel alumina catalyst reported by our research group were compared with thermodynamic model predictions. The model is capable of determining the equilibrium product composition of any biomass, when gasified at any state (T, P) including supercritical water conditions. Furthermore, unlike the commercial Gibbs' energy minimization software, which work with a limited number of model compounds, our model is applicable to any real biomass of known composition (i.e. CH_xO_y, where x and y are determined from the ultimate analysis of the biomass in question). This is of utmost importance in order to see how far are the experimental data from the thermodynamic limits for the product components of interest (i.e., hydrogen and carbon monoxide). This will define a "*challenge gap*" for subsequent research work; especially in terms of the catalyst design and development, as well as process optimization.

In summary, this section is organized as follows:

- Development of a thermodynamic model based on Gibbs' free energy, which will be minimized according to material balance constraints to give the equilibrium product distributions.
- Comparison of the performance of the two thermodynamic models using residual Gibbs' energy function derived from either the Peng–Robinson EoS or the Duan EoS.
- Validation of the model by comparing the obtained compressibility factor Z with its counterpart determined for a gas stream having the same composition at selected set of operating conditions in a process simulator (i.e. Aspen-HYSYS).

7.5 Application in gasification of real biomass

To further emphasize on the rigorous nature of the thermodynamic model developed in this work, we have obtained some real biomass compounds and characterized them in terms of elemental analysis, and simulated them for steam gasification at our reactor operating conditions to see how much hydrogen or syngas product could be obtained from such real feeds. We have stated that biomass conversion to liquid and gaseous fuels presents an attractive method for energy generation, with zero net CO_2 impact on the environment. Waste apple pomace (WAP), and waste banana peels (WBP) are widely available in large quantities especially in the urban areas where they are consumed on daily basis. These waste biomass materials could be utilized in clean hydrogen production. In addition, rice and millet husk are widely available in the tropical areas of the word, where they are mainly handled by incineration or composting.

Waste banana peels (WBP) and waste apple pomace (WAP) were obtained from KFUPM's student restaurant, while rice husk (RH) and Millet Husk (MH) were supplied from Nigeria.

7.5.1 Chemical analyses

The elemental composition of the selected biomass waste materials is presented in Table 7.5.

Table 7.5. Summary of elemental analysis of some selected biomass wastes.

Sample	Composition (CH_xO_y)	
	x	y
Waste banana peels (WBP)	0.200	1.735
Waste apple pomace (WAP)	0.209	1.520
Rice husk (RH)	0.087	1.698
Millet husk (MH)	0.095	1.806

Accordingly, we evaluated the extremum amounts of hydrogen that could be obtained from the above selected biomass waste materials in the subsection.

7.5.2 Temperature progression of equilibrium product composition

Figure 7.6 shows the simulation results of supercritical water gasification of WBP at typical operating conditions of the riser simulator. At 650 °C, hydrogen composition is about 25 mol%, while CO_2 reached up to about 73 mol%. The high amount of CO_2 suggests that water gas shift reaction is thermodynamically favored to enhance H_2 generation. Methanation reaction is negligible as indicated by the near zero amount of methane. Therefore, such reactions that favor the disappearance of methane (i.e. steam reforming of methane and dry reforming of methane) are favored by the thermodynamics of the process.

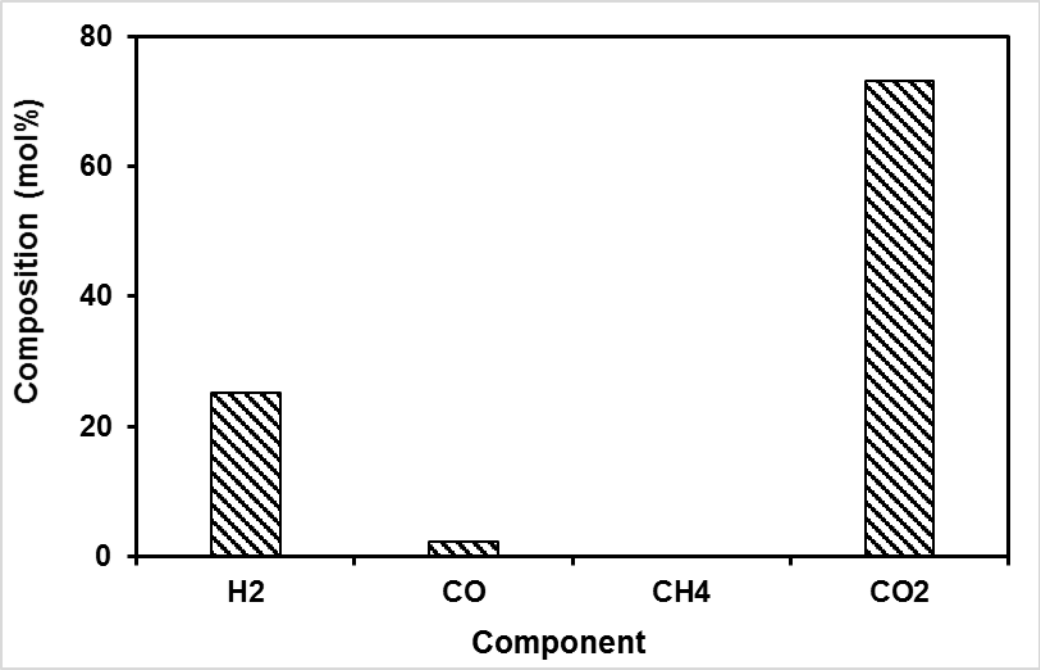

Figure 7.6: Thermodynamic product composition of steam gasification for WBP.

The equilibrium product composition for SCW gasification of millet husk over a range of temperature is illustrated in Figure 7.7.

Interestingly, millet husk which is known to contain a lot of indigestible wastes could be valorized in supercritical water conditions, giving a significant proportions of hydrogen (up to 18 mol%) and CO_2 (~ 80%) at 600 °C (See Figure 7.7). The equilibrium product composition gives a hint about the dominance of water gas shift reaction throughout the temperature range (400 – 700 °C), showing a maximum at 550 °C. Moreover, there is suppression of methane formation within same range of temperature.

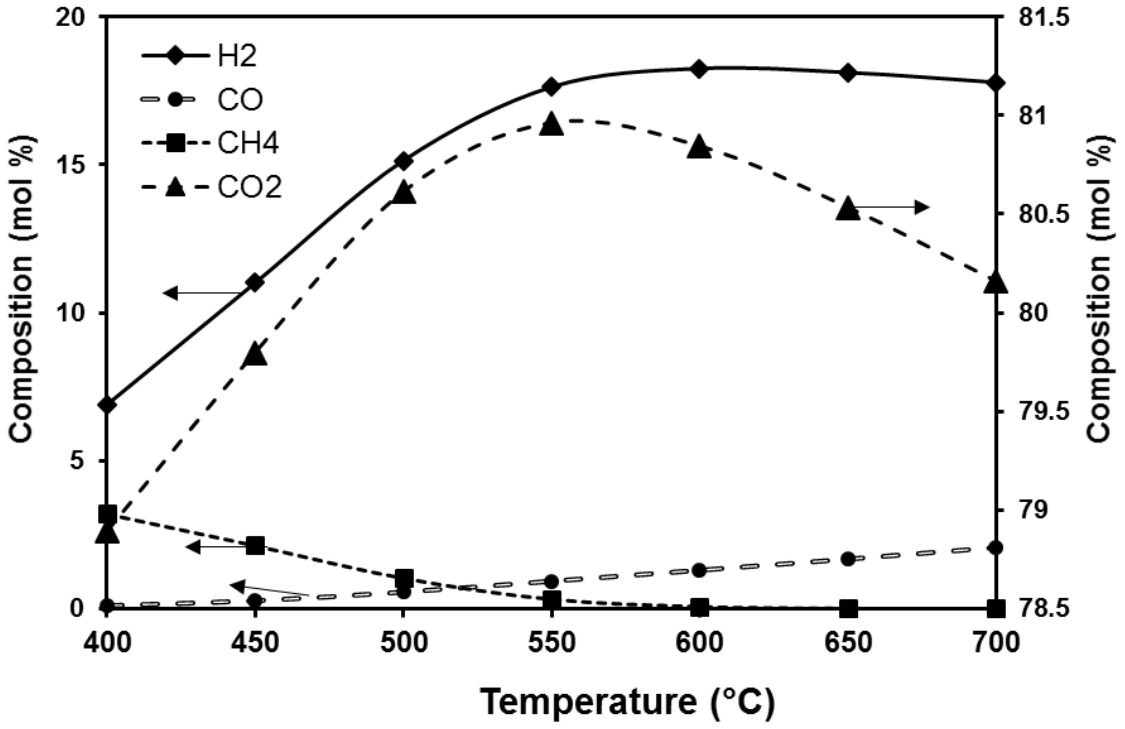

Figure 7.7: Equilibrium product composition for millet husk in SCW.

Figure 7.8 shows the equilibrium product composition of rice husk gasification. Rice husk gives methane-free products above 600 °C. At T > 550 °C, formation of CO is favored probably by Boudouard reaction, and with some contribution from steam gasification of carbon. Water gas shift may not be dominant above 650 °C as could be deduced from an almost flat hydrogen profile.

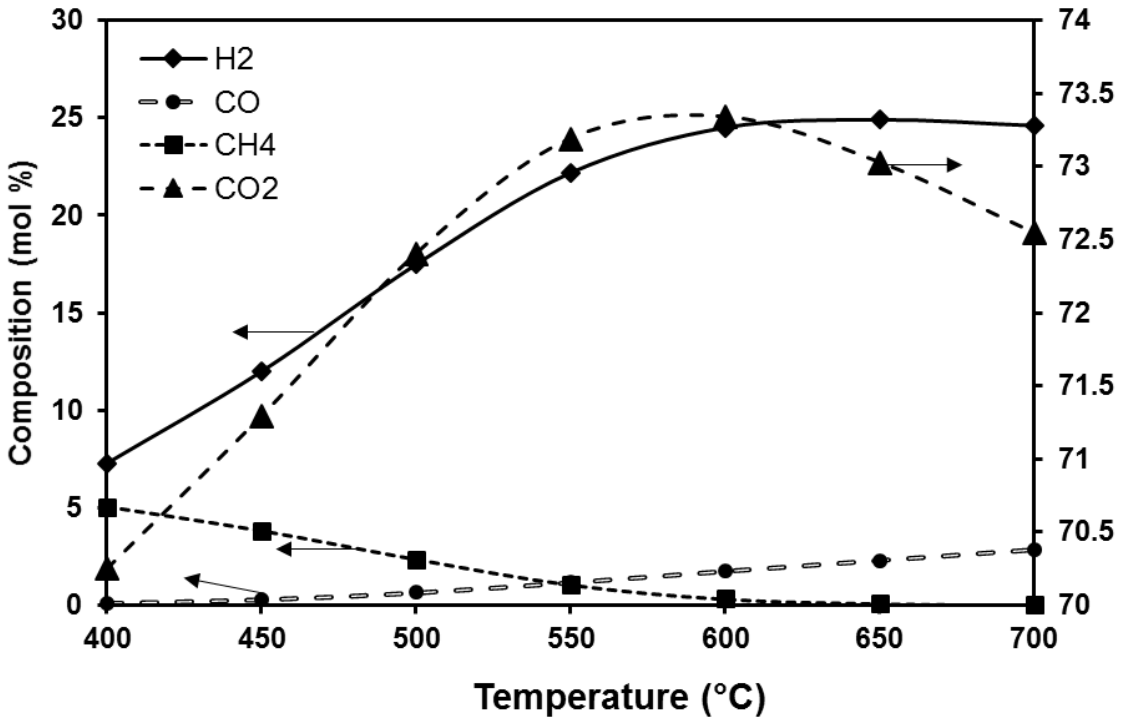

Figure 7.8: Equilibrium product composition for rice husk in SCW.

Figure 7.9 shows the equilibrium product composition for WAP gasification in supercritical water (P = 250 bar). The maximum of amount of CO_2 is about 62.5 mol%, which is less than the corresponding amounts in the three other biomass species. On the other hydrogen production reached up to 35 mol %. This means that Waste apple pomace is capable of undergoing a significant water gas reaction, steam gasification of carbon with moderate Boudouard reactions to maximize hydrogen yield, with lesser CO_2 content as compared to other biomass.

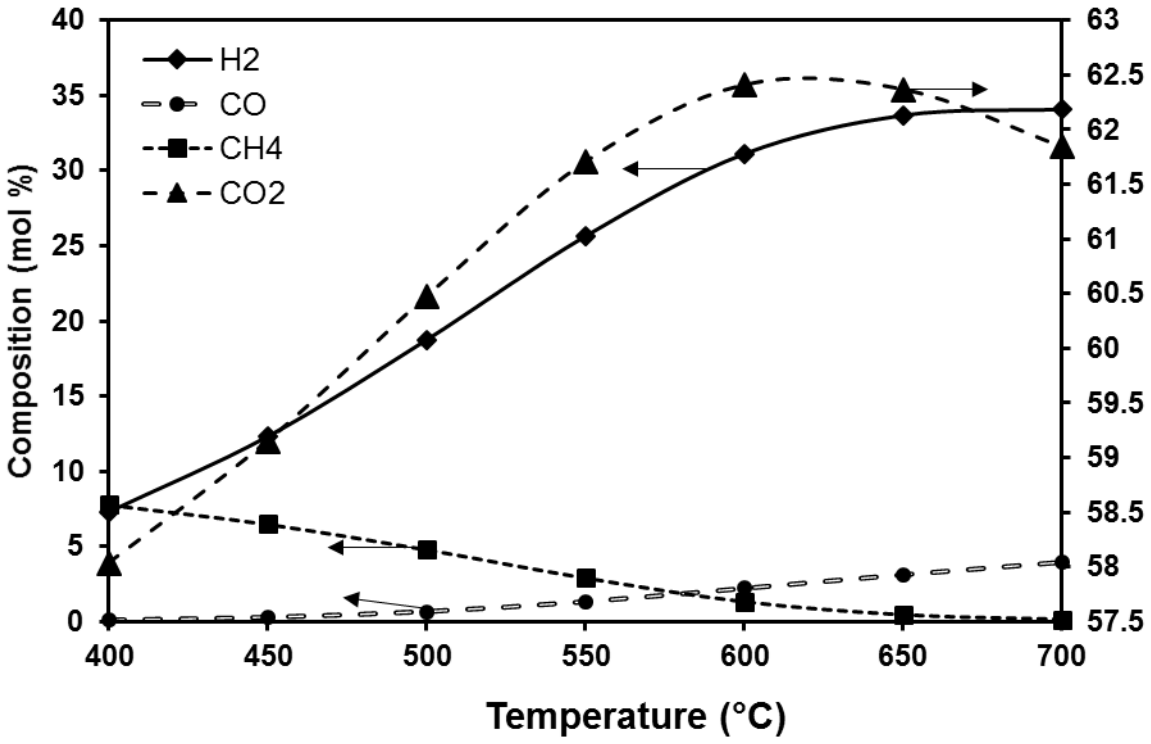

Figure 7.9: Equilibrium product composition for WAP gasification in SCW.

It should be noted in the above discussions that the relative amounts of permanent that could be generated from the waste biomass materials are strictly related to proportions of C:H:O in the biomass.

The thermodynamic studies can be summarized as follows. The thermodynamic model developed, turned out to be a rigorous one, capable of predicting the equilibrium product distribution for any real biomass (i.e., not just glucose). The accuracy of the formulated equilibrium model was tested and validated by comparing the simulated compressibility factor Z with that of a gas stream having the same composition at the same sets of operating conditions using Aspen-HYSYS process simulator. Syngas

production was favored by high temperatures, low pressure and a water to glucose ratio of about 9. Therefore there is room for catalyst design in order to suit any real biomass gasification in SCW, without undermining, the catalyst surface area, metal-support interaction, and/or overall catalysts activity.

CHAPTER 8

CONCLUSIONS AND RECOMMENDATIONS

8.1 Conclusions

Nickel based catalysts being capable of enhancing syngas production from gasification of biomass materials, have a potential large scale application in the conventional fluidized bed reactors. Therefore it is crucial to address the current challenges associated with the application of these catalyst from synthesis to application in a fluidized bed reactor. The present contribution focused on how to mitigate coking and enhance the structural and thermal stability of nickel-alumina based catalysts by doping ceria within the alumina matrix.

The following conclusions can be drawn from the synthesis of the novel Ce-doped-mesoporous alumina support:

i. The new methodology developed for doping ceria on alumina is highly effective in stabilizing γ-phase alumina up to 750 °C, without affecting its surface area.

ii. SEM and BET results indicate that ceria is well dispersed in the alumina phase. The presence of ceria and the synthesis methodology have helped in conserving the surface area of the Ce-Al_2O_3 support by minimizing excessive loss of bridged hydroxyl species.

iii. 1.0 wt. % ceria dopant in the Al_2O_3 matrix led to a network of mesopores having a pore size distribution that is suitable for biomass/tar cracking reactions.

iv. Bare alumina showed an activation energy (E_a) of ammonia desorption of 27.6 kJ/mol, whereas 1.0Ce-Al_2O_3 had E_a = 35.56 kJ/mol. This increase in E_a indicates some moderate Ce/Al_2O_3 interaction which will not impede reactants accessibility to the catalysts active sites.

As regards, the new Ni/Ce-meso-Al_2O_3 catalysts, the following important points should be stressed:

i. XRD patterns showed that nickel is well dispersed on the new Ce-Al_2O_3 surface. This stresses the success of our templated-free technique coupled with the successive incipient wetness impregnation method for loading nickel. The relatively sharper peaks obtained at 20 wt% nickel loading (i.e. Ni(20)/Ce-Al_2O_3) indicate a possible agglomeration at higher nickel loadings.

ii. The BET surface areas of the catalysts decreased from 152 to 104 m^2/g while the pore size was not affected significantly (97-90 Å) as determined via N_2 adsorption/desorption.

iii. The acidity of the catalysts as determined via NH_3 TPD decreased from 0.317 to 0.202 mmol NH_3/g-sample as the nickel loading was increased from 5 to 20 wt%. This is ascribed to coordination of Ni species with electron deficient Lewis acidic centers.

iv. Results of H_2 TPR indicate that nickel interacted moderately with the new ceria-doped alumina support, thereby suppressing any tendency to sintering while providing an acceptable amount of reducible species.

v. TGA profiles showed that the new ceria-doped alumina support is thermally stable and sufficient for low-temperature biomass thermochemical conversions. The thermograms of the spent catalysts showed that the extent of coking was generally low, the maximum being 0.092 g (Coke+Moisture)/g-catalyst for $Ni(5)/Al_2O_3$. An increase in nickel loading from 5 to 20 wt% further attenuated the extent of coking during the gasification process. This is ascribed to the increased carbon conversion efficiency resulting from the coordination of more nickel species with the electron deficient Lewis acidic centers of the alumina support.

vi. By considering two modes of catalyst regeneration, it was shown that the metallic Ni species is preferable for biomass gasification reaction than the oxidized counterpart (i.e. NiO), which must be reduced by $CO+H_2$ species generated from biomass pyrolysis in situ.

vii. A general factorial experimental design indicated that both catalyst regeneration mode and the injection number are significant in determining the percentage hydrogen composition in the gasification products. However, H_2/CO ratio was not affected significantly within the range of the experimental factors considered.

viii. A mixture of 12.5 wt% glucose + 2.5wt% toluene fed to the riser simulator operating at 1atm, 700 °C, 4000 rpm for 30 seconds, showed a product composition of 74.33 mol% H_2, 22.60 mol% COx and 3.06 mol% HC's (i.e. C_1, C_2 and $C_2^=$).

As regards the thermodynamic studies, the following are the main findings.

i. The equilibrium model was verified by comparing the values of the model's compressibility factor Z with that of a similar gas stream using Aspen-Hysys process simulator at the same sets of operating conditions (T, P).

ii. The thermodynamic model could be applied to predict the equilibrium product composition for any real biomass, as illustrated with rice husk, millet husk, waste banana peels, and waste apple pomace.

iii. For glucose gasification, syngas yield was favored at high temperatures, low pressure and a water/glucose ratio of ~9.

The following points should be stressed with respect to the detailed kinetic modeling of steam gasification of glucose over Ni/Ce-doped-Al_2O_3 was carried out under turbulent fluidized bed conditions.

i. Nickel(20)/Ce-meso-Al_2O_3 catalyst gave a better performance for a 15 wt% glucose in water at moderate temperatures (i.e. $550 \leq T \leq 700$ °C) in a CREC riser simulator. This catalyst, in particular, gave the highest amount of syngas without tempering with hydrogen proportion and showed a relatively lower extent of coking as compared to other catalysts (i.e Ni(5), Ni(10) or Ni(15) Ce-meso-Al_2O_3).

ii. Langmuir-Hinshelwood type of kinetic model was found to be appropriate to describe the kinetics of steam gasification of glucose over nickel(20)/Ce-meso-Al_2O_3. Glucose was pyrolyzed to permanent gases (i.e. CO, CO_2, CH_4, and H_2) which recombined via dominantly water gas shift, steam reforming of methane and reverse dry reforming of methane.

iii. A kinetic model of the Langmuir-Hinshelwood type satisfactorily fitted the experimental data obtained for a 15 wt% glucose in water fed to the riser at T = 550, 600, 650 and 700 C; t = 5, 10, 15, 20 and 25 s, with R^2 = 0.999 and AIC = -415.83. The intrinsic rate constants were determined as $k^0_{WGS} = 7.76x10^{-2}$; $k^0_{SRM} = 4.13x10^{-2}$; and $k^0_{RDRM} = 3.57x10^{-2}$ mmol/gcat.s.bar^2 with corresponding activation energies, $E_{WGS} = 20.0$ kJ/mol; $E_{SRM} = 4.20$ kJ/mol and $E_{WGS} = 7.90$ kJ/mol respectively. These intrinsic rate parameters have the same order of magnitude as those reported in the literature.

iv. The kinetic model could be used to predict the desired operating conditions (i.e. temperature and reaction time) for a target syngas composition from a similar feedstock in a similar reactor.

v. The modeling procedure could be applied to a different catalytic system in the same or similar reactor to obtain the necessary kinetic parameters.

8.2 Recommendations

The following are recommended for further studies in this area.

i. Other classes of lignocellulosic model compounds could be tested for gasification using the catalysts matrix synthesized in this work.

ii. The newly prepared support could be impregnated with other active metal species (e.g. rhodium, ruthenium), to compare their performance and stability in gasification environment with respect to nickel.

iii. The effect of the support type could be studied by comparing the catalysts in the current studies with other nickel-based catalysts on different supports, for the same similar reaction conditions.

iv. The role of support mesoporosity could be studied by comparing the activities obtained in the current studies with other systems having nickel supported on microporous supports.

v. The detailed thermodynamic model could be packaged into a software with a provision to add new species with their standard Gibbs' free energy values to suit any real system.

vi. The kinetic scheme developed could be tested for gasification products from other fluidized bed reactors. The model may be modified to accommodate some catalyst deactivation terms to take care of long-run continuous operations.

REFERENCES

[1] Drax, Biomass : the fourth energy source, (2011).

[2] M. Balat, G. Ayar, Biomass energy in the world, use of biomass and potential trends, Energy Sources. 27 (2005) 931–940. doi:10.1080/00908310490449045.

[3] A.-S. Nizami, Recycling and Waste-to-Energy Prospects in Saudi Arabia, BioEnergy Consult. (2015). http://www.bioenergyconsult.com/tag/saudi-arabia/.

[4] A.S.M.J.I. Mazumder, Steam Gasification of Biomass Surrogates: Catalyst Development and Kinetic Modelling, Western Ontario, 2014. doi:http://ir.lib.uwo.ca/etd/2014/.

[5] H. De Lasa, E. Salaices, J. Mazumder, R. Lucky, Catalytic steam gasification of biomass: Catalysts, thermodynamics and kinetics, Chem. Rev. 111 (2011) 5404–5433. doi:10.1021/cr200024w.

[6] S. Adhikari, S. Fernando, A. Haryanto, A Comparative Thermodynamic and Experimental Analysis on Hydrogen Production by Steam Reforming of Glycerin, Energy & Fuels. 21 (2007) 2306–2310. doi:10.1021/ef0700351.

[7] J. Mazumder, H. de Lasa, Fluidizable Ni/La2O3-γAl2O3 catalyst for steam gasification of a cellulosic biomass surrogate, Appl. Catal. B Environ. 160–161 (2014) 67–79. doi:10.1016/j.apcatb.2014.04.042.

[8] J.A.M. Withag, On the gasification of wet biomass in supercritical water : over de vergassing van natte biomassa in superkritiek water, 2013.

[9] Y. Lu, L. Guo, X. Zhang, C. Ji, Hydrogen production by supercritical water gasification of biomass: Explore the way to maximum hydrogen yield and high carbon gasification efficiency, Int. J. Hydrogen Energy. 37 (2012) 3177–3185. doi:10.1016/j.ijhydene.2011.11.064.

[10] L. Zhao, J. Zhang, C.D. Sheng, K. Wang, Q.Z. Ding, Dissolution Characteristics of Inorganic Elements Existing in Biomass during the Supercritical Water Gasification Process, Energy Sources, Part A Recover. Util. Environ. Eff. 34 (2012) 1893–1900. doi:10.1080/15567036.2011.592913.

[11] D. Yu, M. Aihara, M.J. Antal, Hydrogen Production by Steam Reforming Glucose in Supercritical Water?, (1993) 574–577.

[12] Q. Yan, L. Guo, Y. Lu, Thermodynamic analysis of hydrogen production from biomass gasification in supercritical water, Energy Convers. Manag. 47 (2006) 1515–1528. doi:10.1016/j.enconman.2005.08.004.

[13] J.Chu et al 1995.pdf, (n.d.).

[14] X.H. Hao, L.J. Guo, X. Mao, X.M. Zhang, X.J. Chen, Hydrogen production from glucose used as a model compound of biomass gasified in supercritical water, Int. J. Hydrogen Energy. 28 (2003) 55–64. doi:10.1016/S0360-3199(02)00056-3.

[15] Xiadong Xu and Michael Jerry Antal Jr., Gasification of sewage sludge and other biomass for hydrogen production in supercritical water, Environ. Prog. Sustain. Eng. 17 (2006) 215–220.

[16] S. Letellier, F. Marias, P. Cezac, J.P. Serin, R.J. Ferry, P.A.U. Cedex, A thermodynamic equilibrium study of Supercritical Water Gasification of Glucose, (2008) 1–5.

[17] S. Begum, M.G. Rasul, D. Akbar, D. Cork, An Experimental and Numerical Investigation of Fluidized Bed Gasification of Solid Waste, Energies. 7 (2014) 43–61. doi:10.3390/en7010043.

[18] Y. Lu, S. Li, L. Guo, X. Zhang, Hydrogen production by biomass gasification in supercritical water over Ni/γAl2O3 and Ni/CeO2-γAl2O3 catalysts, Int. J. Hydrogen Energy. 35 (2010) 7161–7168. doi:10.1016/j.ijhydene.2009.12.047.

[19] P. Kaushal, T. Proell, H. Hofbauer, Application of a detailed mathematical model to the gasifier unit of the dual fluidized bed gasification plant, Biomass and Bioenergy. 35 (2011) 2491–2498. doi:10.1016/j.biombioe.2011.01.025.

[20] Q. Xue, R.O. Fox, Multi-fluid CFD modeling of biomass gasification in polydisperse fluidized-bed gasifiers, Powder Technol. 254 (2014) 187–198. doi:10.1016/j.powtec.2014.01.025.

[21] O. Yakaboylu, G. Yapar, M. Recalde, J. Harinck, K.G. Smit, E. Martelli, et al., Supercritical Water Gasification of Biomass: An Integrated Kinetic Model for the Prediction of Product Compounds, Ind. Eng. Chem. Res. 54 (2015) 8100–8112. doi:10.1021/acs.iecr.5b02019.

[22] R.-X. Yang, K.-H. Chuang, M.-Y. Wey, Effects of Nickel Species on Ni/Al 2 O 3 Catalysts in Carbon Nanotube and Hydrogen Production by Waste Plastic Gasification: Bench- and Pilot-Scale Tests, Energy & Fuels. 29 (2015) 8178–8187. doi:10.1021/acs.energyfuels.5b01866.

[23] C. Wu, P.T. Williams, A Novel Nano-Ni / SiO 2 Catalyst for Hydrogen Production from Steam Reforming of Ethanol, Environ. Sci. Technol. (2010) 5993–5998.

[24] N.Ü. Cengiz, G. Yıldız, M. Sert, D. Selvi Gökkaya, M. Sağlam, M. Yüksel, et al., Hydrothermal gasification of a biodiesel by-product crude glycerol in the presence of phosphate based catalysts, Int. J. Hydrogen Energy. 40 (2015) 14806–14815. doi:10.1016/j.ijhydene.2015.08.097.

[25] V.G. Deshmane, S.L. Owen, R.Y. Abrokwah, D. Kuila, Mesoporous nanocrystalline TiO2 supported metal (Cu, Co, Ni, Pd, Zn, and Sn) catalysts:

Effect of metal-support interactions on steam reforming of methanol, J. Mol. Catal. A Chem. 408 (2015) 202–213. doi:10.1016/j.molcata.2015.07.023.

[26] L. Zhang, P. Champagne, C. Xu, Screening of supported transition metal catalysts for hydrogen production from glucose via catalytic supercritical water gasification, Int. J. Hydrogen Energy. 36 (2011) 9591–9601. doi:10.1016/j.ijhydene.2011.05.077.

[27] P.A. Manzour, Hydrogen Production Using Catalytic Supercritical Water Gasification of Lignocellulosic Biomass, 2012.

[28] S. Nanda, S.N. Reddy, H.N. Hunter, I.S. Butler, J.A. Kozinski, Supercritical Water Gasification of Lactose as a Model Compound for Valorization of Dairy Industry Effluents, Ind. Eng. Chem. Res. 54 (2015) 9296–9306. doi:10.1021/acs.iecr.5b02603.

[29] O. Yakaboylu, J. Harinck, K.G. Smit, W. de Jong, Supercritical Water Gasification of Biomass: A Detailed Process Modeling Analysis for a Microalgae Gasification Process, Ind. Eng. Chem. Res. 54 (2015) 5550–5562. doi:10.1021/acs.iecr.5b00942.

[30] C. Wu Chunfei, L. Wang Leizhi, P.T. Williams, J. Shi Jeffrey, J. Huang, Hydrogen production from biomass gasification with Ni/MCM-41 catalysts: Influence of Ni content, Appl. Catal. B Environ. 108–109 (2011) 6–13. doi:10.1016/j.apcatb.2011.07.023.

[31] P. Lv, J. Chang, T. Wang, Y. Fu, Y. Chen, J. Zhu, Hydrogen-rich gas production from biomass catalytic gasification, Energy and Fuels. 18 (2004) 228–233. doi:10.1021/ef0301203.

[32] M. Inaba, K. Murata, M. Saito, I. Takahara, Hydrogen production by gasification of cellulose over Ni catalysts supported on zeolites, Energy and Fuels. 20 (2006) 432–438. doi:10.1021/ef050283m.

[33] N. Boukis, U. Galla, H. Müller, E. Dinjus, Biomass gasification in supercritical water. Experimental progress achieved with the Verena pilot plant., 15th Eur. Biomass Conf. Exhib. 7-11 May 2007, Berlin, Ger. (2007) 1013–1016.

[34] D.M. Alonso, S.G. Wettstein, J.A. Dumesic, D.M. Alonso, G. Wettstein, J.A. Dumesic, Chem Soc Rev Bimetallic catalysts for upgrading of biomass to fuels and chemicals w, 41 (2012). doi:10.1039/c2cs35188a.

[35] S. Adhikari, S.D. Fernando, A. Haryanto, Hydrogen production from glycerin by steam reforming over nickel catalysts, Renew. Energy. 33 (2008) 1097–1100. doi:10.1016/j.renene.2007.09.005.

[36] G.J. DiLeo, M.E. Neff, S. Kim, P.E. Savage, Supercritical water gasification of phenol and glycine as models for plant and protein biomass, Energy and Fuels. 22 (2008) 871–877. doi:10.1021/ef700497d.

[37] R.F. Susanti, L.W. Dianningrum, T. Yum, Y. Kim, B.G. Lee, J. Kim, High-yield hydrogen production from glucose by supercritical water gasification without added catalyst, Int. J. Hydrogen Energy. 37 (2012) 11677–11690. doi:10.1016/j.ijhydene.2012.05.087.

[38] D. Castello, A. Kruse, L. Fiori, ScienceDirect Low temperature supercritical water gasification of biomass constituents : Glucose / phenol mixtures, Biomass and Bioenergy. 73 (2014) 84–94. doi:10.1016/j.biombioe.2014.12.010.

[39] I. Lee, Effect of metal addition to Ni / activated charcoal catalyst on gasification of glucose in supercritical water, 6 (2011). doi:10.1016/j.ijhydene.2011.05.008.

[40] M.B.I. Chowdhury, M.M. Hossain, P.A. Charpentier, Effect of supercritical water gasification treatment on Ni/La2O3-Al2O3-based catalysts, Appl. Catal. A Gen. 405 (2011) 84–92. doi:10.1016/j.apcata.2011.07.031.

[41] C. Zhu, L. Guo, H. Jin, J. Huang, S. Li, X. Lian, Effects of reaction time and catalyst on gasification of glucose in supercritical water: Detailed reaction pathway and mechanisms, Int. J. Hydrogen Energy. 41 (2016) 6630–6639. doi:10.1016/j.ijhydene.2016.03.035.

[42] D. Świerczyński, S. Libs, C. Courson, a. Kiennemann, Steam reforming of tar from a biomass gasification process over Ni/olivine catalyst using toluene as a model compound, Appl. Catal. B Environ. 74 (2007) 211–222. doi:10.1016/j.apcatb.2007.01.017.

[43] J. Tao, L. Zhao, C. Dong, Q. Lu, X. Du, E. Dahlquist, Catalytic Steam Reforming of Toluene as a Model Compound of Biomass Gasification Tar Using Ni-CeO2/SBA-15 Catalysts, Energies. 6 (2013) 3284–3296. doi:10.3390/en6073284.

[44] F. Rossi, A. Nicolini, Ethanol reforming for supplying molten carbonate fuel cells, Int. J. Low-Carbon Technol. 8 (2012) 140–145. doi:10.1093/ijlct/cts057.

[45] H.T. Nguyen, E. Yoda, M. Komiyama, Catalytic supercritical water gasification of proteinaceous biomass: Catalyst performances in gasification of ethanol fermentation stillage with batch and flow reactors, Chem. Eng. Sci. 109 (2014) 197–203. doi:10.1016/j.ces.2014.01.036.

[46] S. Therdthianwong, N. Srisiriwat, A. Therdthianwong, E. Croiset, Hydrogen production from bioethanol reforming in supercritical water, J. Supercrit. Fluids. 57 (2011) 58–65. doi:10.1016/j.supflu.2011.02.005.

[47] O. Yakaboylu, J. Harinck, K. Smit, W. de Jong, Supercritical Water Gasification of Biomass: A Literature and Technology Overview, Energies. 8 (2015) 859–894. doi:10.3390/en8020859.

[48] A. Chuntanapum, Y. Matsumura, Char Formation Mechanism in Supercritical Water Gasification Process: A Study of Model Compounds, Ind. Eng. Chem. Res. 49 (2010) 4055–4062. doi:10.1021/ie901346h.

[49] A.K. Goodwin, G.L. Rorrer, Reaction rates for supercritical water gasification of xylose in a micro-tubular reactor, Chem. Eng. J. 163 (2010) 10–21. doi:10.1016/j.cej.2010.07.013.

[50] Z. FANG, Catalytic hydrothermal gasification of cellulose and glucose, Int. J. Hydrogen Energy. 33 (2008) 981–990. doi:10.1016/j.ijhydene.2007.11.023.

[51] I.-G. Lee, M.-S. Kim, S.-K. Ihm, Gasification of glucose in supercritical water, Ind. Eng. Chem. Res. 41 (2002).

[52] J. Mazumder, H.I. de Lasa, Fluidizable La2O3 promoted Ni/γ-Al2O3 catalyst for steam gasification of biomass: Effect of catalyst preparation conditions, Appl. Catal. B Environ. 168 (2015) 250–265. doi:10.1016/j.apcatb.2014.12.009.

[53] L. Atanda, M. Konarova, Q. Ma, S. Mukundan, A. Shrotri, J. Beltramini, High yield conversion of cellulosic biomass into 5-hydroxymethylfurfural and a study of the reaction kinetics of cellulose to HMF conversion in a biphasic system, Catal. Sci. Technol. 6 (2016) 6257–6266. doi:10.1039/C6CY00820H.

[54] L. Wang, Z. Zhang, L. Zhang, S. Xue, W.O.S. Doherty, I.M. O'Hara, et al., Sustainable conversion of cellulosic biomass to chemicals under visible-light irradiation, RSC Adv. 5 (2015) 85242–85247. doi:10.1039/C5RA16616K.

[55] M.B.I. Chowdhury, Nickel-based Catalysts for Gasification of Glucose in Supercritical Water ., (2010).

[56] T. Yanagida, T. Minowa, A. Nakamura, Y. Matsumura, Y. Noda, Behavior of inorganic elements in poultry manure during supercritical water gasification, Nihon Enerugi Gakkaishi/Journal Japan Inst. Energy. 87 (2008) 731–736. doi:10.3775/jie.87.731.

[57] M.H. Waldner, F. Vogel, Renewable production of methane from woody biomass by catalytic hydrothermal gasification, Ind. Eng. Chem. Res. 44 (2005) 4543–4551. doi:10.1021/ie050161h.

[58] A.J. Byrd, K.K. Pant, R.B. Gupta, Hydrogen production from glycerol by reforming in supercritical water over Ru/Al2O3 catalyst, Fuel. 87 (2008) 2956–2960. doi:10.1016/j.fuel.2008.04.024.

[59] F.L. Chan, A. Tanksale, Review of recent developments in Ni-based catalysts for biomass gasification, Renew. Sustain. Energy Rev. 38 (2014) 428–438. doi:10.1016/j.rser.2014.06.011.

[60] N.D. Charisiou, G. Siakavelas, K.N. Papageridis, A. Baklavaridis, L. Tzounis, D.G. Avraam, et al., Syngas production via the biogas dry reforming reaction over nickel supported on modified with CeO2 and/or La2O3 alumina catalysts, J. Nat. Gas Sci. Eng. 31 (2016) 164–183. doi:10.1016/j.jngse.2016.02.021.

[61] P. Osorio-Vargas, N.A. Flores-González, R.M. Navarro, J.L.G. Fierro, C.H. Campos, P. Reyes, Improved stability of Ni/Al2O3 catalysts by effect of promoters

(La2O3, CeO2) for ethanol steam-reforming reaction, Catal. Today. 259 (2016). doi:10.1016/j.cattod.2015.04.037.

[62] P. Chaiprasert, T. Vitidsant, Effects of promoters on biomass gasification using nickel/dolomite catalyst, Korean J. Chem. Eng. 26 (2009) 1545–1549. doi:10.1007/s11814-009-0259-7.

[63] J. Nishikawa, K. Nakamura, M. Asadullah, T. Miyazawa, K. Kunimori, K. Tomishige, Catalytic performance of Ni/CeO2/Al2O3 modified with noble metals in steam gasification of biomass, Catal. Today. 131 (2008) 146–155. doi:10.1016/j.cattod.2007.10.066.

[64] C.E. Efika, C. Wu, P.T. Williams, Syngas production from pyrolysis-catalytic steam reforming of waste biomass in a continuous screw kiln reactor, J. Anal. Appl. Pyrolysis. 95 (2012) 87–94. doi:10.1016/j.jaap.2012.01.010.

[65] J. Srinakruang, K. Sato, T. Vitidsant, K. Fujimoto, Highly efficient sulfur and coking resistance catalysts for tar gasification with steam, Fuel. 85 (2006) 2419–2426. doi:10.1016/j.fuel.2006.04.026.

[66] E.P. Barrett, L.G. Joyner, P.P. Halenda, The Determination of Pore Volume and Area Distributions in Porous Substances. I. Computations from Nitrogen Isotherms, J. Am. Chem. Soc. 73 (1951) 373–380. doi:10.1021/ja01145a126.

[67] D. Dollimore, G.R. Heal, An improved method for the calculation of pore size distribution from adsorption data, J. Appl. Chem. 14 (2007) 109–114. doi:10.1002/jctb.5010140302.

[68] K. Szczodrowski, B. Prélot, S. Lantenois, J.M. Douillard, J. Zajac, Effect of heteroatom doping on surface acidity and hydrophilicity of Al, Ti, Zr-doped mesoporous SBA-15, Microporous Mesoporous Mater. 124 (2009) 84–93. doi:10.1016/j.micromeso.2009.04.035.

[69] A. Le Valant, N. Bion, F. Can, D. Duprez, F. Epron, Preparation and characterization of bimetallic Rh-Ni/Y2O3-Al2O3 for hydrogen production by raw bioethanol steam reforming: influence of the addition of nickel on the catalyst performances and stability, Appl. Catal. B Environ. 97 (2010) 72–81. doi:10.1016/j.apcatb.2010.03.025.

[70] G. Lefèvre, M. Duc, P. Lepeut, R. Caplain, M. Fédoroff, Hydration of γ-alumina in water and its effects on surface reactivity, Langmuir. 18 (2002) 7530–7537. doi:10.1021/la025651i.

[71] S.J. Smith, S. Amin, B.F. Woodfield, J. Boerio-Goates, B.J. Campbell, Phase progression of γ-Al2O3 nanoparticles synthesized in a solvent-deficient environment, Inorg. Chem. 52 (2013) 4411–4423. doi:10.1021/ic302593f.

[72] K. Wefers, C. Misra, Oxides and Hydroxides of Aluminum, Alcoa Tech. Pap. 19 (1987) 1–100.

[73] H. Xiong, H.N. Pham, A.K. Datye, Hydrothermally stable heterogeneous catalysts for conversion of biorenewables, Green Chem. 16 (2014) 4627–4643. doi:10.1039/c4gc01152j.

[74] K.S.W. Sing, Reporting physisorption data for gas/solid systems with special reference to the determination of surface area and porosity (Recommendations 1984), Pure Appl. Chem. 57 (1985). doi:10.1351/pac198557040603.

[75] S. Lowell, J.E. Shields, M.A. Thomas, M. Thommes, Characterization of Porous Solids and Powders: Surface Area, Pore Size and Density, Springer Netherlands, Dordrecht, 2004. doi:10.1007/978-1-4020-2303-3.

[76] C.J. Lucio-ortiz, Preparation and Characterization of Cu and Ni on Alumina Supports and Their Use in the Synthesis of Low-Temperature Metal-Phthalocyanine Using a Parallel-Plate Reactor, (2013) 4324–4344. doi:10.3390/ma6104324.

[77] M.M. Hossain, D. Lopez, J. Herrera, H.I. de Lasa, Nickel on lanthanum-modified γ-Al2O3 oxygen carrier for CLC: Reactivity and stability, Catal. Today. 143 (2009) 179–186. doi:10.1016/j.cattod.2008.09.006.

[78] N. Al-Yassir, R. Le Van Mao, Evaluating and understanding the hydrothermal stability of alumina aerogel doped with yttrium oxide and used as a catalyst support for the thermo-catalytic cracking (TCC) process, Can. J. Chem. 86 (2008) 146–160.

[79] F. Sánchez-De la Torre, J. De la Rosa, B. Kharisov, C. Lucio-Ortiz, Preparation and Characterization of Cu and Ni on Alumina Supports and Their Use in the Synthesis of Low-Temperature Metal-Phthalocyanine Using a Parallel-Plate Reactor, Materials (Basel). 6 (2013) 4324–4344. doi:10.3390/ma6104324.

[80] C.M.A. Parlett, K. Wilson, A.F. Lee, Hierarchical porous materials: catalytic applications, Chem. Soc. Rev. 42 (2013) 3876–3893. doi:10.1039/C2CS35378D.

[81] S. Tsuchiya, Y. Amenomiya, R.J. Cvetanović, Study of metal catalysts by temperature programmed desorption: III. Hydrogen-deuterium exchange on platinum, J. Catal. 20 (1971) 1–9. doi:10.1016/0021-9517(71)90002-9.

[82] R.J. Cvetanović, Y. Amenomiya, Application of a Temperature-Programmed Desorption Technique to Catalyst Studies, Adv. Catal. 17 (1967) 103–149. doi:10.1016/S0360-0564(08)60686-0.

[83] G. Tonetto, J. Atias, H. De Lasa, FCC catalysts with different zeolite crystallite sizes: Acidity, structural properties and reactivity, Appl. Catal. A Gen. 270 (2004) 9–25. doi:10.1016/j.apcata.2004.03.042.

[84] S. Al-Ghamdi, M. Volpe, M.M. Hossain, H. de Lasa, VOx/c-Al2O3 catalyst for oxidative dehydrogenation of ethane to ethylene: Desorption kinetics and catalytic activity, Appl. Catal. A Gen. 450 (2013) 120–130.

doi:10.1016/j.apcata.2012.10.007.

[85] A. Ayandiran, idris A. Bakare, H. Binous, S. Al-Ghamdi, S. Razzak, M.M. Hossain, Oxidative dehydrogenation of propane to propylene over VOx/CaO-γAl2O3 using lattice oxygen, Catal. Sci. Technol. (2016). doi:10.1039/C6CY00078A.

[86] M.G. White, Heterogeneous catalysis, Prentice Hall, New Jersey, 1990.

[87] I.A. Bakare, S.A. Mohamed, S. Al-Ghamdi, S.A. Razzak, M.M. Hossain, H.I. De Lasa, Fluidized bed ODH of ethane to ethylene over VOx-MoOx/γ-Al2O3 catalyst: Desorption kinetics and catalytic activity, Chem. Eng. J. 278 (2014) 207–216. doi:10.1016/j.cej.2014.09.114.

[88] J. Tian, J. Lu, Preparation and properties of nanophase (Ce, Zr, Pr)O 2-doped alumina coating on cordierite ceramic honeycomb for three-way catalysts, Brazilian J. Chem. Eng. 29 (2012) 121–133.

[89] M.R. Quddus, M.M. Hossain, H.I. de Lasa, Ni based oxygen carrier over γ-Al2O3 for chemical looping combustion: Effect of preparation method on metal support interaction, Catal. Today. 210 (2013) 124–134. doi:10.1016/j.cattod.2013.02.005.

[90] S.A. Ganiyu, K. Alhooshani, S.A. Ali, Single-pot synthesis of Ti-SBA-15-NiMo hydrodesulfurization catalysts: Role of calcination temperature on dispersion and activity, Appl. Catal. B Environ. 203 (2017) 428–441. doi:10.1016/j.apcatb.2016.10.052.

[91] I.E. Wachs, C.A. Roberts, Monitoring surface metal oxide catalytic active sites with Raman spectroscopy, Chem Soc Rev. 39 (2010) 5002–5017. doi:10.1039/c0cs00145g.

[92] A. Mitra, M.K. Mishra, J. Saha, G. De, Design of mesoporous alumina–ceria films on glass: Compositional tuning leads to mesoscopic transformations, Microporous Mesoporous Mater. 203 (2015) 151–162. doi:10.1016/j.micromeso.2014.10.014.

[93] S.S. Chan, I.E. Wachs, ln Situ Laser Raman Spectroscopy of Nickel Oxide Supported on y-Al203, J. Catal. 103 (1987) 224–227. doi:10.1016/0021-9517(87)90112-6.

[94] J. Mazumder, H. de Lasa, Fluidizable Ni/La2O3-γAl2O3 catalyst for steam gasification of a cellulosic biomass surrogate, Appl. Catal. B Environ. 160 (2014) 67–79. doi:10.1016/j.apcatb.2014.04.042.

[95] J.T. Richardson, B. Turk, M. V. Twigg, Reduction of model steam reforming catalysts" effect of oxide additives, Appl. Catal. A Gen. 148 (1996) 97–112. doi:10.1016/S0926-860X(96)00225-6.

[96] K. Djebaili, Z. Mekhalif, A. Boumaza, A. Djelloul, XPS , FTIR , EDX , and XRD Analysis of Al2O3 Scales Grown on PM2000 Alloy, 2015 (2015).

[97] V. La Parola, G. Deganello, S. Scirè, A.M. Venezia, Effect of the Al/Si atomic ratio on surface and structural properties of sol-gel prepared aluminosilicates, J. Solid State Chem. 174 (2003) 482–488. doi:10.1016/S0022-4596(03)00321-9.

[98] C. Morterra, G. Magnacca, A case study: surface chemistry and surface structure of catalytic aluminas, as studied by vibrational spectroscopy of adsorbed species, Catal. Today. 27 (1996) 497–532. doi:10.1016/0920-5861(95)00163-8.

[99] A.A. Khaleel, K.J. Klabunde, Characterization of aerogel prepared high-surface-area alumina: In situ FTIR study of dehydroxylation and pyridine adsorption, Chem. - A Eur. J. 8 (2002) 3991–3998. doi:10.1002/1521-3765(20020902)8:17<3991::AID-CHEM3991>3.0.CO;2-X.

[100] E. Parry, An infrared study of pyridine adsorbed on acidic solids. Characterization of surface acidity, J. Catal. 2 (1963) 371–379. doi:10.1016/0021-9517(63)90102-7.

[101] S. Adamu, M.Y. Khan, S.A. Razzak, M.M. Hossain, Ceria-stabilized meso-Al2O3: synthesis, characterization and desorption kinetics, J. Porous Mater. 24 (2017) 1343–1352. doi:10.1007/s10934-017-0376-3.

[102] Y. Richardson, J. Motuzas, A. Julbe, G. Volle, J. Blin, Catalytic investigation of in situ generated Ni metal nanoparticles for tar conversion during biomass pyrolysis, J. Phys. Chem. C. 117 (2013) 23812–23831. doi:10.1021/jp408191p.

[103] H. Schmieder, J. Abeln, N. Boukis, E. Dinjus, A. Kruse, M. Kluth, et al., Hydrothermal gasification of biomass and organic wastes, J. Supercrit. Fluids. 17 (2000) 145–153.

[104] S. Ali, A. Kruse, J. Rathert, Influence of the Heating Rate and the Type of Catalyst on the Formation of Key Intermediates and on the Generation of Gases During Hydropyrolysis of Glucose in Supercritical Water in a Batch, Ind. Eng. Chem. Res. 43 (2004) 502–508.

[105] A.J. Byrd, K.K. Pant, R.B. Gupta, Hydrogen Production from Glucose Using Ru/Al2O3 Catalyst in Supercritical Water, Ind. Eng. Chem. Res. 46 (2007) 3574–3579.

[106] H. Jin, Y. Lu, L. Guo, C. Cao, X. Zhang, Hydrogen production by partial oxidative gasification of biomass and its model compounds in supercritical water, Int. J. Hydrogen Energy. 35 (2010) 3001–3010. doi:10.1016/j.ijhydene.2009.06.059.

[107] R.F. Susanti, L.W. Dianningrum, T. Yum, Y. Kim, Y.W. Lee, J. Kim, High-yield hydrogen production by supercritical water gasification of various feedstocks: Alcohols, glucose, glycerol and long-chain alkanes, Chem. Eng. Res. Des. 92 (2014) 1834–1844. doi:10.1016/j.cherd.2014.01.003.

[108] J. Huang, X. Lian, L. Wang, C. Zhu, H. Jin, R. Wang, Hydrogen production from glucose by supercritical water gasification with Ni/Zr(Ce,Y)O2-δ catalysts, Int. J. Hydrogen Energy. (2016) 1–13. doi:10.1016/j.ijhydene.2016.10.012.

[109] H. Binous, A. Aheed, M.M. Hossain, Haber process and steam-coal gasification: Two standard thermodynamic problems elucidated using two distinct approaches, Comput. Appl. Eng. Educ. 24 (2016) 58–70. doi:10.1002/cae.21672.

[110] M.J. Gurka, L.J. Edwards, K.E. Muller, L.L. Kupper, Extending the Box-Cox transformation to the linear mixed model, J. R. Stat. Soc. Ser. A Stat. Soc. 169 (2006) 273–288. doi:10.1111/j.1467-985X.2005.00391.x.

[111] M. Peymani, S.M. Alavi, M. Rezaei, Synthesis gas production by catalytic partial oxidation of methane, ethane and propane on mesoporous nanocrystalline Ni/Al2O3 catalysts, Int. J. Hydrogen Energy. 41 (2016) 19057–19069. doi:10.1016/j.ijhydene.2016.07.072.

[112] K.Y. Koo, S. Lee, U.H. Jung, H. Roh, W.L. Yoon, Syngas production via combined steam and carbon dioxide reforming of methane over Ni–Ce/MgAl2O4 catalysts with enhanced coke resistance, Fuel Process. Technol. 119 (2014) 151–157. doi:10.1016/j.fuproc.2013.11.005.

[113] A.I. Tsyganok, T. Tsunoda, S. Hamakawa, K. Suzuki, K. Takehira, T. Hayakawa, Dry reforming of methane over catalysts derived from nickel-containing Mg-Al layered double hydroxides, J. Catal. 213 (2003) 191–203. doi:10.1016/S0021-9517(02)00047-7.

[114] S.O. Choi, I.Y. Ahn, S.H. Moon, Effect of CeO2-addition sequence on the performance of CeO2-modified Ni/Al2O3 catalyst in autothermal reforming of iso-octane, Korean J. Chem. Eng. 26 (2009) 1252–1258. doi:10.1007/s11814-009-0227-2.

[115] M. Argyle, C. Bartholomew, Heterogeneous Catalyst Deactivation and Regeneration: A Review, Catalysts. 5 (2015) 145–269. doi:10.3390/catal5010145.

[116] P. Azadi, E. Afif, F. Azadi, R. Farnood, Screening of nickel catalysts for selective hydrogen production using supercritical water gasification of glucose, Green Chem. 14 (2012) 1766. doi:10.1039/c2gc16378k.

[117] K. V. Manukyan, A. Avetisyan, C. Shuck, H. Chatilyan, S. Rouvimov, S. Kharatyan, et al., Nickel Oxide Reduction by Hydrogen: Kinetics and Structural Transformations, J. Phys. Chem. C. (2015) 150622173834003. doi:10.1021/acs.jpcc.5b04313.

[118] F.L. Chan, A. Tanksale, Review of recent developments in Ni-based catalysts for biomass gasification, Renew. Sustain. Energy Rev. 38 (2014) 428–438. doi:10.1016/j.rser.2014.06.011.

[119] G. Guan, M. Kaewpanha, X. Hao, A. Abudula, Catalytic steam reforming of biomass tar: Prospects and challenges, Renew. Sustain. Energy Rev. 58 (2016) 450–461. doi:10.1016/j.rser.2015.12.316.

[120] A.K.P. Mann, Z. Wu, S.H. Overbury, The Characterization and Structure-

Dependent Catalysis of Ceria with Well-Defined Facets, in: Catal. by Mater. with Well-Defined Struct., Elsevier Inc., 2015: pp. 71–97.

[121] B.C. Miranda, R.J. Chimentão, J.B.O. Santos, F. Gispert-Guirado, J. Llorca, F. Medina, et al., Conversion of glycerol over 10%Ni/γ-Al2O3 catalyst, Appl. Catal. B Environ. 147 (2014) 464–480. doi:10.1016/j.apcatb.2013.09.026.

[122] T.S. Nguyen, S. He, G. Raman, K. Seshan, Catalytic hydro-pyrolysis of lignocellulosic biomass over dual Na2CO3/Al2O3 and Pt/Al2O3 catalysts using n-butane at ambient pressure, Chem. Eng. J. 299 (2016) 415–419. doi:10.1016/j.cej.2016.04.104.

[123] M.B.I. Chowdhury, M.M. Hossain, P.A. Charpentier, Effect of supercritical water gasification treatment on Ni/La2O3-Al2O3-based catalysts, Appl. Catal. A Gen. 405 (2011) 84–92. doi:10.1016/j.apcata.2011.07.031.

[124] S. Adamu, H. Binous, S.A. Razzak, M.M. Hossain, Enhancement of glucose gasification by Ni/La2O3-Al2O3 towards the thermodynamic extremum at supercritical water conditions, Renew. Energy. 111 (2017) 399–409. doi:10.1016/j.renene.2017.04.020.

[125] K.E. Sedor, M.M. Hossain, H.I. de Lasa, Reactivity and stability of Ni/Al2O3 oxygen carrier for chemical-looping combustion (CLC), Chem. Eng. Sci. 63 (2008) 2994–3007. doi:10.1016/j.ces.2008.02.021.

[126] G. Haarlemmer, Simulation study of improved biomass drying efficiency for biomass gasification plants by integration of the water gas shift section in the drying process, Biomass and Bioenergy. 81 (2015) 129–136. doi:10.1016/j.biombioe.2015.06.002.

[127] S.N. Reddy, S. Nanda, A.K. Dalai, J. a. Kozinski, Supercritical water gasification of biomass for hydrogen production, Int. J. Hydrogen Energy. 39 (2014) 6912–6926. doi:10.1016/j.ijhydene.2014.02.125.

[128] S.R. Horton, R.J. Mohr, Y. Zhang, F.P. Petrocelli, M.T. Klein, Molecular-Level Kinetic Modeling of Biomass Gasification, Energy & Fuels. 30 (2016) 1647–1661. doi:10.1021/acs.energyfuels.5b01988.

[129] Y. Matsumura, S. Yanachi, T. Yoshida, Glucose decomposition kinetics in water at 25 MPa in the temperature range of 448-673 K, Ind. Eng. Chem. Res. 45 (2006) 1875–1879. doi:10.1021/ie050830r.

[130] C. Promdej, Y. Matsumura, Temperature effect on hydrothermal decomposition of glucose in sub- and supercritical water, Ind. Eng. Chem. Res. 50 (2011) 8492–8497. doi:10.1021/ie200298c.

[131] B. Hejazi, J.R. Grace, X. Bi, A. Mahecha-Botero, Kinetic Model of Steam Gasification of Biomass in a Bubbling Fluidized Bed Reactor, Energy & Fuels. 31 (2017) 1702–1711. doi:10.1021/acs.energyfuels.6b03161.

[132] E. Weiss-Hortala, A. Kruse, C. Ceccarelli, R. Barna, Influence of phenol on glucose degradation during supercritical water gasification, J. Supercrit. Fluids. 53 (2010) 42–47. doi:10.1016/j.supflu.2010.01.004.

[133] B.M. Kabyemela, T. Adschiri, R.M. Malaluan, K. Arai, Glucose and Fructose Decomposition in Subcritical and Supercritical Water: Detailed Reaction Pathway, Mechanisms, and Kinetics, Ind. Eng. Chem. Res. 38 (1999) 2888–2895. doi:10.1021/ie9806390.

[134] C. Franco, F. Pinto, I. Gulyurtlu, I. Cabrita, The study of reactions influencing the biomass steam gasification process q, 82 (2003) 835–842.

[135] E. Salaices, B. Serrano, H. De Lasa, Biomass Catalytic Steam Gasification Thermodynamics Analysis and Reaction Experiments in a CREC Riser Simulator, (2010) 6834–6844.

[136] P. Aznar, M.A. Caballero, A. Sancho, E. France, Plastic waste elimination by co-gasification with coal and biomass in fluidized bed with air in pilot plant, 87 (2006) 409–420. doi:10.1016/j.fuproc.2005.09.006.

[137] D.G. Roberts, D.J. Harris, Char gasification in mixtures of CO2 and H2O: Competition and inhibition, Fuel. 86 (2007) 2672–2678. doi:10.1016/j.fuel.2007.03.019.

[138] Y. Wang, C.M. Kinoshita, Kinetic model of biomass gasification, Sol. Energy. 51 (1993) 19–25.

[139] A.N. Fatsikostas, X.E. Verykios, Reaction network of steam reforming of ethanol over Ni-based catalysts, 225 (2004) 439–452. doi:10.1016/j.jcat.2004.04.034.

[140] J. Corella, A. Sanz, Modeling circulating fluidized bed biomass gasifiers. A pseudo-rigorous model for stationary state, Fuel Process. Technol. 86 (2005) 1021–1053. doi:10.1016/j.fuproc.2004.11.013.

[141] K. Jarosch, T. El Solh, H.I. de Lasa, Modelling the catalytic steam reforming of methane: discrimination between kinetic expressions using sequentially designed experiments, Chem. Eng. Sci. 57 (2002) 3439–3451. doi:10.1016/S0009-2509(02)00214-2.

[142] T. El Solh, K. Jarosch, H. De Lasa, Catalytic Dry Reforming of Methane in a CREC Riser Simulator Kinetic Modeling and Model Discrimination, (2003) 2507–2515. doi:10.1021/ie020749d.

[143] M. Maestri, D.G. Vlachos, A. Beretta, G. Groppi, E. Tronconi, Steam and dry reforming of methane on Rh : Microkinetic analysis and hierarchy of kinetic models, J. Catal. 259 (2008) 211–222. doi:10.1016/j.jcat.2008.08.008.

[144] D. Cheng, Z. Wang, Y. Xia, Y. Wang, W. Zhang, Catalytic amination of diethylene glycol with, RSC Adv. 6 (2016) 102373–102380. doi:10.1039/C6RA21894F.

[145] S.D. Senanayake, J.A. Rodriguez, D. Stacchiola, Electronic Metal–Support Interactions and the Production of Hydrogen Through the Water-Gas Shift Reaction and Ethanol Steam Reforming: Fundamental Studies with Well-Defined Model Catalysts, Top. Catal. 56 (2013) 1488–1498. doi:10.1007/s11244-013-0148-5.

[146] D. Li, M. Tamura, Y. Nakagawa, K. Tomishige, Metal catalysts for steam reforming of tar derived from the gasification of lignocellulosic biomass, Bioresour. Technol. 178 (2015) 53–64. doi:10.1016/j.biortech.2014.10.010.

[147] J. Ashok, S. Kawi, Steam reforming of biomass tar model compound at relatively low steam-to-carbon condition over CaO-doped nickel–iron alloy supported over iron–alumina catalysts, Appl. Catal. A Gen. 490 (2015) 24–35. doi:10.1016/j.apcata.2014.10.057.

[148] G. Eriksson, J.L. Holm, B.J. Welch, A. Prelesnik, I. Zupancic, L. Ehrenberg, Thermodynamic Studies of High Temperature Equilibria. III. SOLGAS, a Computer Program for Calculating the Composition and Heat Condition of an Equilibrium Mixture., Acta Chem. Scand. 25 (1971) 2651–2658. doi:10.3891/acta.chem.scand.25-2651.

[149] C.H. Twu, J.E. Coon, D. Bluck, A Comparison of the Peng-Robinson and Soave-Redlich-KwongEquations of State Using a New Zero-Pressure-Based Mixing Rule forthe Prediction of High Pressure and High Temperature Phase Equilibria, 5885 (1998) 1580–1585.

[150] Z. Duan, N. Møller, J.H. Weare, An equation of state for the CH4-CO2-H2O system: I. Pure systems from 0 to 1000 °C and 0 to 8000 bar, Geochim. Cosmochim. Acta. 56 (1992) 2605–2617. doi:10.1016/0016-7037(92)90347-L.

[151] Z. Duan, N. Møller, J.H. Weare, A general equation of state for supercritical fluid mixtures and molecular dynamics simulation of mixture PVTX properties, Geochim. Cosmochim. Acta. 60 (1996) 1209–1216. doi:10.1016/0016-7037(96)00004-X.

APPENDIX

```
R = 8.3144 * 10^-5;
To = 898.15`;
T = .;
W = 0.2;(* Cat wt in g*)
V = 50.7 * 10^-6;(*% m3 reactor vol*)

abscissae = {5, 10, 15, 20, 25};
init = {{0.27438`, 0.428446389`, 0.654266958`, 0.743544858`},
   {0.189958`, 0.338318847`, 0.652340013`, 0.902796668`},
   {0.302656`, 0.256950673`, 0.121076233`, 0.024215247`},
   {0.29086`, 0.267443399`, 0.208968063`, 0.170582413`},
   {1.73571`, 1.732075472`, 1.724528302`, 1.720754717`}};
KWGS1 = 3.640; KSRM1 = 0.0799; KRDRM1 = 45.500;
KWGS2 = 2.690; KSRM2 = 0.518; KRDRM2 = 5.190;
KWGS3 = 2.060; KSRM3 = 2.760; KRDRM3 = 0.747;
KWGS4 = 1.630;
KSRM4 = 12.400;
KRDRM4 = 0.131;

kwgs[T_] := kwgs0 * Exp[-Ewgs / R * (1 / T - 1 / To)];
ksrm[T_] := ksrm0 * Exp[-Esrm / R * (1 / T - 1 / To)];
krdrm[T_] := krdrm0 * Exp[-Erdrm / R * (1 / T - 1 / To)];
KAh2[T_] := KAh20 * Exp[-dHh2 / R * (1 / T - 1 / To)];
KAco[T_] := KAco0 * Exp[-dHco / R * (1 / T - 1 / To)];
KAco2[T_] := KAco20 * Exp[-dHco2 / R * (1 / T - 1 / To)];
KAch4[T_] := KAch40 * Exp[-dHch4 / R * (1 / T - 1 / To)];
KAh2o[T_] := KAh2o0 * Exp[-dHh2o / R * (1 / T - 1 / To)];
T1 = 550 + 273.15;
T2 = 600 + 273.15;
T3 = 650 + 273.15;
T4 = 700 + 273.15;

wgs1 = W / V * R * T1 * kwgs[T1] * 10^-5 * p1co[t] *
   p1h2o[t] /
    (1 + (KAco2[T1] * p1co2[t] + KAco[T1] * p1co[t] + KAh2o[T1] * p1h2o[t] + KAh2[T1] * p1h2[t] +
         KAch4[T1] * p1ch4[t]) * 10^-5) * (1 - p1h2[t] * p1co2[t] / (KWGS1 * p1co[t] * p1h2o[t]));
srm1 = W / V * R * T1 * ksrm[T1] * 10^-5 * p1ch4[t] *
   p1h2o[t] /
    ((1 + (KAco2[T1] * p1co2[t] + KAco[T1] * p1co[t] + KAh2o[T1] * p1h2o[t] + KAh2[T1] * p1h2[t] +
           KAch4[T1] * p1ch4[t]) * 10^-5)^4) * (1 - p1co[t] * p1h2[t]^3 / (KSRM1 * p1ch4[t] * p1h2o[t]));
rdrm1 = W / V * R * T1 * krdrm[T1] * 10^-5 * p1co[t]^2 *
   p1h2[t]^2 /
    ((1 + (KAco2[T1] * p1co2[t] + KAco[T1] * p1co[t] + KAh2o[T1] * p1h2o[t] + KAh2[T1] * p1h2[t] +
```

```
            KAch4[T1] * p1ch4[t]) * 10^-5)^4) * (1 - p1co2[t] * p1ch4[t] / (KRDRM1 * p1co[t]^2 * p1h2[t]^2));
wgs2 = W / V * R * T2 * kwgs[T2] * 10^-5 * p2co[t] *
    p2h2o[t] /
     (1 + (KAco2[T2] * p2co2[t] + KAco[T2] * p2co[t] + KAh2o[T2] * p2h2o[t] + KAh2[T2] * p2h2[t] +
           KAch4[T2] * p2ch4[t]) * 10^-5) * (1 - p2h2[t] * p2co2[t] / (KWGS2 * p2co[t] * p2h2o[t]));
srm2 = W / V * R * T2 * ksrm[T2] * 10^-5 * p2ch4[t] *
    p2h2o[t] /
     ((1 + (KAco2[T2] * p2co2[t] + KAco[T2] * p2co[t] + KAh2o[T2] * p2h2o[t] + KAh2[T2] * p2h2[t] +
            KAch4[T2] * p2ch4[t]) * 10^-5)^4) * (1 - p2co[t] * p2h2[t]^3 / (KSRM2 * p2ch4[t] * p2h2o[t]));
rdrm2 = W / V * R * T2 * krdrm[T2] * 10^-5 * p2co[t]^2 *
    p2h2[t]^2 /
     ((1 + (KAco2[T2] * p2co2[t] + KAco[T2] * p2co[t] + KAh2o[T2] * p2h2o[t] + KAh2[T2] * p2h2[t] +
            KAch4[T2] * p2ch4[t]) * 10^-5)^4) * (1 - p2co2[t] * p2ch4[t] / (KRDRM2 * p2co[t]^2 * p2h2[t]^2));
wgs3 = W / V * R * T3 * kwgs[T3] * 10^-5 * p3co[t] *
    p3h2o[t] /
     (1 + (KAco2[T3] * p3co2[t] + KAco[T3] * p3co[t] + KAh2o[T3] * p3h2o[t] + KAh2[T3] * p3h2[t] +
           KAch4[T3] * p3ch4[t]) * 10^-5) * (1 - p3h2[t] * p3co2[t] / (KWGS3 * p3co[t] * p3h2o[t]));


srm3 = W / V * R * T3 * ksrm[T3] * 10^-5 * p3ch4[t] *
    p3h2o[t] /
     ((1 + (KAco2[T3] * p3co2[t] + KAco[T3] * p3co[t] + KAh2o[T3] * p3h2o[t] + KAh2[T3] * p3h2[t] +
            KAch4[T3] * p3ch4[t]) * 10^-5)^4) * (1 - p3co[t] * p3h2[t]^3 / (KSRM3 * p3ch4[t] * p3h2o[t]));
rdrm3 = W / V * R * T3 * krdrm[T3] * 10^-5 * p3co[t]^2 *
    p3h2[t]^2 /
     ((1 + (KAco2[T3] * p3co2[t] + KAco[T3] * p3co[t] + KAh2o[T3] * p3h2o[t] + KAh2[T3] * p3h2[t] +
            KAch4[T3] * p3ch4[t]) * 10^-5)^4) * (1 - p3co2[t] * p3ch4[t] / (KRDRM3 * p3co[t]^2 * p3h2[t]^2));
wgs4 = W / V * R * T4 * kwgs[T4] * 10^-5 * p4co[t] *
    p4h2o[t] /
     (1 + (KAco2[T4] * p4co2[t] + KAco[T4] * p4co[t] + KAh2o[T4] * p4h2o[t] + KAh2[T4] * p4h2[t] +
           KAch4[T4] * p4ch4[t]) * 10^-5) * (1 - p4h2[t] * p4co2[t] / (KWGS4 * p4co[t] * p4h2o[t]));
srm4 = W / V * R * T4 * ksrm[T4] * 10^-5 * p4ch4[t] *
    p4h2o[t] /
     ((1 + (KAco2[T4] * p4co2[t] + KAco[T4] * p4co[t] + KAh2o[T4] * p4h2o[t] + KAh2[T4] * p4h2[t] +
            KAch4[T4] * p4ch4[t]) * 10^-5)^4) * (1 - p4co[t] * p4h2[t]^3 / (KSRM4 * p4ch4[t] * p4h2o[t]));
```

```
rdrm4 = W / V * R * T4 * krdrm[T4] * 10^-5 * p4co[t]^2 *
   p4h2[t]^2 /
    ((1 + (KAco2[T4] * p4co2[t] + KAco[T4] * p4co[t] + KAh2o[T4] * p4h2o[t] + KAh2[T4] * p4h2[t] +
           KAch4[T4] * p4ch4[t]) * 10^-5)^4) * (1 - p4co2[t] * p4ch4[t] / (KRDRM4 * p4co[t]^2 * p4h2[t]^2));

eqn1 = p1h2'[t] == wgs1 + 3 * srm1 - 2 * rdrm1;
eqn2 = p1co'[t] == -wgs1 + srm1 - 2 * rdrm1;
eqn3 = p1co2'[t] == wgs1 + rdrm1;
eqn4 = p1ch4'[t] == -srm1 + rdrm1;
eqn5 = p1h2o'[t] == -wgs1 - srm1;
eqn6 = p2h2'[t] == wgs2 + 3 * srm2 - 2 * rdrm2;
eqn7 = p2co'[t] == -wgs2 + srm2 - 2 * rdrm2;
eqn8 = p2co2'[t] == wgs2 + rdrm2;
eqn9 = p2ch4'[t] == -srm2 + rdrm2;
eqn10 = p2h2o'[t] == -wgs2 - srm2;
eqn11 = p3h2'[t] == wgs3 + 3 * srm3 - 2 * rdrm3;
eqn12 = p3co'[t] == -wgs3 + srm3 - 2 * rdrm3;
eqn13 = p3co2'[t] == wgs3 + rdrm3;
eqn14 = p3ch4'[t] == -srm3 + rdrm3;
eqn15 = p3h2o'[t] == -wgs3 - srm3;
eqn16 = p4h2'[t] == wgs4 + 3 * srm4 - 2 * rdrm4;

eqn17 = p4co'[t] == -wgs4 + srm4 - 2 * rdrm4;
eqn18 = p4co2'[t] == wgs4 + rdrm4;
eqn19 = p4ch4'[t] == -srm4 + rdrm4;
eqn20 = p4h2o'[t] == -wgs4 - srm4;


hamda = ParametricNDSolveValue[{eqn1, p1h2[5] == init[[1, 1]], eqn2, p1co[5] == init[[2, 1]],
   eqn3, p1co2[5] == init[[3, 1]], eqn4, p1ch4[5] == init[[4, 1]], eqn5, p1h2o[5] == init[[5, 1]],
   eqn6, p2h2[5] == init[[1, 2]], eqn7, p2co[5] == init[[2, 2]], eqn8, p2co2[5] == init[[3, 2]],
   eqn9, p2ch4[5] == init[[4, 2]], eqn10, p2h2o[5] == init[[5, 2]], eqn11, p3h2[5] == init[[1, 3]],
   eqn12, p3co[5] == init[[2, 3]], eqn13, p3co2[5] == init[[3, 3]], eqn14, p3ch4[5] == init[[4, 3]],
   eqn15, p3h2o[5] == init[[5, 3]], eqn16, p4h2[5] == init[[1, 4]], eqn17, p4co[5] == init[[2, 4]],
   eqn18, p4co2[5] == init[[3, 4]], eqn19, p4ch4[5] == init[[4, 4]], eqn20, p4h2o[5] == init[[5, 4]]

  }, {p1h2, p2h2, p3h2, p4h2, p1co, p2co, p3co, p4co, p1co2, p2co2, p3co2, p4co2, p1ch4,
   p2ch4, p3ch4, p4ch4, p1h2o, p2h2o, p3h2o, p4h2o}, {t, 5, 25},
  {kwgs0, ksrm0, krdrm0, Ewgs, Esrm, Erdrm, KAh20, KAco0, KAco20, KAch40, KAh2o0, dHh2,
   dHco, dHco2, dHch4, dHh2o}]
```

```
ParametricFunction[
  Expression: {p1h2, p2h2, p3h2, p4h2, p1co, p2co, p3co, p4co, p1co2, p2co2, p3co2, p4co2, p1ch4, p2ch4, p3ch4, p4ch4, p1h2o, p2h2o, p3h2o, p4h2o}
  Parameters: {kwgs0, ksrm0, krdrm0, Ewgs, Esrm, Erdrm, KAh20, KAco0, KAco20, KAch40, KAh2o0, dHh2, dHco, dHco2, dHch4, dHh2o}
]
```

```
AllTemp = {{1.`, 5.`, 0.27438`}, {1.`, 10.`, 0.393388`}, {1.`, 15.`, 0.441322`}, {1.`, 20.`, 0.489256`},
   {1.`, 25.`, 0.591736`}, {2.`, 5.`, 0.428446389`}, {2.`, 10.`, 0.559737418`}, {2.`, 15.`, 0.61487965`},
   {2.`, 20.`, 0.683150985`}, {2.`, 25.`, 0.767177243`}, {3.`, 5.`, 0.654266958`}, {3.`, 10.`, 0.751422319`},
   {3.`, 15.`, 0.853829322`}, {3.`, 20.`, 0.945733042`}, {3.`, 25.`, 1.040262582`}, {4.`, 5.`, 0.743544858`},
   {4.`, 10.`, 0.956236324`}, {4.`, 15.`, 1.12166302`}, {4.`, 20.`, 1.21619256`}, {4.`, 25.`, 1.310722101`},
   {5.`, 5.`, 0.189958`}, {5.`, 10.`, 0.145775`}, {5.`, 15.`, 0.129492`}, {5.`, 20.`, 0.123237`},
   {5.`, 25.`, 0.106285`}, {6.`, 5.`, 0.338318847`}, {6.`, 10.`, 0.315138573`}, {6.`, 15.`, 0.30317334`},
   {6.`, 20.`, 0.278123892`}, {6.`, 25.`, 0.25419973`}, {7.`, 5.`, 0.652340013`}, {7.`, 10.`, 0.505800585`},
   {7.`, 15.`, 0.450844359`}, {7.`, 20.`, 0.399632785`}, {7.`, 25.`, 0.357010583`}, {8.`, 5.`, 0.902796668`},
   {8.`, 10.`, 0.6814966`}, {8.`, 15.`, 0.609717812`}, {8.`, 20.`, 0.567852105`}, {8.`, 25.`, 0.515877731`},
   {9.`, 5.`, 0.302656`}, {9.`, 10.`, 0.326319`}, {9.`, 15.`, 0.351503`}, {9.`, 20.`, 0.37518`}, {9.`, 25.`, 0.415676`},
   {10.`, 5.`, 0.256950673`}, {10.`, 10.`, 0.289237668`}, {10.`, 15.`, 0.329596413`}, {10.`, 20.`, 0.365919283`},
   {10.`, 25.`, 0.431838565`}, {11.`, 5.`, 0.121076233`}, {11.`, 10.`, 0.267713004`}, {11.`, 15.`, 0.333632287`},
   {11.`, 20.`, 0.373991031`}, {11.`, 25.`, 0.44529148`}, {12.`, 5.`, 0.024215247`}, {12.`, 10.`, 0.240807175`},
   {12.`, 15.`, 0.341704036`}, {12.`, 20.`, 0.388789238`}, {12.`, 25.`, 0.460089686`}, {13.`, 5.`, 0.29086`},
   {13.`, 10.`, 0.26359`}, {13.`, 15.`, 0.24356`}, {13.`, 20.`, 0.230287`}, {13.`, 25.`, 0.218462`},
   {14.`, 5.`, 0.267443399`}, {14.`, 10.`, 0.247784644`}, {14.`, 15.`, 0.226332714`}, {14.`, 20.`, 0.219946407`},
   {14.`, 25.`, 0.21112217`}, {15.`, 5.`, 0.208968063`}, {15.`, 10.`, 0.21513781`}, {15.`, 15.`, 0.205523351`},
   {15.`, 20.`, 0.194834299`}, {15.`, 25.`, 0.179551023`}, {16.`, 5.`, 0.170582413`}, {16.`, 10.`, 0.17316581`},
   {16.`, 15.`, 0.149560866`}, {16.`, 20.`, 0.136000766`}, {16.`, 25.`, 0.12`}, {17.`, 5.`, 1.73571`},
   {17.`, 10.`, 1.70246`}, {17.`, 15.`, 1.68977`}, {17.`, 20.`, 1.66508`}, {17.`, 25.`, 1.64829`},
   {18.`, 5.`, 1.732075472`}, {18.`, 10.`, 1.674213836`}, {18.`, 15.`, 1.603773585`}, {18.`, 20.`, 1.564779874`},
   {18.`, 25.`, 1.500628931`}, {19.`, 5.`, 1.724528302`}, {19.`, 10.`, 1.608805031`}, {19.`, 15.`, 1.499371069`},
   {19.`, 20.`, 1.444025157`}, {19.`, 25.`, 1.372327044`}, {20.`, 5.`, 1.720754717`}, {20.`, 10.`, 1.524528302`},
   {20.`, 15.`, 1.374842767`}, {20.`, 20.`, 1.328301887`}, {20.`, 25.`, 1.240251572`}};
```

```
model[kwgs0_, ksrm0_, krdrm0_, Ewgs_, Esrm_, Erdrm_, KAh20_, KAco0_, KAco20_, KAch40_, KAh2o0_, dHh2_, dHco_,
   dHco2_, dHch4_, dHh2o_][i_, t_] :=
 Through[hamda[kwgs0, ksrm0, krdrm0, Ewgs, Esrm, Erdrm, KAh20, KAco0, KAco20, KAch40, KAh2o0, dHh2, dHco, dHco2, dHch4, dHh2o][
    t], List][[i]] /;
  And @@ NumericQ /@ {kwgs0, ksrm0, krdrm0, Ewgs, Esrm, Erdrm, KAh20, KAco0, KAco20, KAch40, KAh2o0, dHh2, dHco,
    dHco2, dHch4, dHh2o, i, t}
fit =
  Quiet[NonlinearModelFit[AllTemp,
    {model[kwgs0, ksrm0, krdrm0, Ewgs, Esrm, Erdrm, KAh20, KAco0, KAco20, KAch40, KAh2o0, dHh2, dHco, dHco2, dHch4, dHh2o][
      i, t], {kwgs0 > 0, ksrm0 > 0, krdrm0 > 0, Ewgs > 0, Esrm > 0, Erdrm > 0, KAh20 > 0, KAco0 > 0, KAco20 > 0,
      KAch40 > 0, KAh2o0 > 0, dHh2 > 0, dHco > 0, dHco2 > 0, dHch4 > 0, dHh2o > 0}},
    {{kwgs0, 1.3}, {ksrm0, 1.1}, {krdrm0, 2.30}, {Ewgs, 30}, {Esrm, 68}, {Erdrm, 89}, {KAh20, .1}, {KAco0, .1},
     {KAco20, .55}, {KAch40, .1}, {KAh2o0, .1}, {dHh2, 2}, {dHco, 2}, {dHco2, 20}, {dHch4, 3}, {dHh2o, 2}}, {i, t}]];

fit["AdjustedRSquared"]

0.99875
```

```
Quiet[fit["CorrelationMatrix"]] // MatrixForm
```

1.	0.523115	0.0195744	0.978185	-0.0308117	0.148126	0.00141501	-0.128966	-0.0710078	0.0969958	-0.139656	-0.0994072	-0.147383	0.171743	0.0719881	0.238931
0.523115	1.	-0.152641	0.511957	-0.168497	0.650539	0.412493	-0.44546	-0.363453	0.194059	-0.396946	-0.311051	-0.423873	0.92621	0.170163	0.500519
0.0195744	-0.152641	1.	0.0193526	0.812635	0.171304	0.513117	0.791836	0.889531	-0.947287	0.43213	-0.623856	-0.590677	-0.130748	0.63464	-0.284405
0.978185	0.511957	0.0193526	1.	-0.0299477	0.145264	0.00198291	-0.12657	-0.0693341	0.0945794	-0.136693	-0.0973659	-0.144628	0.168336	0.0706459	0.236291
-0.0308117	-0.168497	0.812635	-0.0299477	1.	0.496835	0.719572	0.617263	0.957592	-0.615107	-0.11734	-0.856327	-0.706522	-0.107736	0.902821	-0.410169
0.148126	0.650539	0.171304	0.145264	0.496835	1.	0.877434	-0.143425	0.238302	0.0270813	-0.707316	-0.845263	-0.798912	0.736892	0.761159	0.128437
0.00141501	0.412493	0.513117	0.00198291	0.719572	0.877434	1.	0.222882	0.529647	-0.366541	-0.394877	-0.90157	-0.885724	0.547797	0.805347	0.0815853
-0.128966	-0.44546	0.791836	-0.12657	0.617263	-0.143425	0.222882	1.	0.730413	-0.773249	0.488608	-0.269556	-0.243442	-0.41126	0.311964	-0.309363
-0.0710078	-0.363453	0.889531	-0.0693341	0.957592	0.238302	0.529647	0.730413	1.	-0.7422	0.140109	-0.701027	-0.557582	-0.324703	0.774137	-0.488873
0.0969958	0.194059	-0.947287	0.0945794	-0.615107	0.0270813	-0.366541	-0.773249	-0.7422	1.	-0.651491	0.402364	0.415972	0.143227	-0.402033	0.22928
-0.139656	-0.396946	0.43213	-0.136693	-0.11734	-0.707316	-0.394877	0.488608	0.140109	-0.651491	1.	0.386018	0.246928	-0.417798	-0.396568	0.00260927
-0.0994072	-0.311051	-0.623856	-0.0973659	-0.856327	-0.845263	-0.90157	-0.269556	-0.701027	0.402364	0.386018	1.	0.922633	-0.383742	-0.956618	0.0997613
-0.147383	-0.423873	-0.590677	-0.144628	-0.706522	-0.798912	-0.885724	-0.243442	-0.557582	0.415972	0.246928	0.922633	1.	-0.49176	-0.773779	-0.266595
0.171743	0.92621	-0.130748	0.168336	-0.107736	0.736892	0.547797	-0.41126	-0.324703	0.143227	-0.417798	-0.383742	-0.49176	1.	0.227445	0.473968
0.0719881	0.170163	0.63464	0.0706459	0.902821	0.761159	0.805347	0.311964	0.774137	-0.402033	-0.396568	-0.956618	-0.773779	0.227445	1.	-0.378615
0.238931	0.500519	-0.284405	0.236291	-0.410169	0.128437	0.0815853	-0.309363	-0.488873	0.22928	0.00260927	0.0997613	-0.266595	0.473968	-0.378615	1.

```
timeint = Range[5., 25, 1]
{5., 6., 7., 8., 9., 10., 11., 12., 13., 14., 15., 16., 17., 18., 19., 20., 21., 22., 23., 24., 25.}

par = fit["BestFitParameters"];

ordinates =
  ordinates = With[{Ewgs = Ewgs /. par, Esrm = Esrm /. par, Erdrm = Erdrm /. par, kwgs0 = kwgs0 /. par, ksrm0 = ksrm0 /. par, krdrm0 = krdrm0 /. par, KAh20 = KAh20 /. par, KAco0 = KAco0 /. par,
    KAco20 = KAco20 /. par, KAch40 = KAch40 /. par, KAh2o0 = KAh2o0 /. par, dHh2 = dHh2 /. par, dHco = dHco /. par, dHco2 = dHco2 /. par, dHch4 = dHch4 /. par, dHh2o = dHh2o /. par},
   Through[hamda[kwgs0, ksrm0, krdrm0, Ewgs, Esrm, Erdrm, KAh20, KAco0, KAco20, KAch40, KAh2o0, dHh2, dHco, dHco2, dHch4, dHh2o][timeint], List]];
k = ordinates // TableForm
```

0.27438	0.27438	0.27438	0.27438	0.27438	0.27438	0.27438	0.27438	0.27438	0.27438	0.27438	0.27438	0.27438	0.27438	0.27438	0.27438	0.27438
0.428446	0.428446	0.428446	0.428446	0.428446	0.428446	0.428446	0.428446	0.428446	0.428446	0.428446	0.428446	0.428446	0.428446	0.428446	0.428446	0.428446
0.654267	0.655267	0.656265	0.65726	0.658254	0.659245	0.660235	0.661222	0.662207	0.663189	0.66417	0.665149	0.666125	0.667099	0.668072	0.669042	0.67001
0.743545	0.743545	0.743545	0.743545	0.743545	0.743545	0.743545	0.743545	0.743545	0.743545	0.743545	0.743545	0.743545	0.743545	0.743545	0.743545	0.743545
0.189958	0.189958	0.189958	0.189958	0.189958	0.189958	0.189958	0.189958	0.189958	0.189958	0.189958	0.189958	0.189958	0.189958	0.189958	0.189958	0.189958
0.338319	0.338319	0.338319	0.338319	0.338319	0.338319	0.338319	0.338319	0.338319	0.338319	0.338319	0.338319	0.338319	0.338319	0.338319	0.338319	0.338319
0.65234	0.65134	0.650342	0.649347	0.648353	0.647362	0.646372	0.645385	0.6444	0.643418	0.642437	0.641458	0.640482	0.639508	0.638535	0.637565	0.636597
0.902797	0.902797	0.902797	0.902797	0.902797	0.902797	0.902797	0.902797	0.902797	0.902797	0.902797	0.902797	0.902797	0.902797	0.902797	0.902797	0.902797
0.302656	0.302656	0.302656	0.302656	0.302656	0.302656	0.302656	0.302656	0.302656	0.302656	0.302656	0.302656	0.302656	0.302656	0.302656	0.302656	0.302656
0.256951	0.256951	0.256951	0.256951	0.256951	0.256951	0.256951	0.256951	0.256951	0.256951	0.256951	0.256951	0.256951	0.256951	0.256951	0.256951	0.256951
0.121076	0.122076	0.123074	0.12407	0.125063	0.126055	0.127044	0.128031	0.129016	0.129999	0.130979	0.131958	0.132934	0.133909	0.134881	0.135851	0.136819
0.0242152	0.0242152	0.0242152	0.0242152	0.0242152	0.0242152	0.0242152	0.0242152	0.0242152	0.0242152	0.0242152	0.0242152	0.0242152	0.0242152	0.0242152	0.0242152	0.0242152
0.29086	0.29086	0.29086	0.29086	0.29086	0.29086	0.29086	0.29086	0.29086	0.29086	0.29086	0.29086	0.29086	0.29086	0.29086	0.29086	0.29086
0.267443	0.267443	0.267443	0.267443	0.267443	0.267443	0.267443	0.267443	0.267443	0.267443	0.267443	0.267443	0.267443	0.267443	0.267443	0.267443	0.267443
0.208968	0.208968	0.208968	0.208968	0.208968	0.208968	0.208968	0.208968	0.208968	0.208968	0.208968	0.208968	0.208968	0.208968	0.208968	0.208968	0.208968
0.170582	0.170582	0.170582	0.170582	0.170582	0.170582	0.170582	0.170582	0.170582	0.170582	0.170582	0.170582	0.170582	0.170582	0.170582	0.170582	0.170582
1.73571	1.73571	1.73571	1.73571	1.73571	1.73571	1.73571	1.73571	1.73571	1.73571	1.73571	1.73571	1.73571	1.73571	1.73571	1.73571	1.73571
1.73208	1.73208	1.73208	1.73208	1.73208	1.73208	1.73208	1.73208	1.73208	1.73208	1.73208	1.73208	1.73208	1.73208	1.73208	1.73208	1.73208
1.72453	1.72353	1.72253	1.72153	1.72054	1.71955	1.71856	1.71757	1.71659	1.71561	1.71463	1.71365	1.71267	1.7117	1.71072	1.70975	1.70879
1.72075	1.72075	1.72075	1.72075	1.72075	1.72075	1.72075	1.72075	1.72075	1.72075	1.72075	1.72075	1.72075	1.72075	1.72075	1.72075	1.72075

VITAE

BIO-DATA

Name	Sagir Adamu
Nationality	Nigerian
Date of Birth	1/2/1984
Permanent Address	46 Nagarke Road Hayin Dogo Samaru, P.O. Box 810107, Zaria Nigeria
Email	sagir@kfupm.edu.sa; cesa2020@yahoo.com
Mobile number	+966535701327

RESEARCH INTERESTS

- Synthesis of metal oxide catalysts for clean energy application
- Thermodynamic and kinetic studies for heterogeneous catalytic reactions

EDUCATION

- PhD. Chemical Engineering, KFUPM, Saudi Arabia, December 2017
  CGPA: 3.9/4.0 (**Distinction**)
- M.Sc. Chemical Engineering and Center for Refining and Petrochemicals KFUPM, Saudi Arabia, May 2013
  CGPA: 3.9/4.0 (**Distinction**)
- B. Eng. Chemical Engineering, Ahmadu Bello University, Zaria, Nigeria, April 2009
  CGPA: 4.64/5.00 (**First Class**)

RESEARCH EXPERIENCE

- **Ph.D. research** at the Department of Chemical Engineering, KFUPM (September 2013 – December 2017)
  - Ni/CeO_2-Al_2O_3 catalyst development for biomass gasification
  - Designing and conducting experiments to test catalyst performance in a riser simulator and in an autoclave engineer's batch reactor

- Kinetic modeling for biomass gasification in riser simulator

❖ **M.Sc. research** at the Center of Research Excellence in Petroleum Refining and Petrochemicals, KFUPM Research Institute. (September 2011 – May 2013).
  - Synthesis of supported metallocene catalysts and application to copolymerization of ethylene with 4-methyl-1-pentene

❖ **B.Eng.** at Ahmadu Bello University, Zaria Nigeria (July 2003 – April 2009).
  - Modeling and simulation of tall form spay dryer

TEACHING EXPERIENCE

❖ At KFUPM as Lecturer-B, from September 2013 to Date

Course taught	Tasks
Chemical Engineering Lab I (CHE 309)	Teaching the application, and theoretical aspects of equipment on heat transfer, mass transfer and fluid mechanics.
Teaching assistance in Transport Phenomena (CHE 501)	Grading and proctoring
Teaching assistance in Numerical Methods in CHE (CHE 560)	Proctoring, grading and tutorial on solving numerical problems in MATHEMATICA
Teaching assistance in the course: Polymer Technology (CHE 463)	Grading and proctoring
Teaching assistance for the course: Transport Phenomena I (CHE 204)	Grading, tutorials and proctoring

❖ At Ahmadu Bello University Zaria, as an Assistant Lecturer (October 2010 – August 2011)

Course taught	Tasks
Chemical Process Technology (CHEN 505)	Teaching the course material with a Senior colleague
Process Dynamics and Control (CHEN 502)	Teaching the course material with a Senior colleague
Postgraduate Diploma course in "Introduction to Chemical Engineering"	Teaching the course material with a Senior colleague

LIST OF PUBLICATIONS

❖ **Published/Accepted:**

- **Sagir Adamu**, Housam Binous, Shaikh A. Razzak, Mohammad M. Hossain. Enhancement of glucose gasification by Ni/La_2O_3-Al_2O_3 towards the thermodynamic extremum at supercritical water conditions, *Renewal Energy Journal,* DOI: https://doi.org/10.1016/j.renene.2017.04.020. **IF: 4.357**

- **Sagir Adamu**, Muhammad Y. Khan, Shaikh A. Razzak, Mohammad M. Hossain. Ceria-stabilized meso-Al_2O_3: synthesis, characterization, and desorption kinetics, *Journal of Porous Materials* 2017, DOI: https://doi.org/10.1007/s10934-017-0376-3. **IF: 1.624**

- **Adamu S,** Hossain, M.M. Detailed kinetic modeling of Ni(20)/Ce-meso-Al_2O_3 catalyzed gasification of cellulosic biomass in a CREC riser simulator, *Industrial and Engineering Chemistry Research*, (Accepted Feb. 2018). **IF: 2.843**

- Muflih A.A, **Adamu S**, Muraza O. Hossain M.M. Fluidizable NiO-Fe2O3/SiO2-γAl_2O_3 for tar (toluene) conversion in biomass gasification, *Process Safety and Environmental Protection*, DOI: https://doi.org/10.1016/j.psep.2017.12.021. **IF: 2.905**

❖ **Under review**

- **Adamu S**, Hossain, M.M. Ni/Ce-meso-Al_2O_3 for biomass gasification in a riser simulator: Effect of nickel loading, and mode of catalyst regeneration on Syngas Composition, *Journal of Industrial and Engineering Chemistry*, submitted November 2017)

- **Adamu S,** Hossain, M.M. Effect of ceria modification of Ni/Al_2O_3 on gasification of glucose/toluene mixed feed, *International Symposia on Chemical Reaction Engineering*, ISCRE 25 (Extended version of this manuscript will be submitted to AIChE Journal).

❖ **Conferences paper:**

- **Adamu S**, Mohammad Mozahar Hossain, Novel Ni/La-Al_2O_3 for Gasification of Biomass Surrogate in Supercritical Water. (*Accepted for MEPEC 2017 Technical Program: 09 - 11 October 2017 Bahrain International Exhibition and Convention Centre*).

PROJECT PARTICIPATION

(1) National Science and Technology Innovation Plan (MAARIFAH) project number 14-PET-283-04. PI: Muhammad Atiqullah

(2) King Abdul Aziz City for Science and Technology (KACST) under KACST-TIC for CCS project no 03. PI: Dr. Mohammad Mozahar Hossain